State-of-Charge Estimation of Lithium-ion Battery for a Satellite Power Management System

HTET AUNG

School of Electrical & Electronic Engineering

A thesis submitted to the Nanyang Technological University

in fulfilment of the requirement for the degree of

Doctor of Philosophy

2015

ACKNOWLEDGEMENT

It has been a long road with many ups and down, but here I am at the end. I am very grateful for everyone who has been there to support me throughout the journey and could not have succeeded without these invaluable support. Of all these people, there are selective few whom I would like to mention.

First and foremost, I would like to express my deepest and sincere gratitude to my supervisor A/P Low Kay Soon for his valuable advice, encouragement and support during my PhD studies. Not only has he imparted academic knowledge and skills required to successfully complete my studies, but also he has influenced me as a better person in life. Being my supervisor for my final year project as well, it was indeed a great pleasure to continue my graduate studies under his guidance.

The author would like to thank all the technical staff members from Satellite Research Centre (SaRC), Mrs. Tan Geok Lan Janet, Mrs. Yap Poh Geok Pamela and Mrs. Tham Suet Mei for their kind support in the technical and administrative matters throughout the studies. I also want to thank Mr. Soon Jing Jun, my senior graduate fellow, and Mr. Lew Jia Min for their generous help, technical and personal suggestions in my studies. The author is also very thankful to everyone from SaRC. It is a pleasure to work among many friends. The enjoyable time we spent together has indeed brought joy to me in many occasions.

I would like to acknowledge Nanyang Technological University for the support of my graduate studies through the Nanyang Graduate Scholarship.

No acknowledgment would be complete without giving thanks to my parents. I would not have gotten to where I am today without the support, care and unconditional love from them. They always believe in me and support me in every decision I made in

my life. I will forever be indebted to them. I hope I have made them proud and I dedicate this thesis to my beloved parents. Last but not least, to my loving and supportive fiancée, thank you for your love and unwavering support throughout these years.

TABLE OF CONTENTS

ACKNOWLEDGEMENT ..... **I**

TABLE OF CONTENTS ..... **III**

LIST OF ACRONYM ..... **VII**

ABSTRACT ..... **VIII**

LIST OF FIGURES ..... **X**

LIST OF TABLES ..... **XIV**

CHAPTER 1 ..... **1**

1. INTRODUCTION **1**

1.1 Background 1

1.2 Motivations 2

1.3 Objectives 3

1.4 Main contribution 4

1.5 Outline of Thesis 5

CHAPTER 2 ..... **7**

2. LITERATURE REVIEW **7**

2.1 Lithium-ion Battery Chemistry 7

2.2 Modelling of Lithium-ion Battery 11

2.2.1 Electrochemical models 13

2.2.2 Equivalent circuit models 18

2.3 State-of-Charge (SOC) Estimation Methods 24

2.4 Summary 29

CHAPTER 3 ..... **31**

3. OPPORTUNISTIC STATE-OF-CHARGE ESTIMATION **31**

3.1 Introduction 31

3.2 Modelling of Lithium-ion Batteries 32
3.2.1 Battery parameters identification 33
3.2.2 Charge and discharge rate factor 37
3.3 Opportunistic State-of-Charge Estimation 39
3.4 Experimental Setup and Evaluation 42
3.5 Summary 47
CHAPTER 4 48
4. SQUARE ROOT SPHERICAL UNSCENTED KALMAN FILTER BASED STATE-OF-CHARGE ESTIMATION 48
4.1 Introduction 48
4.2 Square Root Spherical Unscented Kalman Filter SOC Estimation 49
4.2.1 Battery state space equations 49
4.2.2 Open-circuit voltage (V_{OC}) versus state-of-charge (SOC) 50
4.2.3 Battery parameters extraction 52
4.2.4 Square root spherical unscented Kalman filter 57
1) Unit hyper sphere spherical unscented transform 57
2) Square root unscented Kalman filter (Sqrt-UKFST) 59
4.3 Simulation and Experimental Evaluation of Sqrt-UKFST 63
4.3.1 Simulation studies of Sqrt-UKFST 63
4.3.2 Experimental studies of Sqrt-UKFST 67
1) SOC estimation with unknown initial state 67
2) SOC estimation with known initial state 68
3) Computational requirements 71
4) Robustness study in terms of battery's parameters variation 72
4.4 Summary 74

CHAPTER 5 76

5. DUAL SPHERICAL UNSCENTED KALMAN FILTER BASED STATE-OF-CHARGE ESTIMATION 76

5.1 Introduction 76

5.2 Temperature Dependent Lithium-ion Battery Model 77

5.2.1 Open-circuit voltage V_{OC} versus SOC at 0°C, 25°C and 50°C 79

5.2.2 Battery state space model 81

5.3 Dual Spherical Square Root Unscented Kalman Filter 82

5.4 Simulation and Experimental Evaluation of DUKFST 90

5.4.1 Simulation study of DUKFST 90

5.4.2 Experimental studies of DUKFST 93

1) Robustness and convergence study in terms of initial SOC error ... 94

2) SOC Estimation at 0°C, 25°C and 50°C 97

3) Computational requirement 101

5.5 Summary 102

CHAPTER 6 103

6. PARTICLE SWARM OPTIMIZATION STATE-OF-CHARGE ESTIMATION 103

6.1 Introduction 103

6.2 Particle Swarm Optimization based SOC Estimation 104

6.2.1 Formulation of objective function 105

6.2.2 Inverse barrier constraint 106

6.2.3 The PSO algorithm 108

6.3 Experimental Evaluation 109

6.4 Summary 115

CHAPTER 7 116

7. CONCLUSION AND FUTURE WORKS 116

7.1 Conclusion 116

7.2 Future Works 118

LIST OF PUBLICATIONS 120

BIBLIOGRAPHY 121

LIST OF ACRONYM

BMS	Battery management system
CC-CV	Constant current-constant voltage charging method
C_D	Diffusion capacitance
C_K	Kinetic reaction capacitance
DOD	Depth of discharge
DUKST	Dual square root unscented Kalman filter with spherical transform
EIS	Electrochemical impedance spectroscopy
EKF	Extended Kalman filter
OCV (V_{OC})	Open-circuit voltage
PSO	Particle swarm optimization
R_o	Ohmic resistance
R_C	Diffusion resistance
R_K	Kinetic reaction resistance
R_{int}	Total internal resistance
Sqrt-UKFST	Square root unscented Kalman filter with spherical transform
SOC	State-of-charge
SOH	State-of-health
UKF	Unscented Kalman filter
τ_D	Diffusion time constant
τ_K	Kinetic reactions time constant

ABSTRACT

The lithium-ion battery has become an important energy source for many applications due to its numerous advantages such as high energy density, lack of memory effect, low self-discharging rate, and long cycle life. This also makes it a very promising candidate for pico- and nanosatellites that have space and weight constraint. For high performance and reliability, it is necessary to have accurate knowledge of the present condition of the battery and the remaining battery life. Among the many ways to monitor the battery conditions, estimation of battery's state-of-charge (SOC) is one of the critical tasks in battery management of the satellite power subsystem. Since the satellite operates at different temperatures throughout the orbit, its operating temperature, which is the most significant factor that affects the SOC estimation, must be taken into consideration. In this thesis, four different SOC estimation methods for a satellite have been progressively proposed and developed.

Under different orbital periods, the satellite operates with different subsystems. Taking advantage of different operational scenarios of satellites in different orbits, a SOC estimation method using ampere-hour counting with impulse response reset is proposed and developed. The impulse response is obtained from turning on/off of satellite subsystems and payloads that occur by the satellite operations rather than using an artificial injected pulse. The charging and discharging dependency on current have been considered and taken into account as the charge and discharge rate factors in the method. Moreover, integral resets can be conducted at all SOC levels instead of the traditional fully charged/discharged state. It eliminates the risk of increasing the number of fully charged and discharged cycles thus extending the battery life span. For this

approach, it requires a lookup table to store the various impulse responses which vary at different operating temperatures.

To further improve the performance, a SOC estimation method using the square root unscented Kalman filter (Sqrt-UKFST) with unit-sphere spherical transform has been developed. The Sqrt-UKFST takes advantage of Jacobian-free linearization, which is one of the major drawbacks of extended Kalman filter (EKF) based methods used in SOC estimation. It has a higher error order (second order) than EKF (first order). When it is compared with the unscented transform, fewer sigma points are needed for estimation of sample mean and covariance by using the spherical unscented transform. This results in 32% lower computational requirements. The satellite's operating temperature varies across the orbit and it is one of the critical factors that affect the battery parameters. To include the temperature factor, the SOC estimation with a dual square root unscented Kalman filter (DUKFST) has been developed. In this approach, a dual unscented Kalman filter is used to update battery parameters at different temperature through adaptive covariance matching. The temperature effect on open-circuit voltage (OCV) has been modelled in the DUFKST. All Kalman filter (KF) based methods require the knowledge of measurement and process noise. If not determined properly, it can lead to poor performance in terms of filter divergence and instability. A SOC estimation based on particle swarm optimization (PSO) with inverse barrier constraint is proposed to overcome these drawbacks. This method neither needs to linearize the model nor requires the information on measurement and process noise.

LIST OF FIGURES

Fig. 2.1 Comparison with different battery chemistries in terms of gravimetric and volumetric energy densities [38] 8

Fig. 2.2 Schematic of electrochemical process of lithium-ion cell [39] 9

Fig. 2.3 Anatomy of 1D lithium-ion cell [46] 16

Fig. 2.4 Resistive R_{int} model 18

Fig. 2.5 Half-cell EIS circuit 19

Fig. 2.6 Battery charge depletion and recovery effect during a discharge pulse [46] 20

Fig. 2.7 Dynamic Thevenin RC models 20

Fig. 2.8 Thevenin model 21

Fig. 2.9 Improved Thevenin or double polarization model 22

Fig. 2.10 Runtime based electrical model 23

Fig. 3.1 Equivalent circuit model of lithium-ion battery 32

Fig. 3.2 Battery discharging profile for parameters identification 34

Fig. 3.3 Discharge current pulses applied at 60% SOC 35

Fig. 3.4 Discharge current pulse voltage responses at 60% SOC 35

Fig. 3.5 Voltage response at 60% SOC by 0.58A (0.2C) 36

Fig. 3.6 Charge and discharge resistance versus SOC 37

Fig. 3.7 Battery voltage curves under 0.55A, 1.375A, 2.0625A and 2.75A constant current discharge 38

Fig. 3.8 Discharge rate factors with reference to 1.375A (I_{Ref}) 38

Fig. 3.9 Battery voltage curves under 0.29A, 0.58A, 1.16A and 1.375A constant current charge 39

Fig. 3.10 Charge rate factors with reference to 1.375A (I_{Ref}) 39

Fig. 3.11 Battery impulse response (IR) at 95%, 75% and 50% SOC.....41
Fig. 3.12 Estimated voltage response from 1.45A discharge current.....42
Fig. 3.13 Estimated voltage response from 0.58A charge current.....42
Fig. 3.14 Experimental setup block diagram.....43
Fig. 3.15 LEO orbital scenario solar and load power profile.....44
Fig. 3.16 Battery voltage measurements at various SOCs.....45
Fig. 3.17 Comparison of measured voltage at 78% SOC and calculated voltage using impulse response of 78% and 80% SOC.....45
Fig. 3.18 Comparison between reference and estimated SOC.....46
Fig. 3.19 Estimation error between reference and estimated SOC.....46
Fig. 4.1 V_{OC} versus SOC Graph.....51
Fig. 4.2 Battery parameters extraction discharge current profile.....53
Fig. 4.3 Injected discharge and charge pulses at the end of each rest period.....54
Fig. 4.4 Discharge and charge pulse voltage responses at 90% SOC.....54
Fig. 4.5 R_o at different SOC.....55
Fig. 4.6 Hybrid pulse power characterization (HPPC) load profile.....56
Fig. 4.7 Comparison of experimental and estimated voltages of discharge pulses.....56
Fig. 4.8 Voltage estimation error of discharge pulses.....57
Fig. 4.9 Flowchart of Sqrt-UKFST.....63
Fig. 4.10 Sqrt-UKFST simulation testbed in Simulink.....64
Fig. 4.11 Charge and discharge profile of simulation.....65
Fig. 4.12 SOC estimation comparison in simulation.....65
Fig. 4.13 Absolute SOC estimation error in simulation.....66
Fig. 4.14 SOC estimation with unknown initial state.....68
Fig. 4.15 SOC estimation error under unknown initial SOC.....68

Fig. 4.16 Battery current profile under orbital test experiment 69
Fig. 4.17 Comparison of SOC estimation 69
Fig. 4.18 Comparison of SOC estimation error 70
Fig. 4.19 RMSE comparison with different parameters set between EKF and Sqrt-UKFST 74
Fig. 4.20 Absolute maximum SOC error comparison with different parameters set between EKF and Sqrt-UKFST 74
Fig. 5.1 Temperature dependent double polarization model 77
Fig. 5.2 1.45A (0.5C) discharge pulse response at different temperatures (0°C, 25°C and 50°C) 78
Fig. 5.3 1.45A constant current discharge curve at different temperatures (0°C, 25°C and 50°C) 78
Fig. 5.4 V_{OC} at 50% SOC at 0°C 79
Fig. 5.5 V_{OC} at 50% SOC at 50°C 80
Fig. 5.6 V_{OC} versus SOC at 0°C, 25°C and 50°C 81
Fig. 5.7 Flowchart of DUKFST 89
Fig. 5.8 Thermal dependent lithium-ion battery model in Simulink [184] 90
Fig. 5.9 Simulation load profile of DUKFST 91
Fig. 5.10 Battery operation temperature at 25°C 91
Fig. 5.11 SOC estimation comparison at 25°C 92
Fig. 5.12 Absolute SOC error comparison at 25°C 92
Fig. 5.13 Absolute SOC error comparison at 0°C 93
Fig. 5.14 VELOX-I nanosatellite payload current profile 94
Fig. 5.15 Initial SOC error convergence study at 25°C with different initial errors 95
Fig. 5.16 SOC estimation error under unknown initial SOC at 25°C 96

Fig. 5.17 SOC comparison at 50°C....98
Fig. 5.18 SOC error comparison at 50°C....98
Fig. 5.19 SOC error comparison at 0°C....99
Fig. 5.20 SOC error comparison at 25°C....99
Fig. 5.21 R_o at 0°C, 25°C and 50°C....100
Fig. 5.22 τ_D at 0°C, 25°C and 50°C....100
Fig. 5.23 τ_K at 0°C, 25°C and 50°C....101
Fig. 6.1 VELOX-I vision mission load profile....110
Fig. 6.2 Population size studies using the best fit value....111
Fig. 6.3 Selection of barrier parameter studies....112
Fig. 6.4 SOC estimation comparison....113
Fig. 6.5 SOC estimation error comparison....113
Fig. 6.6 V_t estimation comparison....114
Fig. 6.7 V_t estimation error comparison....114

LIST OF TABLES

Table 2-1 Advantages and disadvantages of lithium-ion [27] 8

Table 2-2 Properties of common positive electrode materials [41] 10

Table 2-3 Electrical and energy properties of various lithium-ion chemistries [42] 11

Table 2-4 Summary of different battery models 13

Table 2-5 Governing equations of lithium-ion by porous electrode theory [46] 16

Table 2-6 Summary of SOC estimation methods 25

Table 4-1 Polynomial fit error of different polynomial order 51

Table 4-2 Identified battery parameters at 25˚C 55

Table 4-3 Proposed unit hyper sphere spherical unscented transform 59

Table 4-4 SOC estimation error performance in simulation 66

Table 4-5 Performance comparison 71

Table 4-6 Multiplication required for each operation 72

Table 4-7 Different parameters sets used in sensitivity analysis 73

Table 5-1 SOC estimation error performance 93

Table 5-2 Initial SOC error analysis at 0°C 96

Table 5-3 Initial SOC error analysis at 50°C 97

Table 5-4 Performance comparison at 0°C, 25°C and 50°C 101

Table 5-5 Multiplication comparison analysis between DUKST, UKFST and EKF 102

Table 6-1. Pseudo code of PSO with inverse barrier constraint method 109

Table 6-2 Performance comparison between proposed method, DUKFST, UKFST and EKF 114

Table 7-1. Summary of proposed methods 118

CHAPTER 1

1. INTRODUCTION

1.1 Background

Miniaturized satellites such as cubesats and nanosatellites are becoming important tools to carry out space science and technology research for educational institutions [1-5]. They are attractive for several reasons. One of which is the much reduced cost as compared to that of the conventional satellites. Among the many subsystems of satellite, an electrical power subsystem is one of the key systems [6, 7]. With advanced battery chemistries such as lithium-ion, electrical power systems can be developed with smaller form factor and lighter weight without compromising its performance [8, 9]. For a satellite, its battery must be reliable and capable of delivering the required power when needed. Once it is launched into space, maintenance or repair work is no longer feasible.

The battery state-of-charge (SOC) is the amount of energy remained as compared to its rated-energy. It provides an indication of current charge left in a battery before it has to be charged. SOC estimation is similar to the "fuel gauge" function. It has become an important issue in battery technology in terms of optimizing the battery performance by indicating the usable charge before recharging. Many types of batteries such as lithium-ion are sensitive to deep discharge or overcharge because it can lead to irreversible damage to the battery. SOC plays an important role in regulating charging and discharging process thus extending the battery life, which is vital to the power supply system used in miniaturized satellites. Reliable and accurate SOC estimation is important in managing a battery to its optimal performance level. There are many approaches to predict the SOC [10-22]. These include battery impedance based methods

(electro impedance spectroscopy), current-based (ampere-hour) methods, voltage-based methods and techniques involving Kalman filter (KF), artificial neural networks (ANN) and state observers.

1.2 Motivations

Many methods have been presented in the literature to perform SOC estimation. Most of these methods are designed for commercial usages and need to be modified for space applications. The traditional ampere-hour counting method is the simplest in terms of computational requirements and ease of implementation. It requires proper resets points in the long run to maintain the accuracy due to the nature of the open loop estimator. The ampere-hour counting method provides fairly accurate SOC estimation with proper reset points. The typical reset points are the fully charged and discharged states of the battery. This requires the battery to go through the complete charge and discharge cycle which severely affects the battery life span and shorten the satellite life span as a result. To overcome the shortcomings, it will be advantageous to have a method that can reset the SOC at any charge or discharge state. This will improve the battery life span as it will reduce the battery charge and discharge full cycle usage. The possibility of taking advantage of the satellite operating environment to help resetting the ampere-hour counting method will be investigated.

Even with the proper reset points, the ampere-hour counting method still lacks the dynamic and close loop features of model based estimation. Among the model based SOC estimation, the extended Kalman filter (EKF) is the most common. However, it has the drawbacks of linearization accuracy and Jacobian matrix derivation. A new model based SOC estimation that overcomes these shortcomings is required. Miniature satellites such as nanosatellites have limited computational power as compared to that

of the large scale satellite. It will be advantageous if a new method has reduced computational load. Most of the traditional SOC estimation methods have been performed at room temperature. For satellite applications, the temperature varies across the orbit which will affect the SOC estimation. With this consideration, temperature dependent SOC estimation is needed for satellite application.

All Kalman filter (KF) based methods are affected by measurement and process noise. In addition, they require the noise to be Gaussian in nature for optimal results. If the process and measurement noise information is not determined properly, it can lead to poor performance and affect the filter stability. Since it uses the model based approach in the estimation, battery model parameters need to be identified through experiments using a customized load profile such as pulse identification to model the battery response. To overcome these shortcomings, a method to estimate SOC without the need to identify the battery parameters and any process and measurement noise is required.

After considering these drawbacks and issues, the aim of this thesis is to propose and investigate the most suitable SOC estimation methods for a nanosatellite, using real time state estimator algorithms. This will enable the nanosatellite to operate its battery to full potential, which is vital to a satellite power supply system and its operating lifespan.

1.3 Objectives

The objectives of this thesis are as follows:

- To study different lithium-ion equivalent circuit models and select a suitable battery model for satellite applications.
- To investigate and propose new algorithms to estimate SOC of battery used in a nanosatellite.

- To investigate the temperature effect on SOC estimation and propose a new approach to include the temperature effect in the estimation.

1.4 Main contribution

The main contributions of the thesis are as follows:

- A SOC estimation method using ampere-hour counting with impulse response reset is proposed and developed in chapter 3. For this proposed approach, the impulse response is obtained from the turning on/off of satellite subsystems and payloads that occur by the satellite operations rather than using an artificial injected pulse. The charging and discharging dependency on the current have been considered and taken into account as the charge and discharge rate factor in the method. Moreover, the impulse response resets can be conducted at all SOC levels instead of the traditional fully charged and discharged state. It eliminates the risk of increasing the number of fully charged and discharged cycles thus extending the battery life span.
- A SOC estimation method using square root unscented Kalman filter (Sqrt-UKFST) with unit hyper sphere spherical transform is proposed and developed in chapter 4. The Sqrt-UKFST does not require linearization of the system. The square root characteristics improve the numerical properties of state covariances. It is also less sensitive to parameter variation than that of EKF. Spherical transform uses fewer sigma points, which reduces the computational requirement of traditional unscented transform. Besides the computational reduction, spherical transform requires only one weighting parameter instead of three required by the regular unscented Kalman filter (UKF) and the sigma points are distributed on the unit sphere model for a better controllability of

sigma point distribution. The experimental results show that the proposed method has an absolute root mean square error (RMSE) of 1.42% and an absolute maximum error of 4.96%, which are lower than those of other methods such as the ampere-hour counting, fuel gauge IC and EKF. In terms of performance improvement, it represents 37% and 44% improvement in RMSE and maximum error respectively when compared against EKF. For computational comparison, it has 32% less requirement than that of the regular UKF.

- Based on Sqrt-UKFST, a dual square root spherical unscented Kalman filter (DUKFST) SOC estimation approach with parameters update is developed to take into account of the temperature effect on battery SOC and parameters in chapter 5. The use of dual filter allows the parameter update to occur at various temperatures. The V_{OC} and SOC temperature dependency have been included in the proposed method. The noise covariance update using the scaling factor has been implemented as well. From the experimental results, the proposed DUKFST has a better performance than the Sqrt-UKFST and EKF with the lowest RMSE and the lowest maximum errors.
- A SOC estimation method based on particle swarm optimization (PSO) with an inverse barrier constraint is proposed and developed in chapter 6 to overcome the shortfalls of EKF and UKF. The PSO-based method does not require the information on the noise covariance.

1.5 Outline of Thesis

The thesis is organized as follows:

Chapter 2 gives a literature review of lithium-ion battery chemistry, modelling of the lithium-ion battery and SOC estimations methods. The electrochemical models and equivalent circuit models of the lithium-ion battery are discussed in details. The challenges and limitations of existing SOC estimation methods have been explained.

Chapter 3 presents the proposed opportunistic state-of-charge (SOC) estimation for a nanosatellite. The opportunistic SOC method makes use of satellite's operational scenarios for resetting the ampere-hour counting method and has been experimentally benchmarked against the ampere-hour counting method without resetting.

Chapter 4 proposes the Sqrt-UKFST to improve the performance of the opportunistic method in Chapter 3 and overcome the shortfalls of commonly used EKF. It also reduces the computational requirement of traditional unscented transform method. The Sqrt-UKFST has been experimentally benchmarked against the EKF, ampere-hour counting method and a commercial fuel gauge integrated circuit.

Chapter 5 presents the dual square root spherical unscented Kalman filter (DUKFST). It is proposed to take into account of the temperature factor when the satellite is in the orbit. Its experimental results are presented and compared against Sqrt-UKFST and EKF methods.

Chapter 6 presents the proposed SOC estimation method using PSO with an inverse barrier constraint. As all the KF based methods require the knowledge of measurement and process noise, this new method overcomes the shortfalls of KF as it does not require information on the process and measurement noise. For comparison, DUKFST, Sqrt-UKFST and EKF methods are used and the experimental results are presented.

Chapter 7 concludes on the research findings and discusses the future research works on new SOC estimation methods in satellites.

CHAPTER 2

2. LITERATURE REVIEW

2.1 Lithium-ion Battery Chemistry

Electrical energy plays an important part in our everyday life. Devices such as capacitors allow direct energy storage but the amount is small and its usage is limited to few applications [23, 24]. To store large amount of energy more efficiently, the conversion of energy in different forms is generally required. Electrochemical power sources such as batteries use the chemical compounds energy as storage medium and generates electrical energy back in the form of electric current through the chemical process [25, 26]. Different battery systems allow these processes to be reversed by means of charge and discharge. In general, batteries are classified as primary and secondary batteries [27, 28]. Primary batteries can convert the chemical energy into electrical once only whereas secondary battery is designed to perform the processes repeatedly.

Among the different battery chemistries, the lithium-ion battery is becoming one of the most promising energy storage technology. It has been widely used in many applications such as portable electronics, electric vehicles (EVs) and satellite [29-32]. The main reason behind such a rapid growth is the outstanding high energy density and long cycling performance. The high energy density makes it attractive for applications where weight or volume are important (e.g., EVs and satellites) [29, 33]. Lithium-ion battery also has a long cycle life of more than 500 cycles and low self-discharge rate of less than 10% per month [34, 35]. It does not suffer the memory effect likes nickel-cadmium (NiCd) and nickel metal hydride (NiMH) batteries. Recent demands on energy

and environmental sustainability have even further spurred great interest in a larger scale lithium-ion battery system as complimentary energy storage for renewable energy resources, such as solar and wind power [36, 37]. The comparison between different chemistries in terms of energy density is shown in Fig. 2.1 [38]. The advantages and disadvantages of lithium-ion are summarized in Table 2-1 [27].

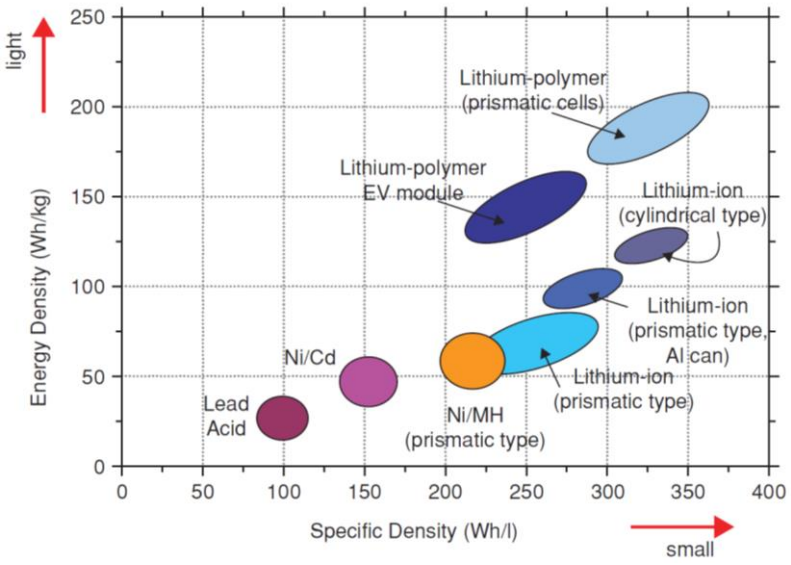

Fig. 2.1 Comparison with different battery chemistries in terms of gravimetric and volumetric energy densities [38]

Table 2-1 Advantages and disadvantages of lithium-ion [27]

Advantages	Disadvantages
• Sealed cells: no maintenance required • Long cycle and shelf life • Broad temperature range of operation • Low self-discharge rate • Rapid charge capability • High rate and high power discharge capability • High coulombic and energy efficiency • High specific energy and energy density • No memory effect	• Moderate initial cost • Degrades at high temperature • Need for protective circuitry • Capacity loss or thermal runaway when over-charged • Venting and possible thermal runaway when crushed • Cylindrical designs typically offer lower power density than NiCd or NiMH

The energy storage mechanism of lithium-ion batteries comprises the negative (anode) and positive (cathode) electrodes with the electrolyte providing a conductive medium for lithium-ions to move between the electrodes. Both electrodes allow lithium-

ions to move in and out of their interiors. Fig. 2.2 shows the electrochemical process of a lithium-ion battery during charging and discharging process.

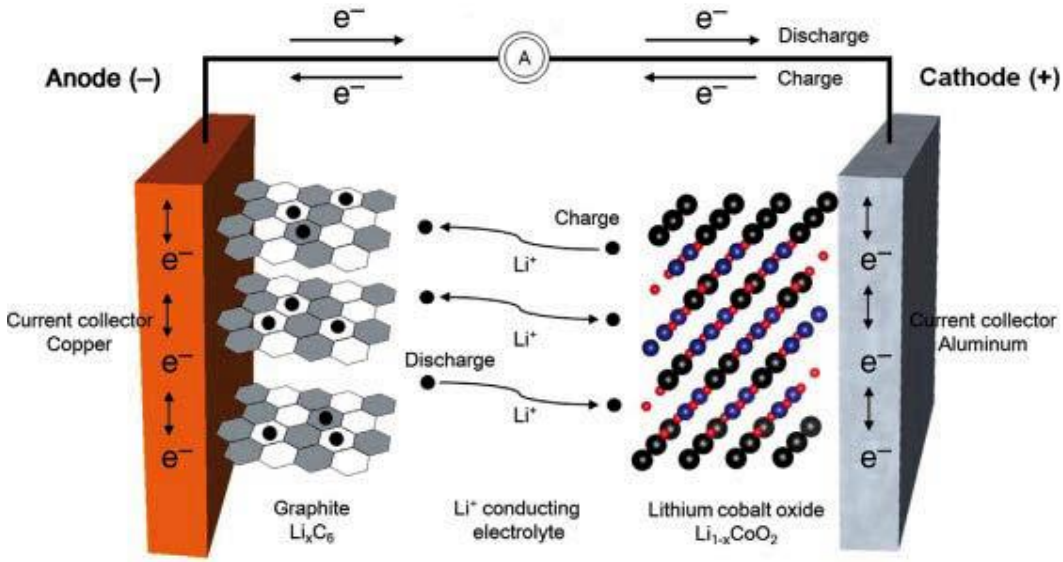

Fig. 2.2 Schematic of electrochemical process of lithium-ion cell [39]

In Fig. 2.2, lithium cobalt oxide ($Li_{1-x}CoO_2$) and graphite (Li_xC_6) are the cathode and anode active materials respectively. Liquid or gel-polymer electrolytes allows lithium-ions (Li^+) to move between the positive and negative electrodes. On charging, Li^+ ions are de-intercalated from the layered $LiCoO_2$ cathode host, transferred across the electrolyte, and intercalated between the graphite layers in the anode. In the positive electrode during charge, the active material is oxidized as follows:

$$LiCoO_2 \underset{\text{discharge}}{\overset{\text{charge}}{\rightleftharpoons}} Li_{1-x}CoO_2 + xLi^+ + xe^- \tag{2.1}$$

In the negative electrode during charge, the active material is reduced. Lithium-ions that migrate from the positive electrode and through the electrolyte and separator are intercalated in the reaction as

$$C + xLi^+ + xe^- \underset{\text{discharge}}{\overset{\text{charge}}{\rightleftharpoons}} Li_xC \tag{2.2}$$

The overall chemical reaction can be written as

$$LiCoO_2 + C \underset{\text{discharge}}{\overset{\text{charge}}{\rightleftharpoons}} Li_xC + Li_{1-x}CoO_2 \quad (2.3)$$

The discharge reverses this process where the electrons pass around the external circuit to power the connected circuitry. These reactions produce a theoretical cell voltage of 4.1V, and is much higher than Ni–MH or Pb–acid cells [40]. The favourable electrochemical performance in energy and power densities have made the early lithium-ion battery a great success for various applications in spite of the remaining challenges. Depending on the materials used for the anode and cathode, various types of lithium-ion batteries with different electrical and energy properties can further be obtained as well. Table 2-2 summarizes the common positive electrode materials [41] and Table 2-3 shows the resultant electrical and energy properties of the various lithium-ion chemistries [42].

Table 2-2 Properties of common positive electrode materials [41]

Material	Chemical formula	Description
Lithium cobalt oxide (LCO)	$LiCoO_2$	Original commercial type; expensive raw materials
Nickel cobalt aluminium (NCA)	$LiNi_{0.8}Co_{0.15}Al_{0.05}O_2$	Highest energy density per unit mass
Nickel manganese cobalt (NMC)	$LiNi_{1-x-y}Mn_xCo_yO_2$	Safer and less expensive than LCO
Lithium manganese oxide (LMO)	$LiMn_2O_4$	Safer and less expensive that LCO, but poor high temperature stability
Lithium-ion phosphate (LFP)	$LiFePO_4$	Very safe, high power, but lower energy density. Best high-temperature stability

Table 2-3 Electrical and energy properties of various lithium-ion chemistries [42]

Positive electrode	LCO and NCA	NMC	LMO	$LiFePO_4$	
Negative electrode	Graphite	Graphite	Graphite	Lithium titanate	Graphite
Optimized for	Energy	Energy or Power	Power	Cycle life	Power
Operating voltage range	2.5-4.2 (rarely 4.35)	2.5-4.2 (rarely 4.35)	2.5-4.2	1.5-2.8	2.0-3.6
Nominal voltage	3.6-3.7	3.6-3.7	3.7-3.8	2.2	3.3
Specific energy (Wh/kg)	175-240 cyl 130-200 polymer	100-240	100-150	70	60-110
Energy density (Wh/L)	400-640 cyl 250-450 polymer	250-640	250-350	120	125-250
Discharge rate (continuous)	2-3C	2-3C (power cells > 30C)	>30C	10C	10-25C
Cycle life (100% DOD to 80% capacity)	500+	500+	500+	4000+	1000+
Ambient temperature during charge (°C)	0-45	0-45	0-45	-65	0-45
Ambient temperature during discharge (°C)	-80	-80	-90	-90	-90

2.2 Modelling of Lithium-ion Battery

When describing a battery cell reaction, two groups of thermodynamic and kinetic parameters are used. Thermodynamic parameters describe the system when the chemical reactions are balanced. In other words, there is no current flow and the battery is in equilibrium state. When chemical reactions occur in the battery, kinetic parameters are used. The parameters include mass transport via migration or diffusion and voltage drop caused by the current flow in electrons. They are required in order to move the chemical reactants to the electrodes surface. Through the use of thermodynamic and kinetic parameters, various battery models have been proposed in literature. The two

most commonly used techniques for modelling batteries are electrochemical modelling and equivalent electric circuit. Electrochemical modelling is mainly based on highly nonlinear equations to describe the battery electrochemical aspects. As such, they can describe battery systems in great details and are considered the most accurate. Equivalent circuit models describe the battery using electrical components only. They are much simpler than the electrochemical models but lack the details. Using non-linear components such as diode in equivalent circuit models [43] or a combination of electrochemical and equivalent circuit modelling [44, 45] have been used to model the battery as well. A summary of different battery model categories under electrochemical and equivalent circuit categories are listed in Table 2-4.

Table 2-4 Summary of different battery models

Category	Models	Advantages	Disadvantages
Electrochemical Model	Nernst, Butler-Volmer, Peukert Equation, Shepherd Model Equation etc.	Describe battery electrochemical operations accurately.	Time consuming. Complex mathematical equations. Not suitable for estimation and control purposes.
Equivalent Circuits Models	Impedance Models	State-of-health (SOH) estimation	Requires AC impedance. Linear model assumption of batteries. Computationally complex. Electrochemical impedance spectroscopy (EIS) is dependent on temperature, SOC, current and SOH. Lacks of run time information on battery. Limited modelling accuracy on transient response.
	Resistive (R_{int}) Model	Simplest model.	Unable to capture battery dynamic responses. Lack of temperature and cycle usage effects.
	Thevenin Models	Suitable for control and simulation. Able to capture battery dynamic operations more accurately than R_{int}.	Lack of temperature and cycle usage effects. Computational complexity increases with additional *RC* networks. Lacks of run time information on battery.
	Run Time Based Model	Battery run time information	Computationally complex.

2.2.1 Electrochemical models

Unlike equivalent circuit models, the electrochemical models are able to accurately represent the chemical processes that take place in the battery. The electrochemical model describes the battery internal process in details and is considered the most

accurate among the different modelling methods [46]. However, it comes with heavy computational requirements. Among different electrochemical battery models, the lumped parameter model and porous electrode theory model are two of the most popular methods.

In the lumped parameter model, the battery internal operations are described by a set of differential algebraic equations (DAEs) using Nernst's theory and the Butler-Volmer equation while assuming a uniform spatial distribution of chemical products. Nernst's theory describes the open-circuit potential of the battery using the relationship between the electric potential of electrode and electrical charge [47]. Thus, the electrical potential $\phi(t)$ of an electrode using the Nernst's equation can be described as

$$\phi(t) = \phi^0 - \frac{RT}{nF} \ln\left(\prod_k (m_k(t)\gamma_k)^{\nu_k} \right) \tag{2.4}$$

where ϕ^0 *is the* electromotive force at standard conditions, R is the universal gas constant, T is the absolute temperature, n is the number of electrons, F is the Faraday's constant, k subscript represents the k^{th} reactants, m is the molality, γ is the activity coefficient and ν is the stoichiometric coefficient. The Butler-Volmer equation describes the relationship between battery current density $J(t)$ and over-potential or polarization $\eta(t)$ *as* [40]

$$J(t) = J_0 \left[\exp\left(\frac{\alpha F}{RT} \eta(t) \right) - \exp\left[\frac{(1-\alpha)F}{RT} \right] \eta(t) \right] \tag{2.5}$$

where α is the charge transfer coefficient, and J_0 is the exchange current density. The advantage of the lumped battery model is that the resultant equations are simple and easy to integrate yet still gives a fast and accurate battery models for automotive and control applications. Although the approach of using simple DAEs gives good accuracy for the early primary and secondary battery models of Pb-acid [48] and NiMH [49, 50]

cells, it is insufficient to describe the most modern batteries such as lithium-ion. Usage of new electrode materials and battery design results in more complex electrochemical processes requiring more complex models to describe modern batteries. For example, the spatial distribution of lithium-ion between the electrodes needs to be modelled for lithium-ion batteries and this is one area where lumped parameter falls short.

In [51-54], the porous electrode theory based model has been used to describe lithium-ion batteries. Porous electrode theory is able to describe a battery system in much more details than the lumped battery models as it takes into account of most of the electrochemical processes such as mass diffusion, side reactions, temperature effects and battery ageing. As such, porous electrode based models have become the standard for most of the modern battery modelling technique. It has even been used for generating of data required to validate battery models [46]. Unlike the lumped parameter based approach, partial differential equations (PDEs) are used in porous electrode theory. The porous electrode approach uses the Nernst and Butler-Volmer equations. Its PDEs use Fick's and Ohm's laws for diffusion of active materials concentration and electric potentials distributions. The PDEs are derived using a simplified one-dimensional spatial cell structure as shown in Fig. 2.3.

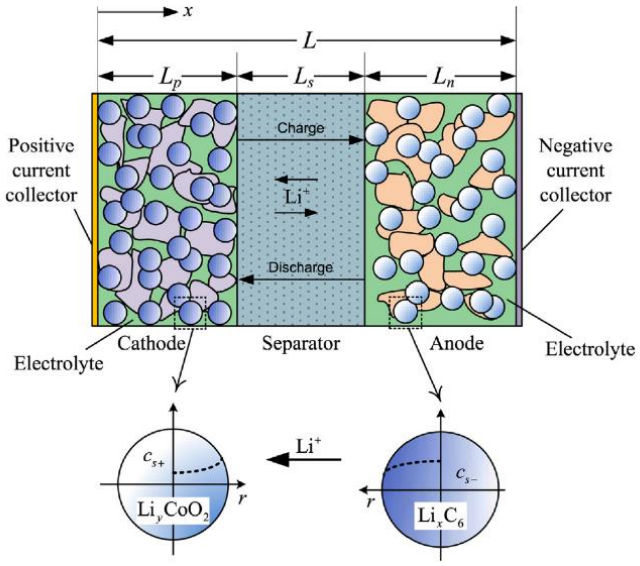

Fig. 2.3 Anatomy of 1D lithium-ion cell [46]

Specifically, the PDEs that describe the electrochemical processes of Li^+ ions are given[1] in Table 2-5.

Table 2-5 Governing equations of lithium-ion by porous electrode theory [46]

Changes in lithium-ion concentration in solid and liquid phase	$\frac{\partial c_{s,k}(x,r,t)}{\partial t} = \frac{D_{s,k}}{r^2}\frac{\partial}{\partial r}\left(r^2\frac{\partial c_{s,k}(x,r,t)}{\partial t}\right)$ $\varepsilon_k\frac{\partial c_{e,k}(x,t)}{\partial t} = \frac{\partial}{\partial x}\left(D_{eff,k}\frac{\partial c_{e,k}(x,t)}{\partial x}\right) + a_k(1-t_+)J_k(x,t)$
Solid phase charge conservation	$\sigma_{eff,k}\frac{\partial^2\Phi_{s,k}(x,t)}{\partial x^2} = a_k F J_k(x,t)$
Boundary conditions	$-\sigma_{eff,p}\left.\frac{\partial\Phi_{s,p}}{\partial x}\right\|_{x=0} = -\sigma_{eff,n}\left.\frac{\partial\Phi_{s,n}}{\partial x}\right\|_{x=L} = I$ $-\sigma_{eff,p}\left.\frac{\partial\Phi_{s,p}}{\partial x}\right\|_{x=L_p} = -\sigma_{eff,n}\left.\frac{\partial\Phi_{s,n}}{\partial x}\right\|_{x=L_p+L_s} = 0$

[1] The similar notations of the equation in [45] are used here.

Effective electronic conductivity	$\sigma_{eff,k} = \sigma_k \left(1-\varepsilon_k-\varepsilon_{f,k}\right)$ $-\sigma_{eff,k}\frac{\partial \Phi_{s,k}(x,t)}{\partial x} - k_{eff,k}\frac{\partial \Phi_{e,k}(x,t)}{\partial x} + \frac{2k_{eff,k}(x,t)RT}{F}\left(1-t_+\right)\frac{\partial \ln c_{e,k}}{\partial x} = I$
Butler-Volmer equation [55]	$J_k(x,t) = 2K_k \left(c_{s,k,\max} - c_{s,k,surf}\right)^{0.5} \left(c_{s,k,surf}\right)^{0.5} c_{e,k}^{0.5}(x,t)$ $\times\left[\exp\left(\frac{0.5F}{RT}\mu_{s,k}(x,t)\right) - \exp\left(-\frac{0.5F}{RT}\mu_{s,k}(x,t)\right)\right]$

These partial differential algebraic equations (PDAEs) are defined for each electrode and electrolyte region individually and are coupled with each other by the continuity in the boundary conditions. Using the diffusion law, the changes in lithium-ion concentration PDAE is able to describe battery dynamics response more accurately than the traditional RC network in the equivalent circuit model. Battery operational usage is greatly affected by temperature variation and it is beneficial if it is able to incorporate temperature effect accurately in order to improve the battery capability. The porous electrode model is able to capture the temperature effect accurately by including temperature *T* in the equations. With the detailed electrochemical model, accurate prediction of power and behaviour from a battery is possible. This allows the battery to be operated more aggressively while ensuring the battery safety conditions. However, solving these equations in real time for control purposes is nontrivial and it requires complex methods with high computational requirement. As such, the electrochemical models are time consuming and computationally complex in terms of simulation and real time purposes. In order to reduce the computational load and complexity, different model reduction methods such as reducing the model order or number of unknowns have been implemented [56, 57]. These still require substantial computational

requirement when compared against equivalent circuit models and they are not suitable for real time systems.

2.2.2 Equivalent circuit models

Unlike the electrochemical models presented in section 2.2.1, the equivalent circuit models use only electrical components to describe the battery internal dynamics of the electrochemical processes. Although they do not provide as much details as the electrochemical models, they are still able to capture basic characteristics of battery chemistry and can be easily incorporated for real time applications due to its relatively simple computational requirement. Thus they are more suited to control and circuit simulation environments [58, 59].

The simplest equivalent circuit model is the resistive model [60] as shown in Fig. 2.4 and its electrical equations can be written as (2.6).

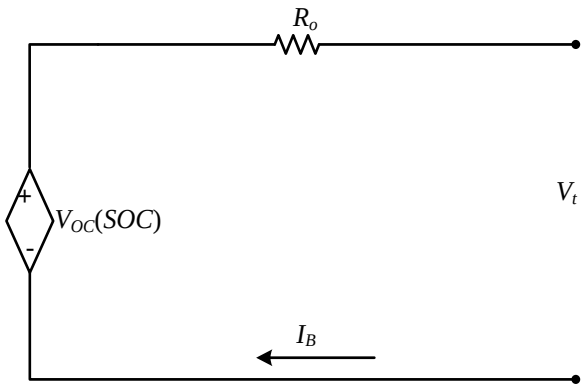

Fig. 2.4 Resistive R_{int} model

$$V_t = V_{OC} - I_B R_o \tag{2.6}$$

where V_t is the battery terminal voltage and I_B is the battery current. The model consists of only one resistor and one ideal voltage source. The ideal voltage source V_{OC} represents the battery open-circuit voltage (OCV) and it is a function of battery state-of-charge (SOC). R_o is the ohmic resistance of the battery. Although it is the simplest

among the equivalent circuit battery models, it lacks the ability to model the battery transient (relaxation effects) and dynamic operations during charging and discharging.

To improve the accuracy of resistive model, more electrical components such as resistors and capacitors networks can be added. These improved models can be divided into two categories: impedance and Thevenin models. For impedance models, electrochemical impedance spectroscopy (EIS) is used to describe the battery operations [61, 62]. Injecting an AC current into the battery, its responses are modelled by the battery complex impedance function in frequency domain. Fig. 2.5 presents a battery half-cell describing the chemical reactions at one of the electrodes using a Randles circuit. The electrical components used in the circuit include electrode inductance L, internal resistance R_i, charge transfer resistance R_{ct} and double layer capacitance C_{dl}. The component Z_w is a constant-phase Warburg element which represents the diffusion effects. However, the need of AC current and the dependency of EIS on SOC, current, temperature and battery usage increases the computational complexity of impedance based models.

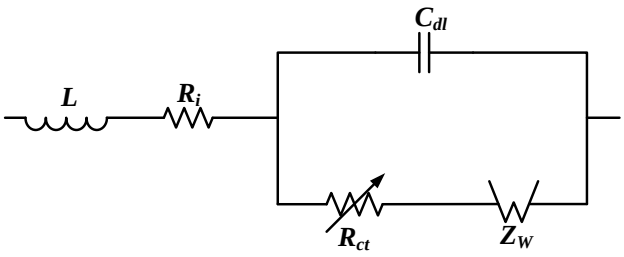

Fig. 2.5 Half-cell EIS circuit

For Thevenin models, a series of resistor and capacitors networks are added to model the transient response in terms of charge depletion and recovery during charging and discharging. Charge depletion occurs when the battery starts to discharge. Due to the highly concentrated chemical reactants near the anode and cathode at the start, the initial voltage drop is subdued. Then it gradually decreases as time increases [63]. The

charge recovery occurs in the opposite manner of charge depletion when the battery starts to charge or discharging stops. This is from diffusion effects within the cathode and anode in the battery [63]. The charge depletion and recovery effects from a discharge current pulse is shown in Fig. 2.6. Fig. 2.7 shows the Thevenin models with *n* number of RC networks. Depending on the required accuracy and complexity, one can choose how many RC networks to be included in the model [59, 64].

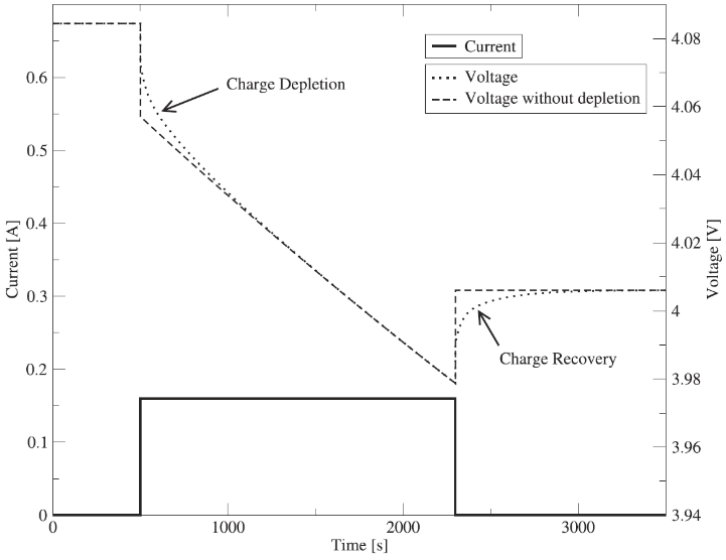

Fig. 2.6 Battery charge depletion and recovery effect during a discharge pulse [46]

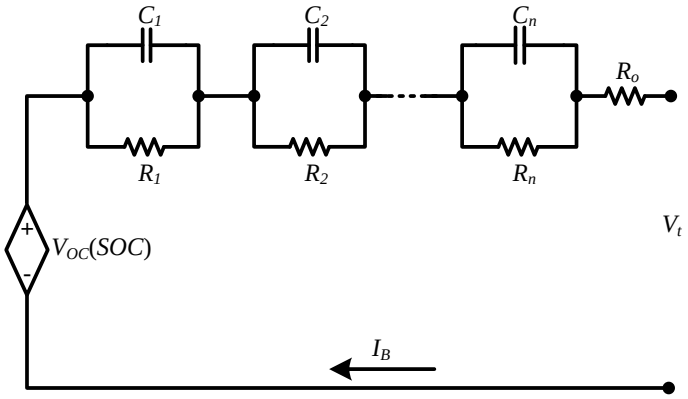

Fig. 2.7 Dynamic Thevenin RC models

Currently, the most commonly used Thevenin models are Thevenin and improved Thevenin models [65]. The Thevenin model is shown in Fig. 2.8 with only one RC network. It can model the transient effects during charging and discharging better than

the resistive model. However, it falls short in modelling the responses at the end of fully charged/discharged stage. The electrical characteristic equation can be written as

$$\dot{V}_1 = \frac{-V_1}{R_1 C_1} + \frac{I_B}{C_1} \tag{2.7}$$

$$V_t = V_{OC} - V_1 - I_B R_o \tag{2.8}$$

where V_1 is the voltage across the RC network and R_1 and C_1 represent the RC circuit components in the model.

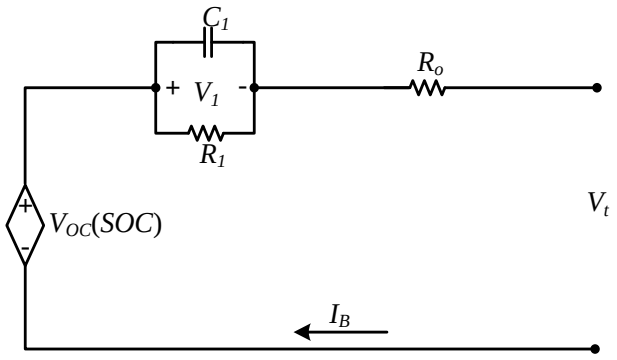

Fig. 2.8 Thevenin model

To further improve the accuracy of Thevenin model, an additional RC network can be added resulting in improved Thevenin or a double polarization model as shown in Fig. 2.9. With an additional RC network, it is able to capture the transient responses more accurately than the Thevenin model at the fully charged/discharged state.

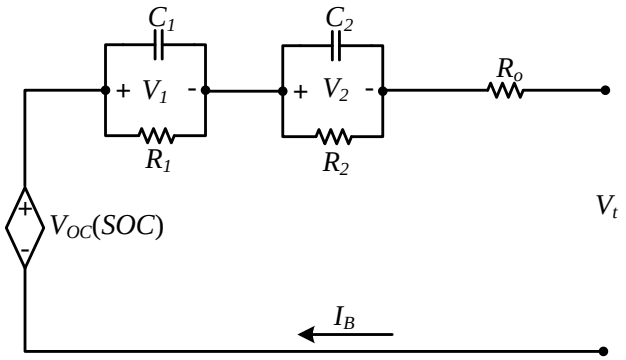

Fig. 2.9 Improved Thevenin or double polarization model

The electrical characteristics of the model can be written as

$$\dot{V}_1 = -\frac{V_1}{R_1 C_1} + \frac{I_B}{C_1} \tag{2.9}$$

$$\dot{V}_2 = -\frac{V_2}{R_2 C_2} + \frac{I_B}{C_2} \tag{2.10}$$

$$V_t = V_{OC} - V_1 - V_2 - I_B R_o \tag{2.11}$$

where V_1 and V_2 represent the voltages across the two RC networks and R_1, C_1, R_2 and C_2 represent the two RC circuit components.

Although Thevenin based models can accurately capture the battery dynamic operations, it lacks information on battery run time such as capacity which can be affected by ageing and charge and discharge current. In order to include this information, the run time based model has been proposed in [66-68].

Fig. 2.10 shows the runtime based electrical model of the lithium-ion battery. It uses an additional complex circuit network combined with dynamic Thevenin models to include additional variable components such as battery self-discharge, $R_{Self\text{-}Discharge}$ and capacity, $C_{Capacity}$.

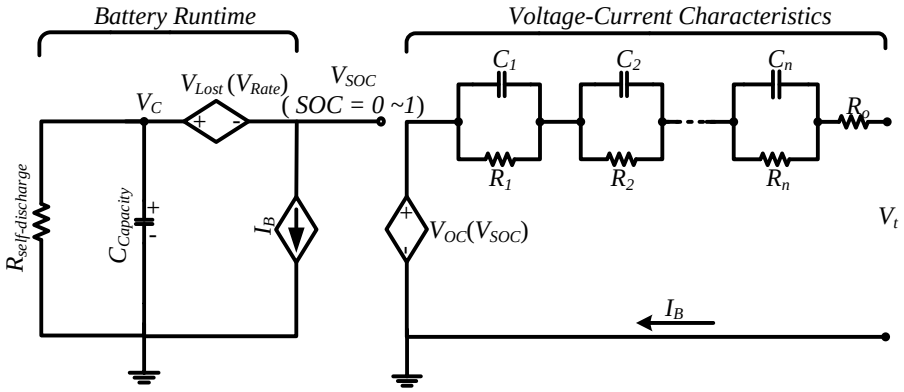

Fig. 2.10 Runtime based electrical model

The electrical characteristics can be written as

$$\dot{V}_{SOC} = -\frac{V_{SOC}}{R_{self-discharge}C_{Capacity}} - \frac{I_B}{C_{Capacity}} \tag{2.12}$$

$$\dot{V}_i = -\frac{V_i}{R_i C_i} + \frac{I_B}{C_i} \tag{2.13}$$

$$V_t = V_{OC} - V_1 - V_2 - ..... - V_n - I_B R_o \tag{2.14}$$

where $i = 1, ..., n$.

The voltage-current characteristic modelling is the same as the dynamic Thevenin model as seen in (2.13) and (2.14). One added feature is that the battery SOC is now a function of self-discharge and capacity which can also be updated to estimate the battery life time. However, it comes with increased computational complexity and the modelling of the relationship between capacity and SOC is no easy task. The manner in which the battery capacity varies is also dependent on many factors such as the battery operating environment, depth of discharge level and charge/discharge current rate [69].

In this thesis, the Thevenin based equivalent circuit modelling method is used due to its advantages of simpler computational complexity, transient response capabilities

and more suited for control and simulation purposes over the electrochemical modelling method. The details of the model will be explained further in chapter 3.

2.3 State-of-Charge (SOC) Estimation Methods

In chapter 1, it has been mentioned that high energy density, low self-discharge and lack of memory effects have made lithium-ion batteries the preferred choice over other battery chemistries such as NiMH and Pb-acid for many applications. However, they require high safety requirement during operation. Overcharging or over discharging a lithium-ion battery can cause permanent damage to the battery. A battery management system (BMS) is an important part in any battery operated system. It ensures an optimal and reliable battery operation through monitoring different aspects of batteries such as state-of-charge (SOC) and state-of-health (SOH). SOC can simply be defined as the remaining capacity or charge of the battery in percentage with respect to total capacity of the battery. SOC estimation is one of the most important aspects of the modern battery management system. For satellite applications, it is important to have accurate knowledge of present condition of the battery. Accurate and reliable SOC estimation provides the current state of the battery and enables batteries to be safely charged and discharged. It also prevents uninterrupted system shutdown of the satellite. Since the battery is an electrochemical energy storage system, SOC cannot be measured directly and it needs to be estimated from the battery voltage and current measurements. Many SOC estimation approaches have been presented in the literature [10-22]. They can be classified into different categories such as ampere-hour counting and model-based estimations. The summary of different SOC estimation methods is shown in Table 2-6.

Table 2-6 Summary of SOC estimation methods

Category	Methods	Advantages	Disadvantages
Ampere-hour counting	Current [21, 70-72]	Simple computational complexity. Ease of implementation.	Open loop estimation. Needs periodic resets and highly accurate sensors.
Open-circuit voltage-based estimation	Voltage [73-79]	Simple computational complexity.	Sensitive to battery and operation conditions. Needs long rest time (current = 0). Temperature dependent.
Model-based estimation	Kalman filter [80-98] Observers [67, 99-117] Artificial neural networks [118-129] Fuzzy logic [22, 127-131] and support vector machine [132-136]	Dynamic. Accurate battery electrochemical processes if used with electrochemical models. Temperature and ageing factor update is possible. Improved battery nonlinearity when using computational intelligence methods.	Needs accurate battery model. Noise statistics needed for Kalman filters. Linearization accuracy. Time consuming in both algorithms and models. Needs large training data. Dependent on quality of training data sets and membership functions are highly subjective for machine learning methods. Heavy computational burden for computational intelligence methods.
Impedance-based estimation	Electrochemical impedance spectroscopy (EIS)[14, 43, 137-144]	Gives information on SOH.	Dependent on temperature and ageing. More suited for offline and laboratory. Cost sensitive.
Estimation using special measurement techniques	Battery magnetic characteristics [145-147]	More measurement available than traditional current, voltage and temperature.	Additional sensor is expensive. Moderate accuracy compared with other model-based methods. No proof of battery effect on battery magnetic characteristics

For ampere-hour counting method, it simply measures the current flowing in and out of the battery. The ampere-hour counting can be expressed as:

$$SOC_t = SOC_{t-1} - \int_t^{t+1} \frac{\eta I(t)}{Capacity}\,\Delta t \tag{2.15}$$

where η is the Coulomb efficiency and Δt is the sampling time. When the battery capacity is known and the battery current can be measured accurately, it can provide accurate SOC estimation. However, this requires information on initial SOC and highly accurate sensors which can be costly. With no feedback loop involved, ampere-hour

counting is considered an open loop estimator and the accumulated measurement errors can give erroneous SOC estimation if it is operated in the long term. Additional calibration or reset points are needed to maintain its accuracy [70-72]. One example is the use of end of charge and discharge voltage, which is highly dependent on battery current and parameters [21]. The requirement of end of charge and discharge voltage increases battery fully charge and discharge cycle and it can severely shorten the battery life span.

The OCV-based SOC estimation takes advantage of the intrinsic relationship between OCV and SOC of the battery. For the OCV to be measured accurately, the battery needs to be relaxed for a long time. Nonetheless, there are methods for the estimation of OCV under a limited amount of time. In [73], it uses an empirical formula to estimate OCV using the parameters obtained from laboratory experiment. These parameters extraction is conducted using a new battery only and the accuracy diminishes once battery ages. To overcome the decline in conjunction with battery ageing, OCV estimation using adaptive methods have been reported in [74-76] with OCV relaxation model. Using the model, the OCV parameters are identified through curve fitting whenever the current is interrupted each time. One example of the voltage relaxation model is as follows [76]:

$$V_{OCV}(t) = EMF - \left(EMF - V_{OCV}\left(t=0\right)\right)e^{-t/\tau} \tag{2.16}$$

where *EMF* represents the equilibrium battery voltage at the end of the relaxation period, V_{OCV} represents any battery voltage measured under open-circuit condition (battery current is zero) and τ represents the time constant of the relaxation model. The advantage of the function is the required *EMF* and τ can be identified easily. However, the resultant approximation is very inaccurate [76]. Moreover, these methods need the battery to be

rested at one stage and this is not possible for applications such as satellite where batteries are used constantly [77, 78]. Furthermore, the OCV and SOC relationship is affected by the operating temperature which varies across the orbit of a satellite.

For model-based estimation methods, the approach is to make use of battery measurements such as voltage, current and temperature for SOC estimation using the OCV-SOC relationship or direct estimation with the battery model. The models could be electrochemical or equivalent circuit models. Equivalent circuit models are more popular for model based estimation due to its simplicity. The main shortfall of the equivalent circuit model is the requirement of model parameters update to deal with ageing batteries. The most commonly used model technique is the Kalman filter based method such as extended Kalman filter (EKF) [80-91]. The main disadvantage of EKF is the linearization of battery nonlinearity. Although unscented Kalman filter (UKF) and central difference Kalman filter have been used to reduce the linearization error [92-96, 148], all Kalman filter based methods require information on measurement and process noise. Inaccurate information might lead to poor performance in convergence or filter stability. The assumption of the Gaussian noise in nature might affect convergence and accuracy as it may not be valid in real applications. Instead of Kalman filter, H_∞ and particle filter have been used in SOC estimation to overcome those shortfalls [99-104]. However, computational requirement of these filters are high, and they can be up to a factor of 50 when compared with UKF [103]. The improvement in performance is rather modest as compared to EKF.

Various observer based methods such as sliding mode observers, Luenberger observer and adaptive observer have been presented in [67, 105-116]. Although the sliding mode observer can handle the nonlinearity effects well, its performance deteriorates when there is noise in the output. Adaptive feature is added in these

observers to tackle battery ageing but it comes with increased computational complexity. Moreover, observers combined with ampere-hour counting and recursive least-square-based filters such as windows least square [79, 149-151] have been implemented in model-based SOC estimations as well. These methods are simpler yet they can give significant divergence problems when the battery model accuracy deteriorates.

The electrochemical models can be used to improve the accuracy in battery modelling for the model-based methods of EKF, sigma-point Kalman filter and partial differential equation (PDE) observer and multi-rate particle filter but they come with higher computational complexity, which also limits the parameters available to improve the battery ageing factor [152-160]. As some battery parameters are dependent on SOC, impedance spectroscopy has been used in SOC estimation [14, 43, 137-143]. However, it requires the battery impedance to be measured with AC voltage and current, which makes it more suited for laboratory tests [43, 141]. Battery parameters vary greatly when battery ages and is dependent on temperature, which can affect the estimation accuracy.

Computational intelligence and machine learning methods such as artificial neural networks (ANN), fuzzy logic and support vector machines (SVM) have been implemented in SOC estimations. The ANN methods can be further divided into the ANN based SOC estimation and the ANN method combined with the previously mentioned methods such as EKF and observer [118-129]. It has even been used in conjunction with ampere-hour counting. An ANN based SOC estimation is similar to the model-based SOC estimation. Instead of using an electrical model to model SOC, it uses ANNs to describe the relationship of SOC. Its advantage is that it does not require the detailed knowledge of battery behaviour. However, large training data sets are required to train these ANN and the ANN estimation method trained using the new

battery cannot give a reliable SOC estimation of the aged battery. Due to the open loop nature of this approach, the online training or updating of ANN is not feasible. To make closed loop estimation, ANNs based methods have been combined with neuro-controller [121] and Kalman filter methods [122-125]. One of the major advantages from these over ANNs based methods is that theoretically it allows online training of ANNs during battery operations. Its main drawback is the need of large training data sets for over fitting the model. Fuzzy based neural networks such as radial basis function neural networks (RBFNN) [22, 127-131] and support vector machines (SVM) [132-136] based approaches are similar to ANNs and have the same disadvantages mentioned previously. Overall, computational intelligence and machine learning methods can capture battery nonlinearity feature better but the computational complexity is higher. The accuracy is highly dependent on the quality and amount of training data. Most battery management systems make use of three available measurements, namely voltage, current and temperature. In [145-147], SOC estimation is conducted with the additional battery magnetic sensors measurement. It models the magnetic characteristic as the SOC indicator. However, it is unclear if the battery magnetic characteristics is affected by ageing. Similar to ampere-hour counting, it needs an expensive sensor and achieves only moderate accuracy.

2.4 Summary

In this chapter, a literature review of battery modelling and various SOC estimation methods have been presented. Lithium-ion battery chemistry was first presented for better understanding the battery intrinsic operations. Based on these chemical reactions, two most common modelling methods namely the electrochemical and equivalent circuit methods have been introduced. As the equivalent circuit models are able to

provide the required accuracy and details with relatively simpler computational requirements than those of electrochemical based methods, it is adopted in this thesis.

Among the SOC estimation methods, ampere-hour counting is the simplest but suffers from accumulated errors. Moreover, it needs the battery to be fully charged and discharged for reset points. Voltage based methods such as OCV requires the battery to be rested at certain stage which is not possible for satellite applications. Kalman filters such as EKF requires linearization and Gaussian noise information for optimal results.

Ampere-hour counting could achieve good estimation provided accurate periodic calibration or resetting points are conducted regularly. Since the traditional reset points are detrimental to battery lifespan, resetting of ampere-hour counting method at all SOC level should be performed. A new approach named opportunistic SOC estimation has been investigated and will be presented in chapter 3. To improve the shortfalls of EKF and computational cost of traditional unscented transform, the UKF and spherical unscented transform with unit sphere will be studied and presented in chapter 4. Most of the reported SOC estimation methods assume that the battery is operating at room temperature with constant battery parameters. Since satellite operating temperature varies across the orbit, temperature effect on SOC estimation needs to be considered. This is discussed in chapter 5.

CHAPTER 3

3. OPPORTUNISTIC STATE-OF-CHARGE ESTIMATION

3.1 Introduction

A new SOC estimation method using ampere-hour counting with impulse response reset from different satellite's operating scenarios is presented in this chapter. Due to the advantages as mentioned in chapter 2, lithium-ion batteries have been used widely as the energy source for satellite applications [8, 32]. Unlike the consumer electronics applications, servicing of satellite hardware is infeasible once it is launched. Consequently, the safety and reliability is of paramount important in satellite applications. Estimation of battery state-of-charge (SOC) is one of the critical tasks in battery management and control of the satellite power subsystem. Lithium-ion batteries are sensitive to overcharge and/or deep discharge. This can lead to permanent damage to the batteries, which compromises its performance and life span of the satellite mission. Accurate and reliable SOC estimation provides the current state of the battery and enables it to be safely charged and discharged. It also prevents system shutdown, which can severely affect the satellite operation.

Among the SOC estimation methods presented in chapter 2, the ampere-hour counting method is the most popular due to its simplicity and low computational cost. However, its performance depends on the sensor accuracy, the initial error and the accumulated measurement errors. Due to its reliance of integration and open loop nature, errors in terminal measurements due to noise, resolution, and rounding are accumulative. The accumulated measurement errors can give erroneous estimation as high as 25% [148]. These drawbacks can be overcome by a proper removal of integral

errors. Many researchers have used voltage measurements at fully charged/discharged state to remove the accumulated errors [21, 70]. However, it is not an easy task to determine if the voltage is at fully charged and discharged state as it is highly dependent on current magnitude. The need for frequent fully charge and discharge of the battery would severely affect its battery lifespan. The proposed method performs the resetting at different SOCs via impulse response obtained from the opportunity when the satellite subsystems are turned on/off instead of artificially injecting a pulse. The resetting can be conducted at all SOC levels instead of fully charged/discharged state.

3.2 Modelling of Lithium-ion Batteries

Different modelling methods to describe the internal characteristics of battery have been presented in chapter 2. A summary of different battery models can be found in Table 2-4. In the sequel, the double polarization equivalent circuit model is used. Fig. 2.9 in section 2.2.2 shows the equivalent circuit model of the battery and is shown here as Fig. 3.1.

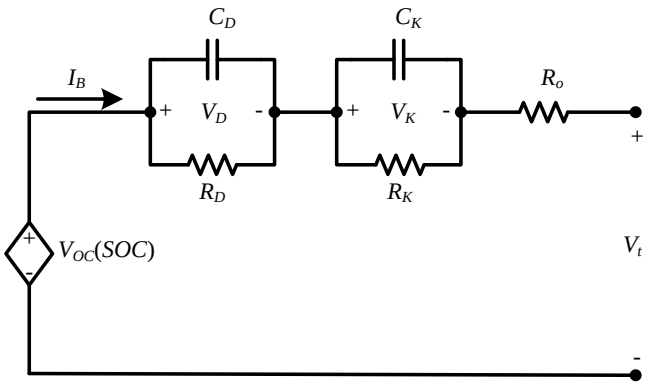

Fig. 3.1 Equivalent circuit model of lithium-ion battery

In Fig. 3.1, V_{OC}, V_t and I_B represent the battery open-circuit voltage, battery output voltage and battery current respectively. The resistor R_o represents the instantaneous voltage drop during the battery charge and discharge process. The two RC networks describe the transient response (also known as relaxation effect) during the discharge

and charge process. R_D and C_D represent the diffusion process whereas R_K and C_K represent the kinetic reaction. As presented in section 2.2.2, the voltage relationship equations can be obtained by using Kirchhoff's voltage law as follows:

$$\dot{V}_D = -\frac{V_D}{R_D C_D} + \frac{I_B}{C_D} \tag{3.1}$$

$$\dot{V}_K = -\frac{V_K}{R_K C_K} + \frac{I_B}{C_K} \tag{3.2}$$

$$V_t = V_{OC} - V_D - V_K - I_B R_o \tag{3.3}$$

The identification of the battery parameters in Fig. 3.1 will be discussed in the next section.

3.2.1 Battery parameters identification

The battery parameters (R_o, R_D, R_K, C_D and C_K) can be obtained by using the pulse charging and discharging method and they are used to calculate the battery rate factor [161, 162]. In this method, the charge and discharge pulses are injected into the battery at various SOCs and the battery parameters are extracted from their voltage responses. In this study, a lithium-ion battery (NCR18650) with a nominal capacity of 2.9Ah is used. It has a maximum charge voltage of 4.2V and a discharge voltage of 2.5V. The battery is first fully charged by the constant current and constant voltage (i.e. CC-CV) method till the battery charging current drops below 50mA. It is rested for 30 minutes to reach the steady state. The battery is then discharged at every 10% SOC interval with 30 minute rest interval as shown in Fig. 3.2. The low discharge current of 0.58A (0.2C) is used to avoid excessive internal heat and improve the discharging efficiency.

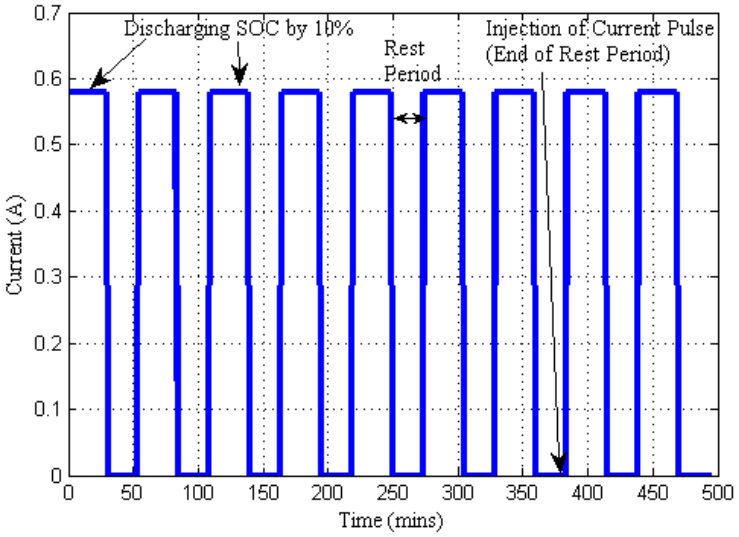

Fig. 3.2 Battery discharging profile for parameters identification

At the end of each rest period, discharge current pulses of different capacity rate of 0.58A (0.2C), 1.45A (0.5C), 2.175A (0.75C) and 2.9A (1C) and charge current pulses of 0.29A (0.1C), 0.58A (0.2C), 1.16A (0.4C) and 1.45A (0.5C) are applied for 5 seconds and their voltage responses are recorded. As the current pulses are injected at 10% SOC every interval, a total of 10 measurements are performed. Fig. 3.3 shows the discharge current pulse profile applied at the 60% SOC case and Fig. 3.4 shows their corresponding voltage responses.

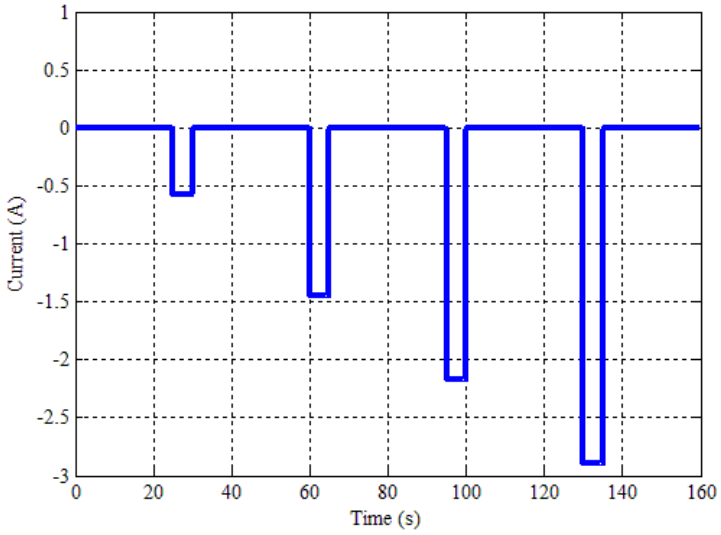

Fig. 3.3 Discharge current pulses applied at 60% SOC

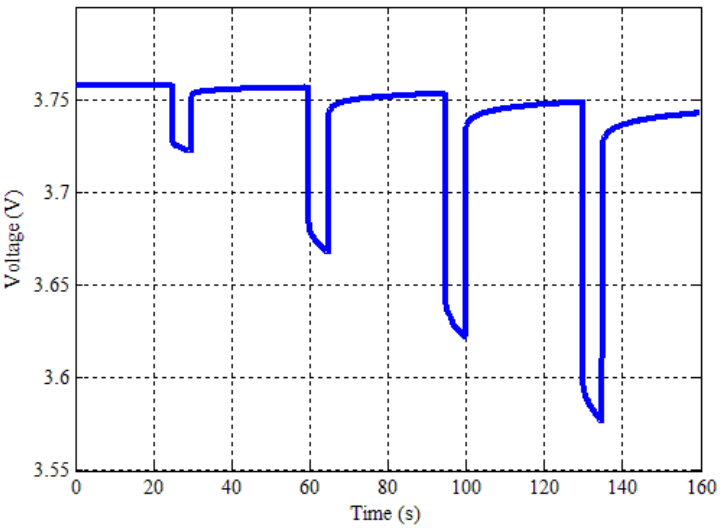

Fig. 3.4 Discharge current pulse voltage responses at 60% SOC

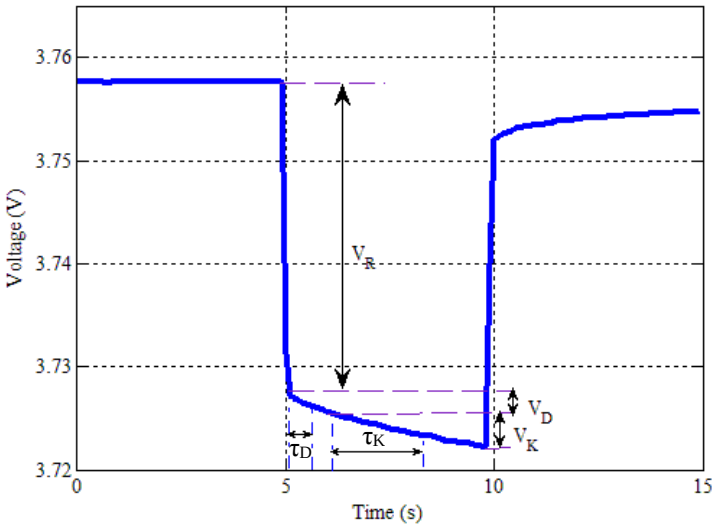

Fig. 3.5 Voltage response at 60% SOC by 0.58A (0.2C)

Fig. 3.5 shows the voltage response under the condition of 0.58A discharge pulse at 60% SOC. The battery voltage response can be divided into three parts to obtain the battery model parameters. The voltage drop V_R during the first period is caused by the ohmic resistance R_o ($V_R = I_B R_o$). For the short and long term transient periods, the voltage responses are expressed as

$$V_{Transient} = a \times e^{-\frac{t-t_o}{b}} \tag{3.4}$$

where $a = I_B \times R_D$, $b = \tau_D = (R_D \times C_D)$ in the short term transient and $a = I_B \times R_K$, $b = \tau_K = (R_K \times C_K)$ in the long term transient. Using Fig. 3.5, the battery parameters (R_o, R_D, R_K, C_D and C_K) can be calculated using (3.4) and the total battery internal resistance $R_{int} = R_o + R_D + R_K$ can then be obtained. The calculated charging and discharging resistance at different SOCs is plotted in Fig. 3.6. From the figure, it is observed that the battery internal resistance remains constant between 20% and 90% SOC range. However, there is a sharp increase in the fully charged/discharged state. These average resistances of

R_{int} will be used in the charge and discharge rate factor calculation in the following section.

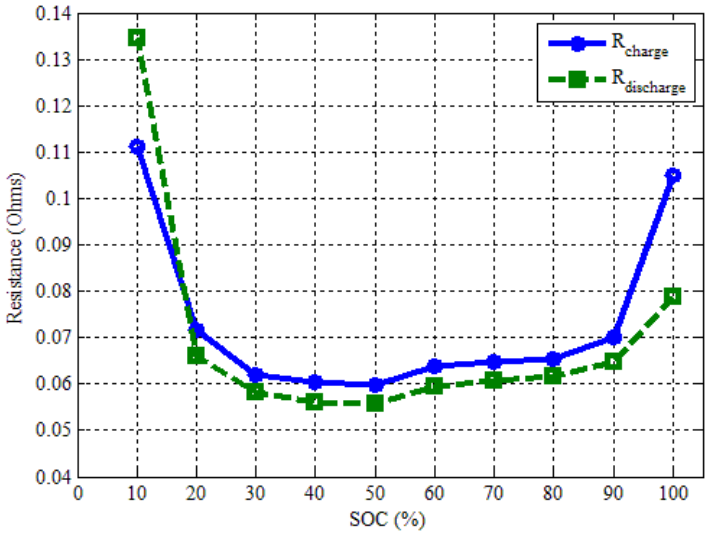

Fig. 3.6 Charge and discharge resistance versus SOC

3.2.2 Charge and discharge rate factor

The available charged and discharged battery capacity is dependent on temperature and current [162]. As the operating temperature of the satellite's battery is kept constant by a built-in heater, the temperature factor can be neglected. The dependency of charged/discharged capacity on the current rate is included through a rate factor. To determine the charge and discharge rate factor, the battery voltage under various discharge curves are measured and plotted in Fig. 3.7. First, one discharge curve is chosen as reference curve. The reference curve can be chosen arbitrarily but it is recommended to choose at the expected operating current range to improve the accuracy [162]. In our case, 1.375A is the expected operating range for discharge current and is chosen as the reference curve. From the discharge curves associated with different currents (0.55A, 2.0625A and 2.75A) and the reference discharge curve, the discharge rate factor α for any current I_B is calculated as follows:

$$\alpha = \frac{c}{d} \tag{3.5}$$

where c is the x-axis intersection point by shifting the reference curve I_{Ref} with $(I_{Ref} - I)$ and d is the x-axis intersection point of I_B.

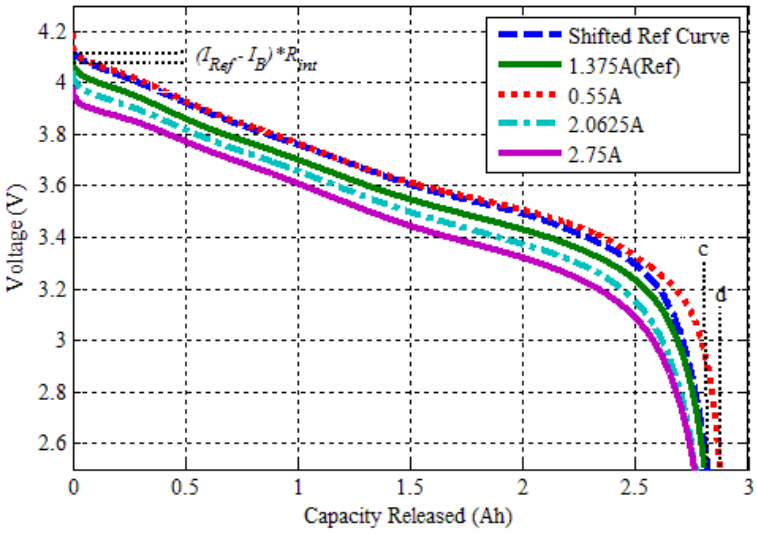

Fig. 3.7 Battery voltage curves under 0.55A, 1.375A, 2.0625A and 2.75A constant current discharge

The discharge rate factor for other discharge currents are calculated similarly and the results are plotted in Fig. 3.8. Similarly, the charge rate factor can be calculated with the same approach and is plotted in Fig. 3.10.

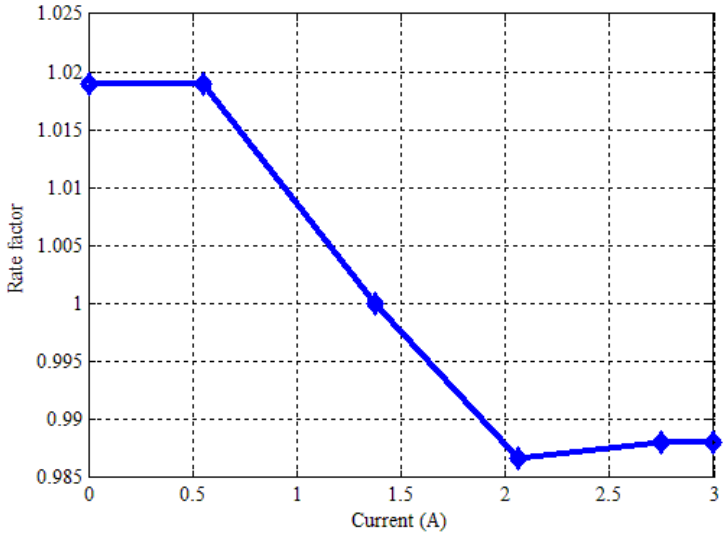

Fig. 3.8 Discharge rate factors with reference to 1.375A (I_{Ref})

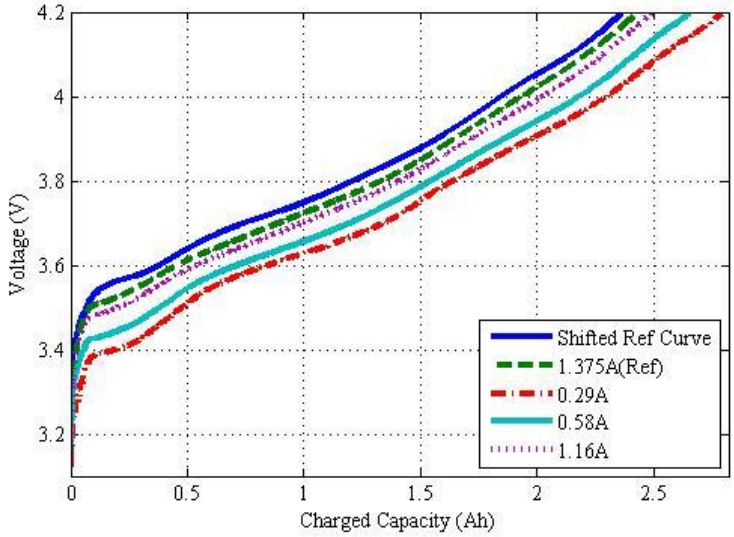

Fig. 3.9 Battery voltage curves under 0.29A, 0.58A, 1.16A and 1.375A constant current charge

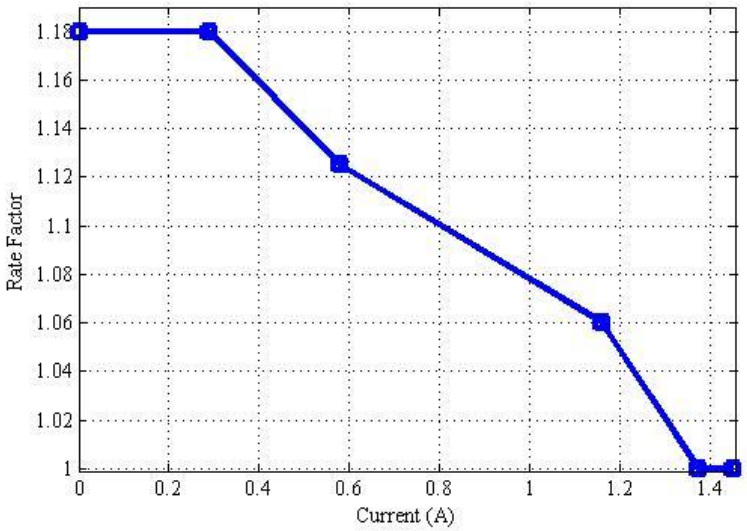

Fig. 3.10 Charge rate factors with reference to 1.375A (I_{Ref})

3.3 Opportunistic State-of-Charge Estimation

A new SOC estimation using ampere-hour counting with impulse response is introduced in this section. The conventional approach suffers from accumulated errors due to its reliance on integration and open loop nature. Using the opportunity arises from the turning on and off of satellite subsystems, the battery impulse response can be used to recalibrate the battery SOC at all levels of SOC instead of fully charged and

discharged states. Given the discharge and charge rate factor, the SOC can be estimated as

$$SOC_n = SOC_{n-1} - \int_{n-1}^{n} Rate\ Factor \times I_B \Delta t \tag{3.6}$$

In any linear time invariant (i.e. LTI) system, the output of LTI system to an arbitrary input can be obtained by using its impulse response as [163]

$$y[s] = u[s] * h[s] \tag{3.7}$$

where s is the Laplace operator, $y[s]$ is the battery output voltage, $u[s]$ is the battery current and $h[s]$ represents its impulse response in the frequency domain. In order to determine the impulse response of a battery, a narrow pulse of current is applied to the battery and the output voltage is measured. It is important to note that the pulse width should be sufficiently smaller than the shortest time constant of the system [138, 144]. In fact, knowing the smallest time constant of the system (i.e., battery) will allow us to select the pulse current such that a good approximation of the impulse response is achieved [138, 144]. Assuming a linear time invariant behaviour within the reasonable window of time, the impulse response of a battery can be used as a battery model. This model can then be used, along with the real time measurement of the current, to calculate the output voltage. Having the impulse response of the battery and convolving it with measured input current to the battery the output voltage can be calculated. The impulse response can be obtained by the turning on and off of the satellite subsystem. Battery impulse responses at 50%, 75% and 95% of SOC are plotted in Fig. 3.11.

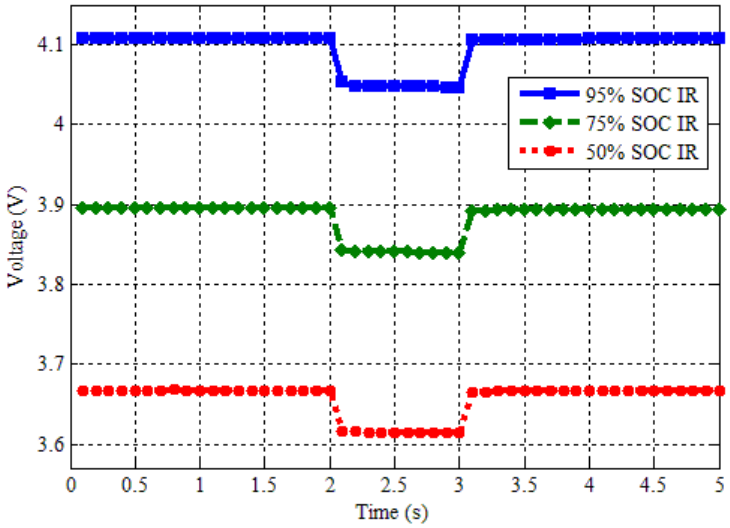

Fig. 3.11 Battery impulse response (IR) at 95%, 75% and 50% SOC

In general, the battery impulse response can be modelled by the ARMAX (autoregressive moving average) method [163]:

$$\begin{aligned} y(t)+a_1y(t-1)+....+a_{n_a}y(t-n_a)=u(t)+b_1u(t-1)+....+b_{n_b}u(t-n_b) \\ +e(t)+c_1e(t-1)+....+c_{n_c}e(t-n_c) \end{aligned} \tag{3.8}$$

where $y(t)$ represents the output voltage at time t, $u(t)$ represents the input current at time t, $e(t)$ is the white noise disturbance and n_a , n_b and n_c represent the polynomial orders. The $a_1 \cdots a_{n_a}$, $b_1 \cdots b_{n_b}$ and $c_1 \cdots c_{n_c}$ are the coefficients of the respective n_a, n_b and n_c polynomial orders. Using the battery impulse responses as shown in Fig. 3.11, the coefficients of impulse responses are calculated using the prediction-error method. With the polynomial coefficients and input current pulse, the battery output voltage can be estimated by (3.8). The estimated voltage response from 1.45A discharge current and 0.58A charge current with 10 seconds duration are plotted in Figs. 3.12 and 3.13.

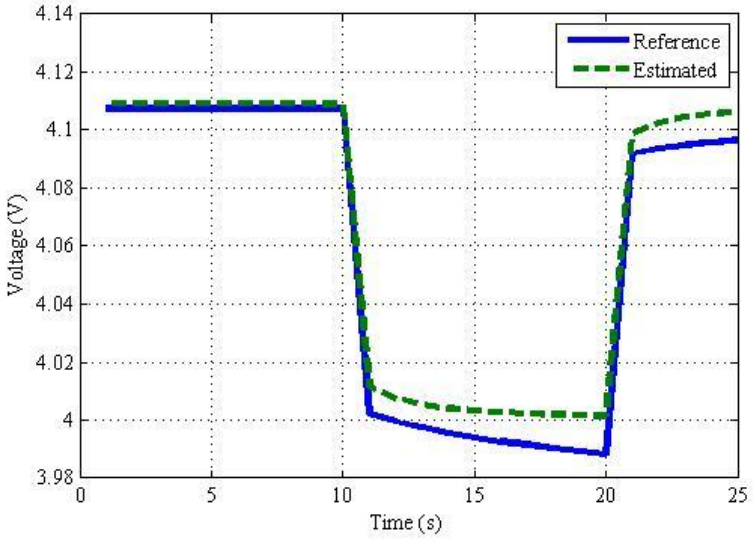

Fig. 3.12 Estimated voltage response from 1.45A discharge current

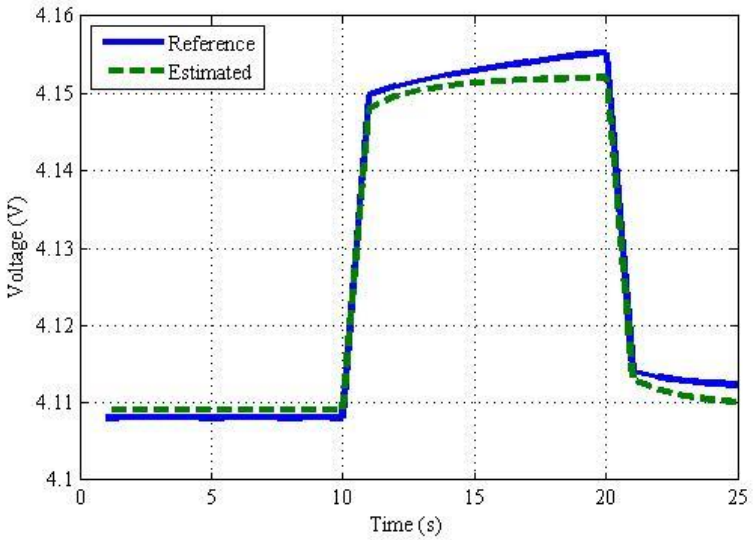

Fig. 3.13 Estimated voltage response from 0.58A charge current

3.4 Experimental Setup and Evaluation

For the experimental setup, a virtual instrument based test and measurement system similar to [161] is used. Fig. 3.14 shows the block diagram of the experimental setup. As shown in Fig. 3.14, it consists of a power supply (Agilent E3631A) to simulate the charging from solar power and a DC electronic load (Prodigit 3311F) to simulate the loading effects of satellite subsystems. A data acquisition system (NI USSB-6255) is

used to record the battery terminal voltage, terminal current and temperature for the reference SOC calculation. The reference SOC is obtained by using the calibrated ampere-hour counting via the high precision current sensor from the power supply and the DC electronics load with the sensor accuracy of 0.2% and 0.1% respectively. All the hardware equipment and components are controlled by the LABVIEW software. A microcontroller (100MHz C8051F120) is used to process the acquired data as well as the real-time experimental SOC for comparison. A thermal chamber (SE-300) is used to maintain the battery temperature at 25˚C to emulate the battery heater in maintaining the satellite battery temperature. The setup is used to perform a satellite mission scenario of a low earth orbit (LEO) profile. For the experiment, the satellite is operating at an altitude of 650km and one orbit lasts for 97 minutes. Fig. 3.15 shows the two 97 minutes LEO orbit scenario profile used in the experiment.

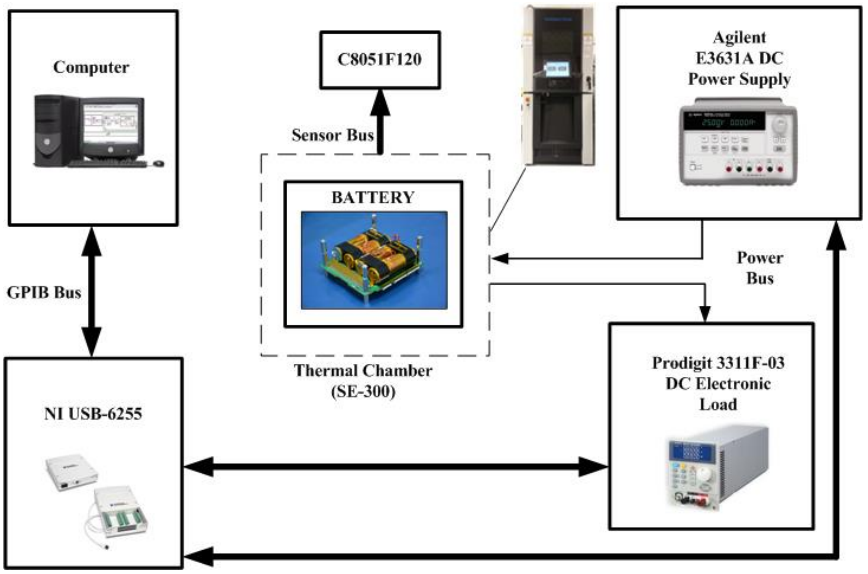

Fig. 3.14 Experimental setup block diagram

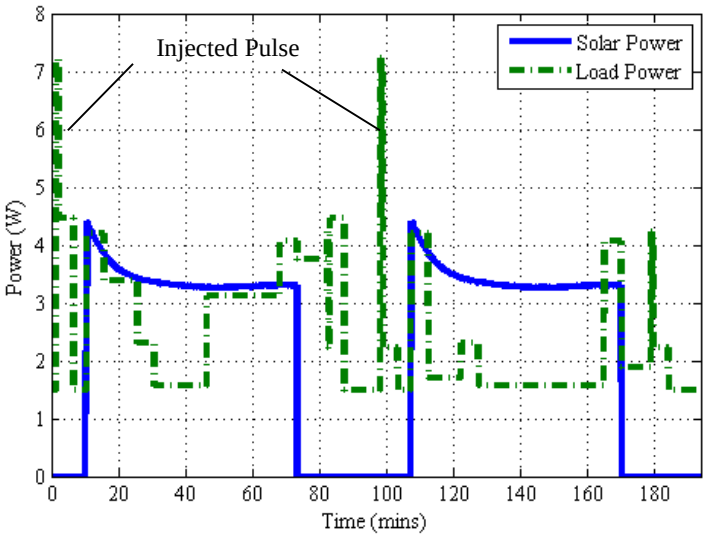

Fig. 3.15 LEO orbital scenario solar and load power profile

For the actual test, a total of 18 orbits are run in the experiment. In Fig. 3.15, the load spike represents the injected profile as described during the satellite operation scenario. At every injected pulse by means of turning on/off the satellite subsystems, the battery terminal voltages are estimated by different impulse response via discrete convolution and compared with battery voltage measurements using (3.7) and (3.8). Fig. 3.16 shows the measured battery voltage from the injected current pulse at various SOC levels. Comparison of the measurement and estimated voltage by different impulse response equations are plotted in Fig. 3.17.

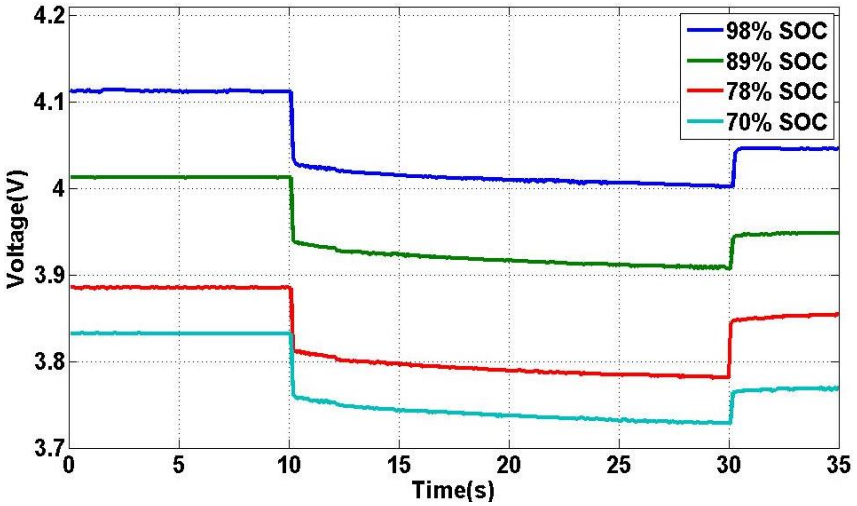

Fig. 3.16 Battery voltage measurements at various SOCs

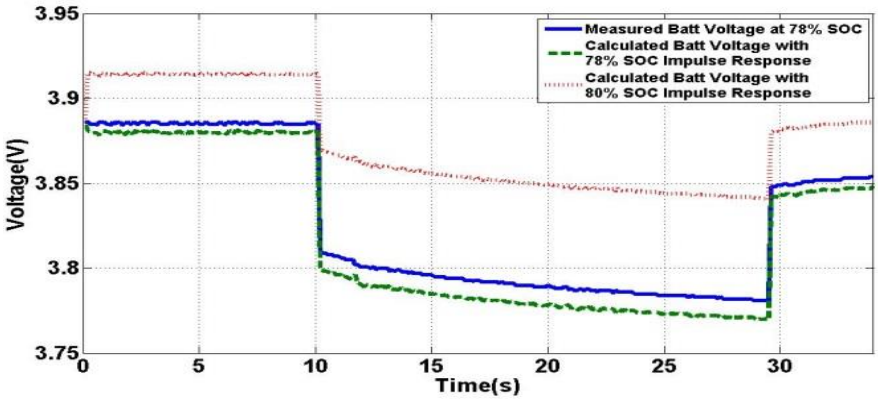

Fig. 3.17 Comparison of measured voltage at 78% SOC and calculated voltage using impulse response of 78% and 80% SOC

Each estimated voltage response at different SOCs is evaluated via the following cost function using the reference battery voltage measurement V_t and the estimated battery voltage $\hat{V}_t$

$$\text{Cost Function} = \min \sum_{i}^{m} \left(\left| V_{t,i} - \hat{V}_{t,i} \right| \right) \tag{3.9}$$

where m is the duration the satellite subsystem is turned on/off in seconds. The minimum cost represents the voltage estimation with the smallest estimation error. Each SOC level has the respective impulse response. Using the different impulse response, the voltage

estimation is performed and compared it with the measured battery voltage. The voltage response with minimal cost is then used to reset the ampere-hour method at the end of injected pulse. With this, the ampere-hour method is able to reset at every SOC level. The estimated SOC of the orbital test is plotted against reference SOC in Fig. 3.18. It can be observed that the estimated SOC closely follows the reference SOC. The corresponding error between the reference and estimated SOC of the orbital test is shown in Fig. 3.19. From the results, the proposed method has a maximum error of 5.14% and a mean error of 1.83%.

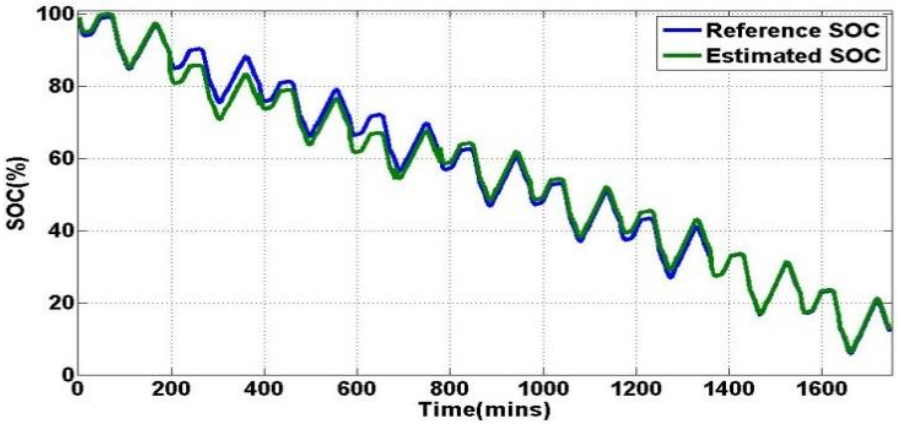

Fig. 3.18 Comparison between reference and estimated SOC

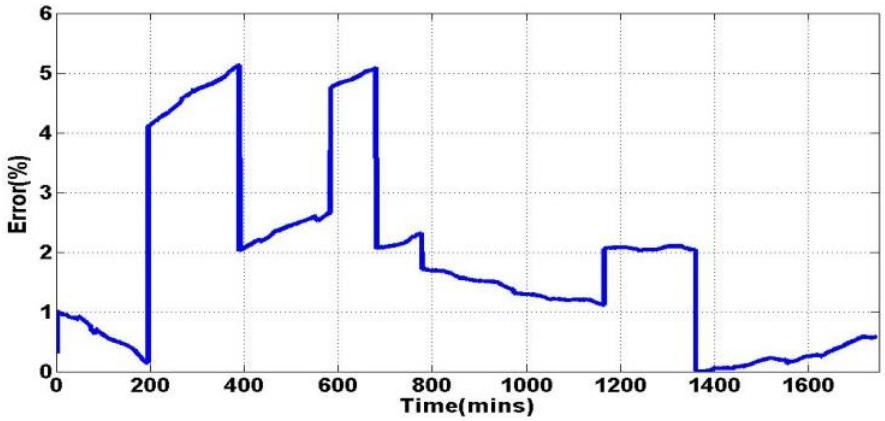

Fig. 3.19 Estimation error between reference and estimated SOC

3.5 Summary

In this chapter, the SOC estimation using ampere-hour counting with impulse response reset has been presented. The proposed method takes advantage of turning on/off of satellite subsystems instead of artificially injecting current pulses to extract battery's impulse response. The charging and discharging dependency on current have been considered and taken into account as charge and discharge rate factor in the method. The performance has been compared against that of the accurate ampere-hour meter using power supply and electronic load current. From the experiment, it is observed that the proposed approach has a maximum error of 5.14% and a mean error of 1.83%. For this approach, there is a need to store all the different SOC impulse responses in a look-up table. The impulse responses are different if the battery heater fails to maintain the operating temperature. To further improve the estimation, SOC estimation using the unscented Kalman filter with unit spherical transform is proposed in the next chapter.

CHAPTER 4

4. SQUARE ROOT SPHERICAL UNSCENTED KALMAN FILTER BASED STATE-OF-CHARGE ESTIMATION

4.1 Introduction

The opportunistic state-of-charge (SOC) estimation via impulse response presented in chapter 3 needs to store the impulse response in the look-up table. The impulse responses are different at different temperatures as well as between new and aged cells. In this chapter, a square root spherical unscented Kalman filter (Sqrt-UKFST) is proposed to overcome the major shortfalls of the extended Kalman filter (EKF) such as Jacobian matrix derivation and linearization accuracy as well as the opportunistic SOC estimation. The linearized approximation of the nonlinear function (or Jacobian matrix) in EKF increases the implementation complexity. In addition, its error convergence is sensitive to the initial state estimation error, and the inaccurate Jacobian matrix estimation could lead to filter divergence and affect its stability. The proposed method does not require the linearization for a nonlinear model and have a higher error-order (second order) than EKF (first order) [164]. In addition, it does not require refactorization on state covariance as in the regular unscented Kalman filter (UKF). The square root aspect of the filter improves the numerical stability by ensuring the state covariance is always semi-positive definite [94, 164]. The spherical transform requires fewer sigma points than the traditional unscented transform leading to lower computational cost [165, 166]. Furthermore, the spherical transform requires only one weighting parameter instead of three required by the regular UKF. To allow a better controllability of sigma point distribution, a unit hyper sphere model is used such that

the distribution is independent on the number of sigma points as in the standard spherical transform method.

The proposed method has been experimentally evaluated. The results will be compared with existing SOC estimation methods such as ampere-hour counting, portable fuel gauge and EKF.

4.2 Square Root Spherical Unscented Kalman Filter SOC Estimation

4.2.1 Battery state space equations

To construct a battery state space equations for Sqrt-UKFST, the double polarization model of a lithium-ion battery shown in Fig. 3.1 is used. Let ζ be the SOC, and V_D and V_K be the voltages across the two RC networks. Define the battery state variables x as $x = \begin{bmatrix} \zeta_{k+1} & V_{D_{k+1}} & V_{K_{k+1}} \end{bmatrix}^T$. The battery state process function, F, in discrete time using (3.1), (3.2) and (3.6) can be written as:

$$\zeta_{k+1} = \zeta_k - \frac{\eta I_B \Delta t}{Q_b} \tag{4.1}$$

$$V_{D_{k+1}} = V_{D_k} e^{\frac{-\Delta t}{R_D C_D}} + I_B R_D (1 - e^{\frac{-\Delta t}{R_D C_D}}) \tag{4.2}$$

$$V_{K_{k+1}} = V_{K_k} e^{\frac{-\Delta t}{R_K C_K}} + I_B R_K (1 - e^{\frac{-\Delta t}{R_K C_K}}) \tag{4.3}$$

$$\begin{bmatrix} \zeta_{k+1} \\ V_{D_{k+1}} \\ V_{K_{k+1}} \end{bmatrix} = F(V_{OC}(f(\zeta_k), V_{D_k}, V_{K_k})$$

$$= \begin{bmatrix} 1 & 0 & 0 \\ 0 & e^{\frac{-\Delta t}{R_D C_D}} & 0 \\ 0 & 0 & e^{\frac{-\Delta t}{R_K C_K}} \end{bmatrix} \begin{bmatrix} \zeta_k \\ V_{D_k} \\ V_{K_k} \end{bmatrix} + \begin{bmatrix} -\frac{\Delta t}{Q_b} \\ R_D(1-e^{\frac{-\Delta t}{R_D C_D}}) \\ R_K(1-e^{\frac{-\Delta t}{R_K C_K}}) \end{bmatrix} [I_B] \tag{4.4}$$

where V_t is the battery terminal voltage, I_B is the battery current, Q_b is the battery nominal capacity, Δt is the sampling time and η is the Coulomb efficiency. The Coulomb efficiency is assumed to be 1 based on the charge and discharge rate factor in Figs. 3.8 and 3.10. From Fig. 3.1, taking V_t as the system output and I_B as the system input, the V_t measurement function H can be obtained as

$$V_t = H(V_{OC}(f(\zeta)), V_D, V_K) = \begin{bmatrix} 1 & -1 & -1 \end{bmatrix} \begin{bmatrix} f(\zeta) \\ V_D \\ V_K \end{bmatrix} - I_B R_o \tag{4.5}$$

To estimate ζ, V_D and V_K, the battery parameters (R_o, R_D, R_K, C_D and C_K) and the function $f(\zeta)$ are required. These parameters will be experimentally identified in the next sections by using the open-circuit voltage test for $f(\zeta)$ and the transfer function method for the battery parameters.

4.2.2 Open-circuit voltage (V_{OC}) versus state-of-charge (SOC)

The open-circuit voltage of the battery V_{OC} has a nonlinear relationship with SOC. To obtain this nonlinear function, the open-circuit voltage test is conducted using the Panasonic NCR 18650 lithium-ion battery with 2.9Ah capacity as a case study. In this study, the hysteresis effect is neglected. The hysteresis effect can be included if an

additional voltage source is placed in parallel to V_{OC} in Fig. 3.1 at the expense of increased complexity [167-169]. The battery is first fully charged through the constant-current and constant voltage (CC-CV) method and is then rested for an hour to allow it to reach the steady state voltage before V_{OC} is measured. For the subsequent V_{OC} measured at different SOC levels, the battery is discharged at 0.29A for an hour, and rested for another hour to reach the steady state before another test is conducted. Fig. 4.1 shows the SOC-V_{OC} graph obtained from the experiment.

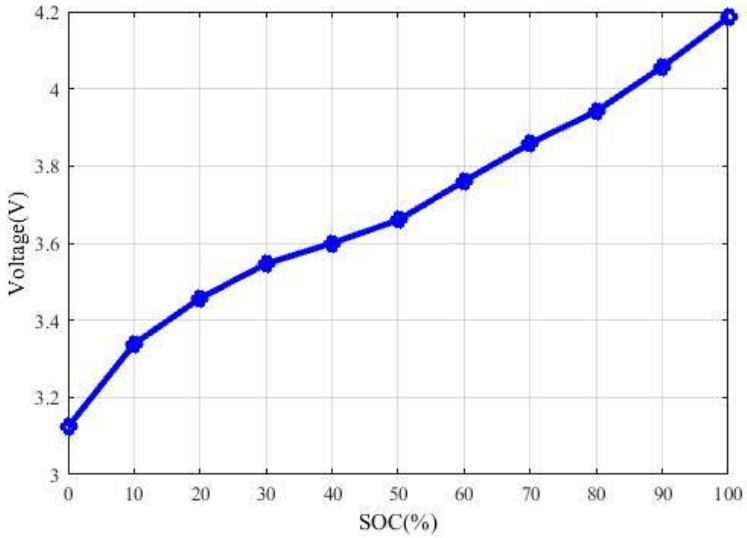

Fig. 4.1 V_{OC} versus SOC Graph

Table 4-1 Polynomial fit error of different polynomial order

Polynomial order	Polynomial Fit Error (RMSE)
4th Degree	0.0219
5th Degree	0.0199
6th Degree	0.0188
7th Degree	0.0036
8th Degree	0.0029

To describe the relationship between the V_{OC} and the SOC (ζ) in Fig. 4.1, a polynomial curve fitting is used. From Table 4-1, the 7th order polynomial equation has

the fitting error of 3.6mV. Although the higher polynomial order reduces the error, the improvement is insignificant. Hence, the 7th order polynomial equation has been used to express the V_{OC} versus SOC relationship:

$$V_{OC} = f(\zeta) = m_1\zeta^7 + m_2\zeta^6 + ... + m_6\zeta^2 + m_7\zeta + m_8 \tag{4.6}$$

Based on the experimental data in Fig. 4.1, the coefficients are obtained as: m_1 = *-20.553*, m_2 = *80.694*, m_3 = *-120.81*, m_4 = *83.352*, m_5 = *-22.502*, m_6 = *-1.542*, m_7 = *2.418* and m_8 = *3.124*. This V_{OC} and ζ relationship is used in the estimation of battery terminal voltage in the later section.

4.2.3 Battery parameters extraction

Battery parameters need to be identified to estimate the battery state variables. In this study, the transfer function method is used to identify the required battery parameters. Using (4.2)-(4.5), the V_t in the frequency domain after taking the Laplace transform can be written as

$$V_t(s) = V_{OC}(s) - I_B(s)R_o - \frac{R_D I_B(s)}{1+sR_DC_D} - \frac{R_K I_B(s)}{1+sR_KC_K} \tag{4.7}$$

By considering $V_t - V_{OC}$ as the output and the current I_B as the input, the transfer function $G(s)$ can be derived as

$$\begin{aligned} G(s) &= \frac{V_t(s)-V_{OC}(s)}{I_B(s)} = -\frac{a_2s^2+a_1s+a_o}{s^2+b_1s+b_o} \\ &= -\left\{ \frac{R_Os^2 + (\frac{R_O}{R_DC_D} + \frac{R_O}{R_KC_K} + \frac{1}{C_D} + \frac{1}{C_K})s + \frac{R_O+R_D+R_K}{R_DC_DR_KC_K}}{s^2 + (\frac{1}{R_DC_D} + \frac{1}{R_KC_K})s + \frac{1}{R_DC_DR_KC_K}} \right\} \end{aligned} \tag{4.8}$$

To extract the battery parameters via the transfer function, various charge and discharge pulses are injected into the battery at different SOC intervals and the corresponding voltage responses are measured. To obtain the required voltage

responses, the battery is first fully charged through the CC-CV method and is then discharged using the load profile of Fig. 3.2 in section 3.2. The profile is repeated as Fig. 4.2. At the end of each rest interval, different charge (0.29A, 0.58A, 1.16A, 1.45A) and discharge (0.58A, 1.45A, 2.175A, 2.9A) current pulses with 5s duration are injected into the battery, as shown in Fig. 4.3. Assuming V_{OC} remains unchanged over the short duration, the corresponding voltage responses with respect to each current pulse are recorded. The cycle is repeated at every 10% SOC interval until the battery is fully discharged. The voltage responses from the injected current pulses across different SOC values are then used in identifying the transfer function and the parameter identification. Fig. 4.4 shows one example of the voltage responses at 90% SOC.

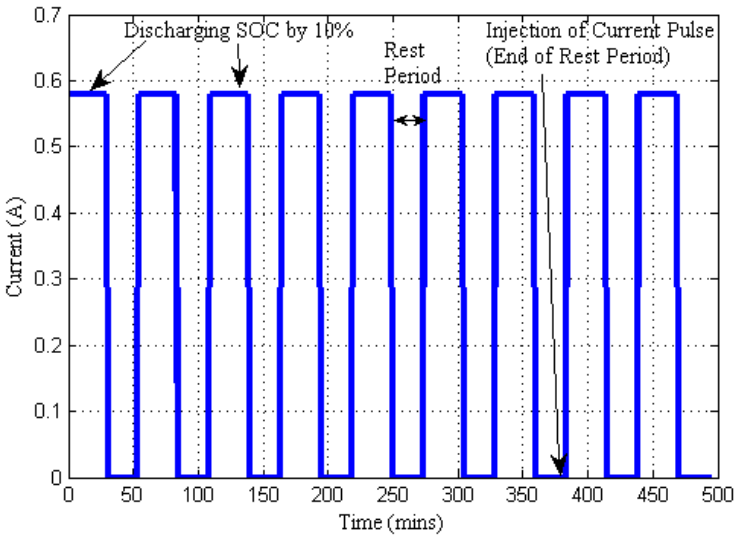

Fig. 4.2 Battery parameters extraction discharge current profile

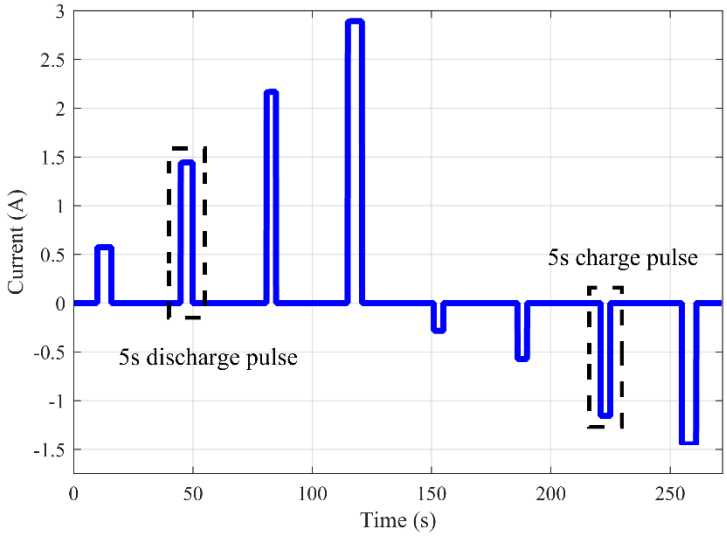

Fig. 4.3 Injected discharge and charge pulses at the end of each rest period

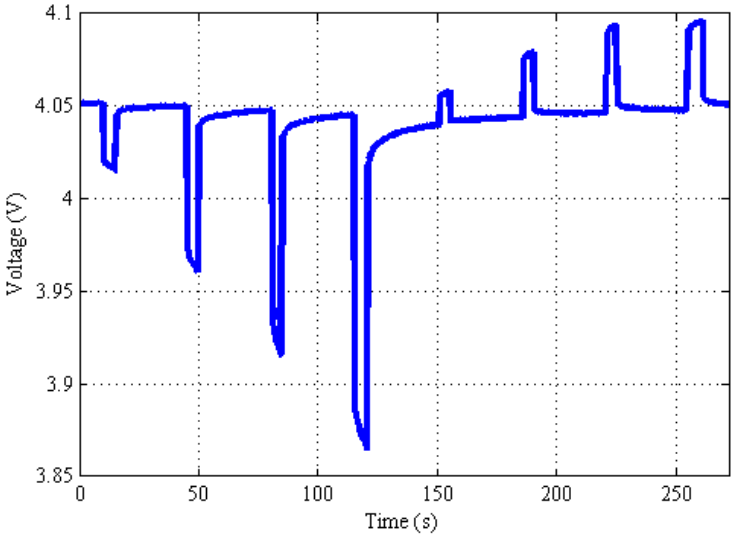

Fig. 4.4 Discharge and charge pulse voltage responses at 90% SOC

Using the voltage responses and the corresponding injected current pulses, the transfer function coefficients (a_2, a_1, a_0, b_1 and b_0) of $G(s)$ can be obtained using (4.8). The battery parameters (R_o, R_D, C_D, R_K and C_K) can then be obtained by solving these coefficients. Different sets of transfer functions and parameters are identified with respect to the measured voltage at each SOC level.

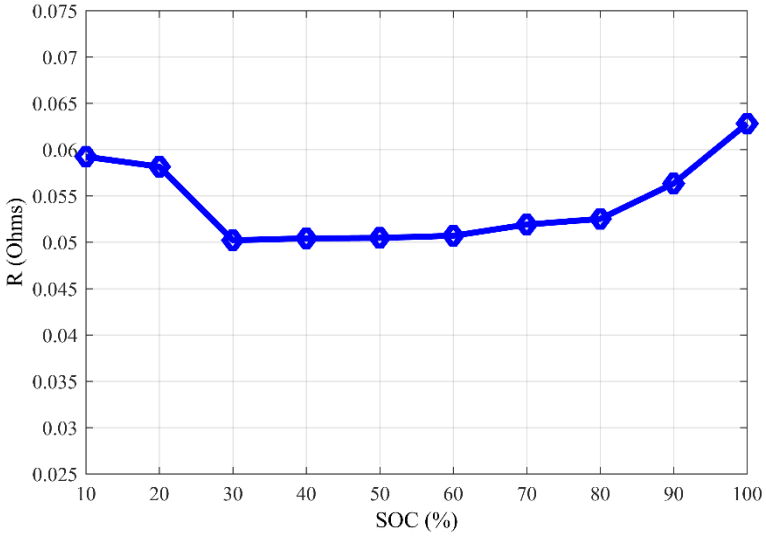

Fig. 4.5 R_o at different SOC

Fig. 4.5 presents the identified parameter R_o at different SOC levels. Although R_o changes with respect to the SOC level, the variation is negligible. This can be further seen in Fig. 3.6. In Fig. 3.6, the total resistance remains constant between 20% and 90% SOC range and increases only at the fully charged/discharged state. As the variations of parameters with respect to SOC are insignificant, the average identified parameters are used. Since the parameter identification is performed at 10% SOC interval, a total of 10 measurement are used to compute the average. Table 4-2 lists the minimum, average and maximum values of the identified battery parameters.

Table 4-2 Identified battery parameters at 25˚C

	Minimum	Average	Maximum
R_o	50.21 mΩ	54.28mΩ	62.82 mΩ
R_D	7 mΩ	10.58 mΩ	11 mΩ
R_K	27.5 mΩ	40.16 mΩ	56.6 mΩ
C_D	110F	330 F	690F
C_K	743F	1020 F	1520F

To verify the identified battery parameters, a hybrid pulse power characterization (HPPC) load profile as shown in Fig. 4.6 is used [88]. The comparison of experimental

and estimated voltages as well as the estimation error are shown in Figs. 4.7 and 4.8 respectively.

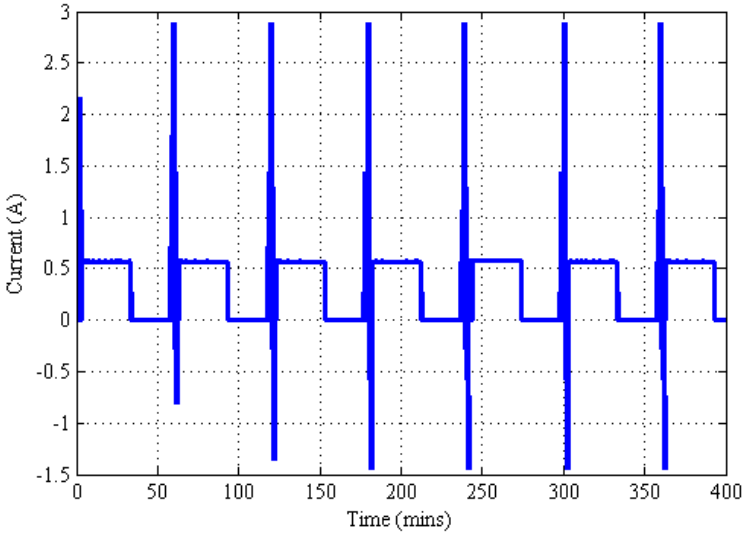

Fig. 4.6 Hybrid pulse power characterization (HPPC) load profile

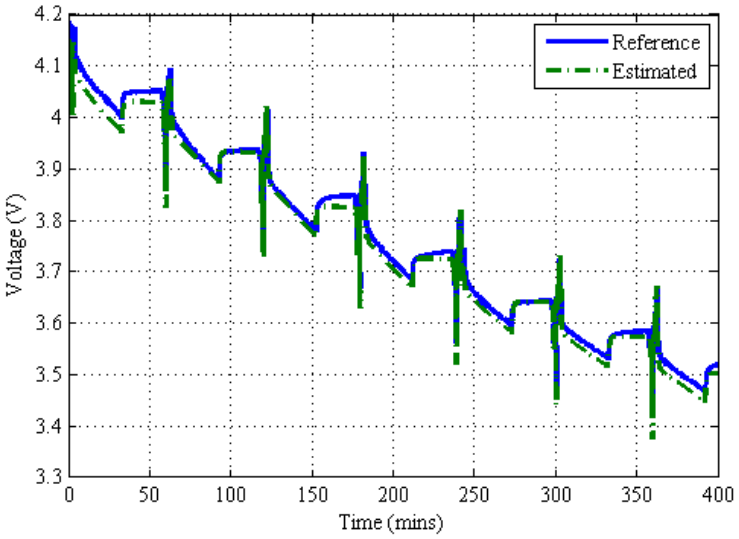

Fig. 4.7 Comparison of experimental and estimated voltages of discharge pulses

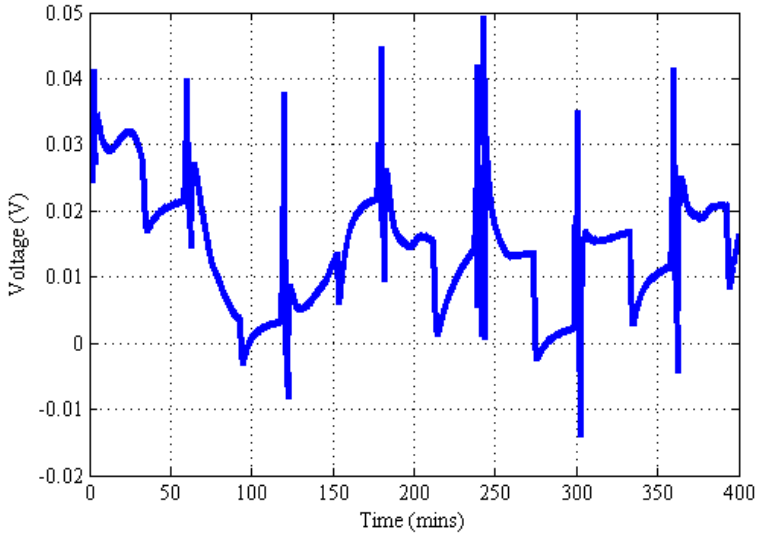

Fig. 4.8 Voltage estimation error of discharge pulses

From Fig. 4.8, the results show that the state space model of the battery using the identified battery parameters could accurately estimate the battery voltage. The mean estimation error is 10mV and the maximum error is 50 mV at the time that the charge and discharge pulses are applied.

4.2.4 Square root spherical unscented Kalman filter

1) Unit hyper sphere spherical unscented transform

The EKF has been extensively used in the SOC estimation in the literature [97, 170]. Although the EKF performs well by integrating with other estimation methods including observers and neural network, it experiences limitation such as the filter stability due to Jacobian matrices [171]. To achieve better stability and accuracy, the unscented Kalman filter (UKF) has been introduced as it does not require the computation of Jacobian matrices. The UKF uses a selection of weighted sigma points to estimate the sample mean and covariance.

There are several sigma point transformation methods: unscented, simplex and spherical transforms [172]. Due to the fact that the computation cost of UKF is

proportional to the number of sigma points, it is beneficial to have fewer sigma points. The unscented transform requires $2n + 1$ sigma points selection, where n is the dimension of the system. The simplex transform requires only $n + 1$ sigma points. However, it suffers from numerical stability issues due to the fact that the sigma points lie on the sphere with a radius of $2^{n/2}$ [173].

The spherical transform considered in this paper for SOC estimation requires $n + 2$ sigma points. Its numerical stability is improved by reducing the sphere radius to $\sqrt{n} \,/\, (1-W_0)$. In the spherical transform of a n-dimensional system, the initial weight W_0 is set first and the choice of W_0 affects only the fourth and higher order moments of the set of sigma points. Using W_0 and n, the rest of the weights (W_1 to W_n) are selected. The three element vectors (χ_0^1, χ_1^1 and χ_2^1) are generated using W_1. To generate the required $n + 2$ sets of sigma point vectors with n dimension, the element vectors are recursively expanded.

In this study, it was discovered that several stability issues remain in the spherical transform UKF, such as negative battery parameters. This is due to the fact that the sphere radius for sigma point distribution depends on the size of estimated state vector. To ensure the sphere radius is independent on the estimated state vector size, and ζ always fall within the range of the expected variance of $f(\zeta)$, all sigma points are normalized with respect to $\sqrt{n} \,/\, (1-W_0)$. Thus, all the sigma points are guaranteed to be projected within a unit hyper sphere. The spherical transform is summarized in Table 4-3.

Table 4-3 Proposed unit hyper sphere spherical unscented transform

Step 1: Choose the initial weight, W_0

$$0 \le W_0 \le 1$$

Step 2: Compute the rest of the weights, W_i

$$W_i = \frac{1 - W_0}{n+1}$$

Step 3: Initialize the following element vectors,

$$\chi_0^1 = [0],\ \chi_1^1 = \begin{bmatrix} -\frac{1}{\sqrt{2W_1}} \end{bmatrix},\ \chi_2^1 = \begin{bmatrix} \frac{1}{\sqrt{2W_1}} \end{bmatrix}$$

Step 4: Recursively expand the following vectors, for j=2,…,n,

$$\chi_i^j = \begin{cases} \begin{bmatrix} \chi_0^{j-1} \\ 0 \end{bmatrix} & \text{for i = 0} \\ \begin{bmatrix} \chi_i^{j-1} \\ -\frac{1}{\sqrt{j(j+1)W_1}} \end{bmatrix} & \text{for i =1,....., j} \\ \begin{bmatrix} 0_{j-1} \\ \frac{j}{\sqrt{j(j+1)W_1}} \end{bmatrix} & \text{for i = j+1} \end{cases}$$

Step 5: Arrange χ_i^j vectors in a unit hyper sphere

$$\frac{\chi_i^j}{\sqrt{n}/(1-W_0)}$$

2) Square root unscented Kalman filter (Sqrt-UKFST)

In a standard UKF, the state covariance P_k is recursively updated and propagated by decomposing into matrix square root, S_k, for sigma point mapping at each time step where $P_k = S_k S_k^T$. Then, P_k matrix is reconstructed from all the propagated sigma points for updating purpose. On the other hand, the Sqrt-UKFST directly propagates and updates the S_k without the needs of decomposing and reconstructing matrix P_k. This avoids the needs of refactorization on P_k at each time step. Thus positive semi-definiteness of the P_k could be guaranteed [164]. The square root UKF makes use of three linear algebra techniques for the square root covariance update and propagation.

They are *QR* decomposition (*qr*), Cholesky factor updating (*cholupdate*) and efficient least squares [164].

Given the state space model of the nonlinear battery system in (4.4) and the output equations in (4.5), it can be expressed in the general form as

$$x_{k+1} = f(x_k, u_k) + Q_k \tag{4.9}$$

$$y_k = h(x_k, u_k) + R_k \tag{4.10}$$

where the system input variable u_k is I_B, x_k is the system state variable of $\begin{bmatrix} \zeta & V_D & V_K \end{bmatrix}$ and y_k is the measured output V_t. Let $Q_k \sim N(0, cov_Q)$ and $R_k \sim N(0, cov_R)$ represent the uncorrelated zero-mean white Gaussian process and measurement noise. The proposed Sqrt-UKFST is as follows.

1) *Initialization*:

The initial state $\hat{x}_0 = \begin{bmatrix} \zeta & V_D & V_K \end{bmatrix}^T$ and initial covariance S_0 are initialized using (4.11) and (4.12)

$$\hat{x}_0 = E\begin{bmatrix} x_0 \end{bmatrix} \tag{4.11}$$

$$S_0 = chol\left\{ E[(x_0 - \hat{x}_0)(x_0 - \hat{x}_0)^T] \right\} \tag{4.12}$$

where *chol* represents the Cholesky factor calculation.

2) *Computation of sigma points*:

Through the proposed unit hyper sphere unscented transform in Table 4-3, the *n* state variables can be transformed into *n + 2* sigma points χ_i^n with the corresponding weight W_i with *i* ranges from 0 to *n + 1*. Using the state *x* and covariance *S* at *k-1*, the sigma points $\chi_{i,k-1}$ are computed using (4.13)

$$\chi_{i,k-1} = \hat{x}_{k-1} + S_{k-1}\chi_i^n \tag{4.13}$$

3) *Time update:*

The sigma points are propagated through the state function $f(x_k,u_k)$ in (4.4) and a *priori* state estimate $\hat{x}_k^-$ is calculated using the propagated sigma points $\chi_{k|k-1}$,

$$\chi_{k|k-1} = F(\chi_{k-1}, I_{B,k-1}) \tag{4.14}$$

$$\hat{x}_k^- = \begin{bmatrix} \hat{\zeta}_k^- & \hat{V}_D^- & \hat{V}_K^- \end{bmatrix}^T = \sum_{i=0}^{n+1} W_i \chi_{k|k-1} \tag{4.15}$$

A *priori* error covariance S_k^- is computed using (4.16) and (4.17),

$$S_k^- = qr\left\{\begin{bmatrix} \sqrt{W_i}(\chi_{1:n+1,k|k-1} - \hat{x}_k^-) & \sqrt{Q} \end{bmatrix}\right\} \tag{4.16}$$

$$S_k^- = cholupdate\{S_k^-, \chi_{0,k|k-1} - \hat{x}_k^-, W_0\} \tag{4.17}$$

where *qr* and *cholupdate* represent the QR factorization and Cholesky factor update. These propagated sigma points $\chi_{k|k-1}$ are then used to calculate $\Upsilon_{k|k-1}$ through the nonlinear measurement model $H(x_k,u_k)$ in (4.5) and estimate the system output $\hat{y}_k^-$ using (4.18) and (4.19) as follows

$$\Upsilon_{k|k-1} = H[\chi_{k|k-1}, I_{B,k-1}] \tag{4.18}$$

$$\hat{y}_k^- = \hat{V}_t^- = \sum_{i=0}^{n+1} W_i \Upsilon_{i,k|k-1} \tag{4.19}$$

4) *Measurement update and correction*:

The measurement covariance $S_{\tilde{y}_k}$ and the cross covariance matrix $P_{x_k y_k}$ are then computed based on the estimated Υ_k, $\hat{y}_k^-$ and the transformed sigma points $\chi_{k|k-1}$ using (4.20)-(4.22) as

$$S_{\tilde{y}_k} = qr\{[\sqrt{W_i}(\Upsilon_{1:n+1,k|k-1} - \hat{y}_k^-) \quad \sqrt{R}]\} \tag{4.20}$$

$$S_{\tilde{y}_k} = cholupdate\{S_{\tilde{y}_k}, \Upsilon_{0,k|k-1} - \hat{y}_k^-, W_0\} \tag{4.21}$$

$$P_{x_k y_k} = \sum_{i=0}^{n+1} W_i(\chi_{i,k|k-1} - \hat{x}_k^-)(\Upsilon_{i,k|k-1} - \hat{y}_k^-)^T \tag{4.22}$$

The Kalman gain K_k is calculated using (4.23) as

$$K_k = P_{x_k y_k} S_{\tilde{y}_k}^{T^{-1}} S_{\tilde{y}_k}^{-1} \tag{4.23}$$

The state estimate update $\hat{x}_k^+$ is computed through measurement ($y_k = V_t$) and the calculated K_k using (4.24) as

$$\hat{x}_k^+ = \hat{x}_k^- + K_k(y_k - \hat{y}_k^-) \tag{4.24}$$

Lastly, a *posterior* error covariance S_k is computed as

$$S_k = cholupdate\{S_k^-, K_k S_{\tilde{y}_k}, -1\} \tag{4.25}$$

These steps are repeated till the end of the experiment. Fig. 4.9 shows the flowchart of the Sqrt-UKFST algorithm.

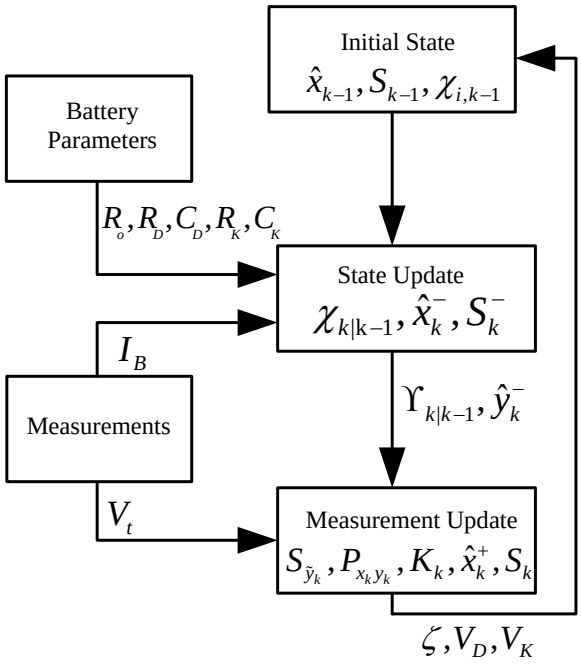

Fig. 4.9 Flowchart of Sqrt-UKFST

4.3 Simulation and Experimental Evaluation of Sqrt-UKFST

4.3.1 Simulation studies of Sqrt-UKFST

To verify the performance of the Sqrt-UKFST, a simulation study is first performed using the lithium-ion battery model in Simulink. Fig. 4.10 shows the constructed simulation testbed used in Simulink. The Sqrt-UKFST algorithm is performed using the input data of V_t and I_B from the Simulink instead of using the actual experimental measurements.

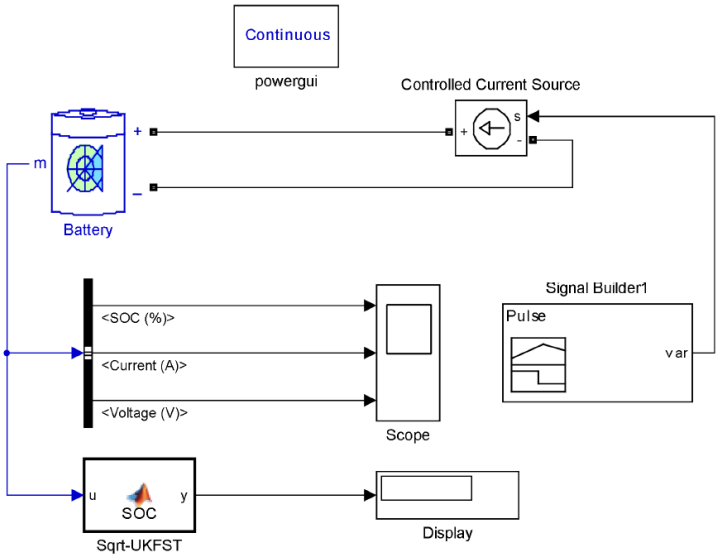

Fig. 4.10 Sqrt-UKFST simulation testbed in Simulink

The lithium-ion battery in the simulation has a nominal voltage of 3.6V and a nominal capacity of 2.9Ah as well. The following assumptions have been made to get the battery model in Simulink [174]:

- The internal resistance is kept constant during the charge and discharge cycles and does not vary with the amplitude of the current
- The battery capacity is the same for different current magnitudes
- Thermal effect is ignored.

Fig. 4.11 shows the current profile of the simulation to verify the Sqrt-UKFST. It consists of 5 different pulse charge and discharge currents, i.e. 2.9A discharge, 1.45A charge, 1.45A discharge, 0.58A charge and 0.58A discharge. Each charge and discharge pulse have 30 seconds of rest time between them. The comparison between the estimated and the reference SOC is plotted in Fig. 4.12 and its absolute estimation error is shown in Fig. 4.13. Fig. 4.13 shows that the Sqrt-UKFST estimates the SOC accurately with a maximum error bound of 1%.

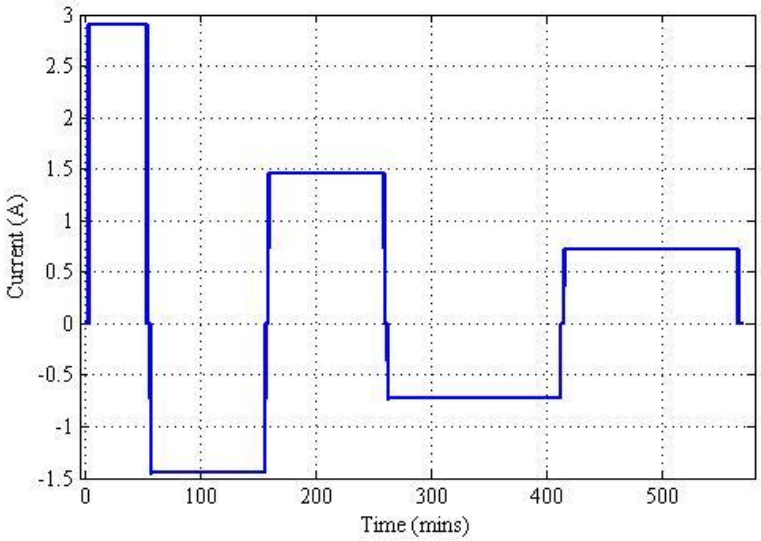

Fig. 4.11 Charge and discharge profile of simulation

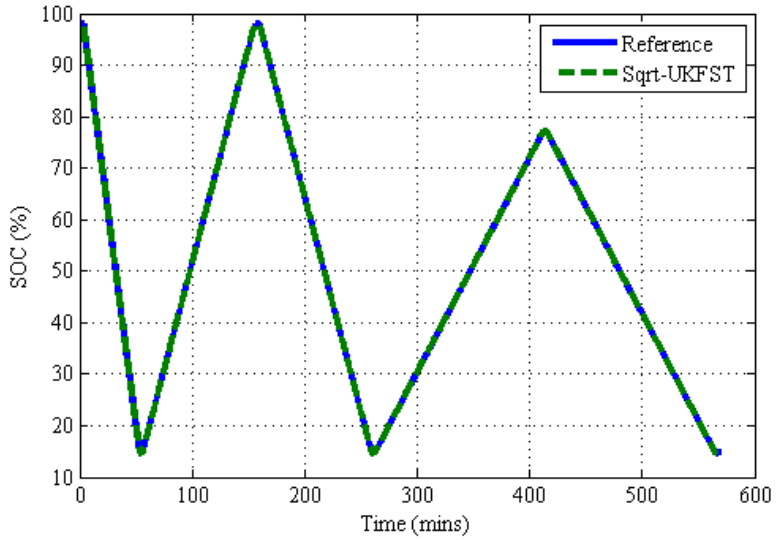

Fig. 4.12 SOC estimation comparison in simulation

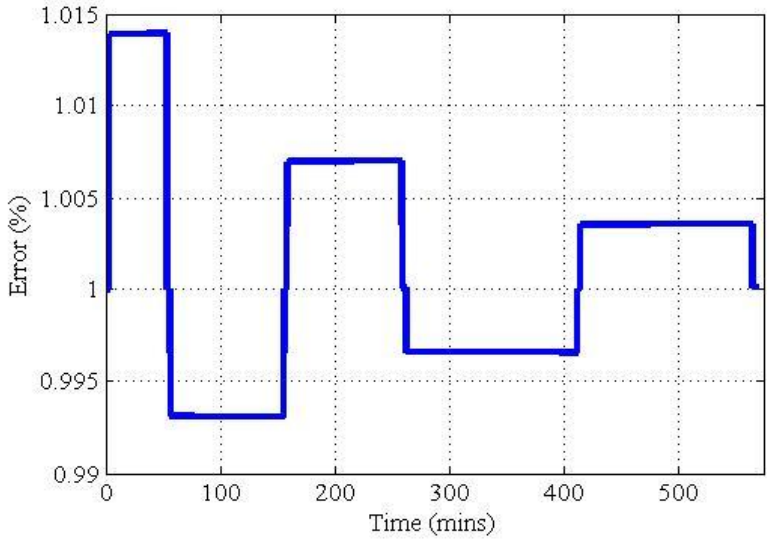

Fig. 4.13 Absolute SOC estimation error in simulation

To evaluate the performance of SOC estimation quantitatively, the absolute mean, root mean square (RMSE) and absolute maximum errors of the SOC are calculated as follows

$$Mean = \frac{1}{m}\sum_{k=1}^{m}\left|\zeta_k - \hat{\zeta}_k\right| \tag{4.26}$$

$$RMSE = \sqrt{\frac{1}{m}\sum_{k=1}^{m}\left(\zeta_k - \hat{\zeta}_k\right)^2} \tag{4.27}$$

$$Maximum = Max\left|\zeta_k - \hat{\zeta}_k\right| \tag{4.28}$$

where ζ_k is the reference SOC and $\hat{\zeta}_k$ is the estimated SOC. Table 4-4 summarizes the calculated error performance from the simulation study.

Table 4-4 SOC estimation error performance in simulation

Mean	1.00%
RMSE	1.00%
Maximum	1.02%

4.3.2 Experimental studies of Sqrt-UKFST

To validate the proposed method experimentally, the same battery test bench as shown in Fig. 3.14 and the satellite mission scenario of Fig. 3.15 are used. Similarly, the reference SOC is obtained by using the calibrated ampere-hour counting via the high precision current sensor from the power supply and the DC electronics load. For performance comparison, the EKF, a portable fuel gauge (MAX17058) with an expected accuracy of 3~5% and the ampere-hour counting method are used for benchmarking.

1) SOC estimation with unknown initial state

The performance of SOC estimation using the proposed Sqrt-UKFST with unknown initial SOC is performed. The true SOC is set as 100% and the two initial SOC are set at 0% and 50%. Fig. 4.14 shows that the estimated SOC converges to the true SOC within 250s when the initial SOC error is 50%. With the initial SOC error at 100%, the proposed method converges to the true SOC after 300s. To further validate the convergence performance of the proposed method, different reference SOC states are used. Fig. 4.15 summarizes the SOC estimation errors after 300s of different initial estimated SOC for four reference SOC values. The four reference SOC values are 30%, 50%, 75% and 100%. From Fig. 4.15, the Sqrt-UKFST is able to converge to the reference SOC across the entire operating range with a maximum estimation error of 2.4%. The results show that the initial estimation error does not impact the convergence of the SOC estimation using the proposed Sqrt-UKFST.

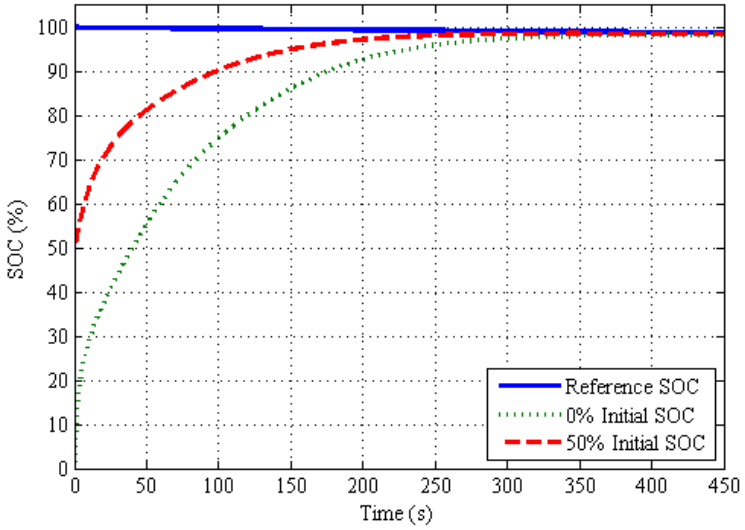

Fig. 4.14 SOC estimation with unknown initial state

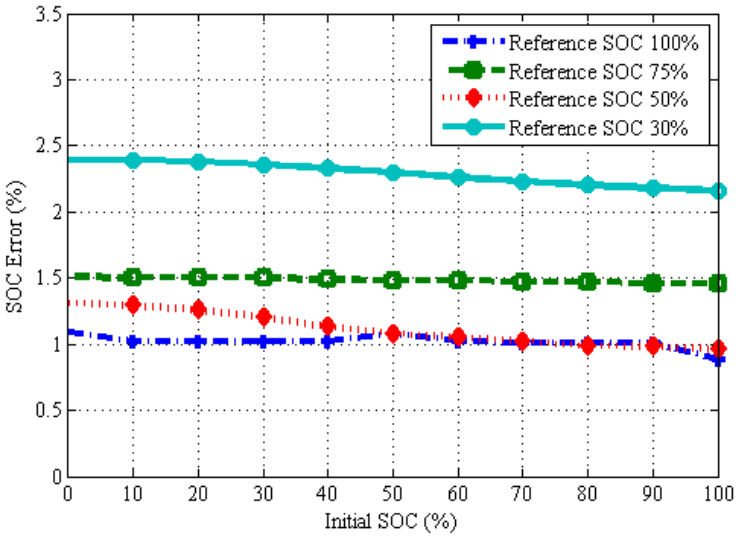

Fig. 4.15 SOC estimation error under unknown initial SOC

2) SOC estimation with known initial state

The initial state of SOC is known whenever the battery is fully charged. Fig. 4.16 shows the experimental results of the battery current with 16 satellite orbits using the load profile in Fig. 3.15. In this experiment, the battery is fully charged before the test is commenced.

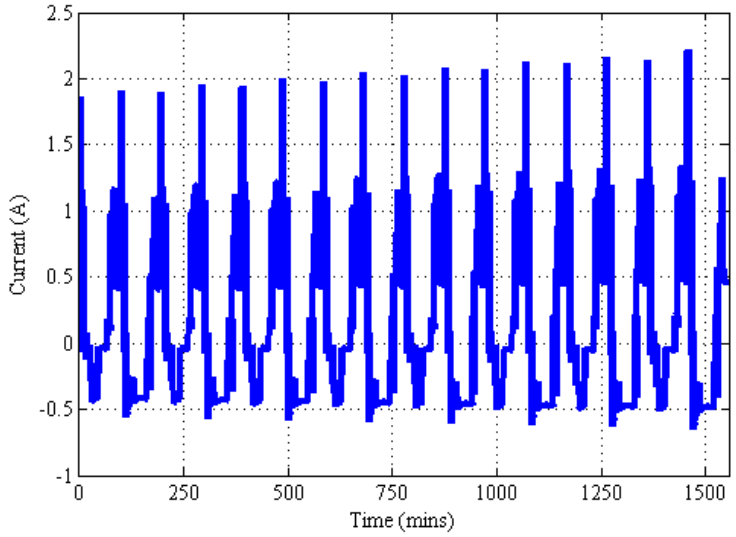

Fig. 4.16 Battery current profile under orbital test experiment

Fig. 4.17 shows the corresponding SOC estimation using various approaches. From the results, it is observed that the SOC based on the ampere-hour counting method drifted away from the reference SOC due to the accumulated errors. Moreover, it is noticed that both the EKF and Sqrt-UKFST perform better than the fuel gauge.

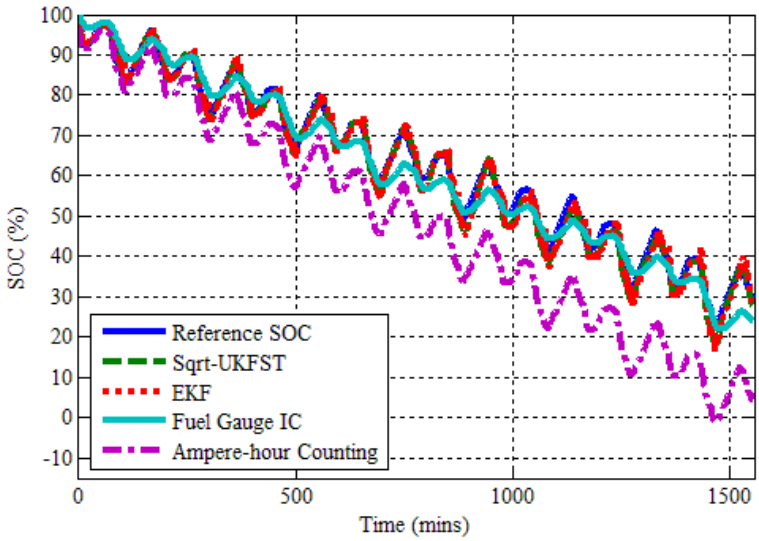

Fig. 4.17 Comparison of SOC estimation

The percentage SOC estimation error is plotted in Fig. 4.18. From the results, it is observed that the ampere-hour counting error increases linearly due to the accumulated errors. For the fuel gauge circuit, its SOC estimation relies solely on the voltage

readings. Since the battery voltage increases when it is being charged and vice versa, the fuel gauge circuit experiences higher fluctuations in SOC estimation than EKF and Sqrt-UKFST whenever a charge/discharge current is applied. Both EKF and Sqrt-UKFST have similar SOC estimation error.

Table 4-5 summarizes the results. It shows that the Sqrt-UKFST has the lowest RMSE of 1.42%, absolute mean error of 1.09% and maximum error of 4.96%. For the EKF, its errors are about 40% higher than Sqrt-UKFST. Furthermore, the fuel gauge estimation error is at least 100% higher than the Sqrt-UKFST. It is noted that the ampere-hour counting mean error is almost ten times higher than the Sqrt-UKFST.

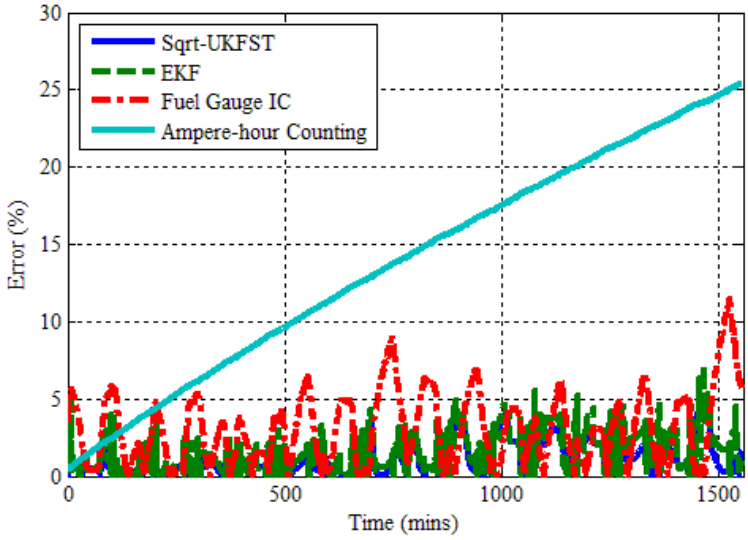

Fig. 4.18 Comparison of SOC estimation error

Table 4-5 Performance comparison

		Sqrt-UKFST	*EKF*	*Fuel Gauge*	*Ampere-hour Counting*
RMSE	Absolute Value	1.42%	1.95%	3.85%	15.48%
	% increase w.r.t Sqrt UKFST	-	37.32%	171.13%	990%
Mean Error	Absolute value	1.09%	1.54%	3.09%	13.73%
	% increase w.r.t Sqrt-UKFST	-	41..28%	183%	1153%
Maximum Error	Absolute value	4.96%	7.15%	11.47%	25.38%
	% increase w.r.t Sqrt-UKFST	-	44.15%	131.30%	411.69%

3) Computational requirements

Table 4-6 compares the number of multiplication required in each operation for the spherical unscented transform, regular unscented transform and EKF. In the table, "*n*" denotes the number of states and "*L*" is the number of measurements. From the table, it is observed that the spherical unscented transform requires less multiplication than the regular unscented transform as a result of using fewer sigma points. For the SOC estimation ($n = 3$ and $L = 1$), the total number of multiplication is 81 for the spherical unscented transform and 107 for the unscented transform. Thus there is a 32% saving in multiplication using the Sqrt-UKFST.

Table 4-6 Multiplication required for each operation

	Multiplication Required		
Operation	*Spherical Unscented Transform*	*Unscented transform*	*EKF*
P_{xx}	$(n + 2)\, n^2$	$(2n + 1)\, n^2$	-
P_{xy}	$(n + 2)\, (nL)$	$(2n + 1)\, (nL)$	-
P_{yy}	$(n + 2)\, L^2$	$(2n + 1)\, L^2$	-
$PH^T(HPH^T + R)$	-	-	$L^3 + 2nL^2 + 2n^2L$
$K(y - \hat{y})$	$L^3 + nL^2 + nL$	$L^3 + nL^2 + nL$	$nL + Ln^2$
$P - KP_{yy}K$	Ln^2	Ln^2	$n^2L + n^3$
Total Multiplication Required ($n = 3, L = 1$)	81	107	73

4) Robustness study in terms of battery's parameters variation

The accuracy of SOC estimation is affected by the battery model accuracy. The battery parameters may vary depending on the battery's state-of-health [175]. As the battery usage increases, its parameters such as R_o would change. The variation could be as high as 60% of initial parameters [176]. To study the robustness of the proposed approach and EKF with respect to parameters variation, different battery parameter sets are used. Table 4-7 presents different sets of parameters in terms of 25%, 50%, 75%, 125%, 150%, 175% and 200% of the actual battery parameters. For groups 1 to 3, the true battery parameters are higher than the estimated parameters, and groups 4 to 7 provide the cases that the true parameters are lower than the estimated parameters.

Table 4-7 Different parameters sets used in sensitivity analysis

	R_o (mΩ)	R_D (mΩ)	R_K (mΩ)	C_D (F)	C_K (F)
True Parameters (p)	54.28	10.58	40.16	330	1020
Group 1 (0.25p)	13.57	2.65	10.04	82.5	255
Group 2 (0.5p)	27.14	5.29	20.08	165	510
Group 3 (0.75p)	40.71	7.94	30.12	247.5	765
Group 4 (1.25p)	67.85	13.23	50.2	412.5	1275
Group 5 (1.5p)	81.42	15.87	60.24	495	1530
Group 6 (1.75p)	94.99	18.52	70.28	577.5	1785
Group 7 (2p)	108.56	21.06	80.32	660	2040

The parameters in each group are used by Sqrt-UKFST and EKF to estimate the SOC. Figs. 4.19 and 4.20 show the RMSE and absolute maximum error. Both figures show that Sqrt-UKFST has lower error than EKF. Fig. 4.19 shows that the highest RMSE error for EKF and Sqrt-UKFST are 7.6% and 4.3% respectively. The absolute maximum error for EKF can be as high as 29% while Sqrt-UKFST remains below 8%. In summary, the Sqrt-UKFST is more robust to parameter variation than EKF.

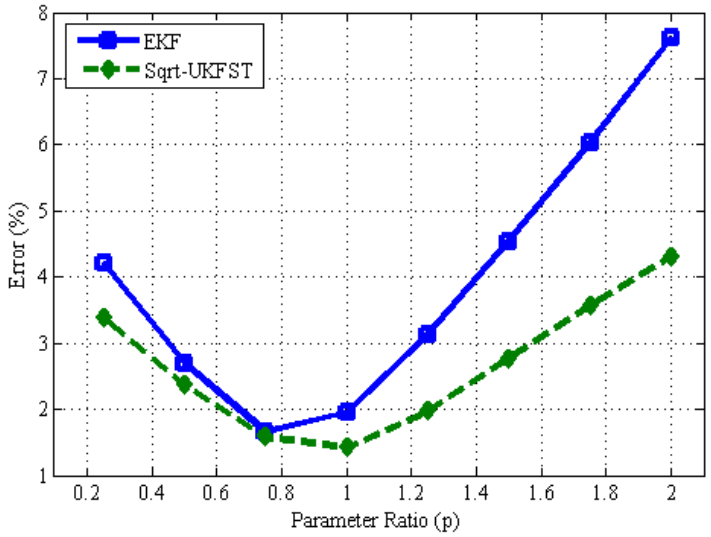

Fig. 4.19 RMSE comparison with different parameters set between EKF and Sqrt-UKFST

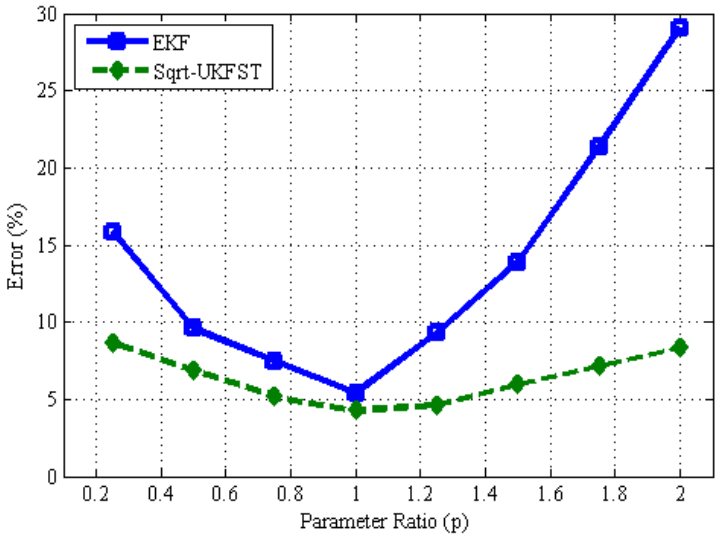

Fig. 4.20 Absolute maximum SOC error comparison with different parameters set between EKF and Sqrt-UKFST

4.4 Summary

Using the double polarization lithium-ion battery model, a new state-of-charge (SOC) estimation method using square root spherical unscented Kalman filter (Sqrt-UKFST) is presented in this chapter. It takes advantage of Jacobian-free linearization approach with unscented Kalman filter. The spherical transform with hyper unit sphere

requires fewer sigma points than the standard UKF and provides a better controllability of the sigma point distribution. In addition, the square root characteristic of the proposed approach improves the numerical properties in state covariance. The experimental results of the proposed approach have been compared with EKF, ampere-hour counting and fuel gauge. The RMSE results have shown that those of EKF, ampere-hour counting and fuel gauge are approximately 37%, 900% and 171% higher than the proposed method respectively. In addition, the parameter variation study shows that the proposed Sqrt-UKFST is more robust than EKF. Furthermore, computational analysis shows that the regular UKF requires 32% more multiplication than Sqrt-UKFST. For the proposed Sqrt-UKFST method, the temperature effect is neglected as a heater for the battery is assumed to be in use. In the next chapter, the temperature effect will be included for the SOC estimation using a dual spherical unscented Kalman filter.

CHAPTER 5

5. DUAL SPHERICAL UNSCENTED KALMAN FILTER BASED STATE-OF-CHARGE ESTIMATION

5.1 Introduction

The square root spherical unscented Kalman filter (UKFST) method proposed in chapter 4 does not consider the temperature effect. In this chapter, the variation of temperature is considered for the SOC estimation using a dual spherical unscented Kalman filter. Ambient temperature is one of the significant factors that affects SOC estimation. Since the satellite operates at different temperatures throughout the orbit, it must be taken care accordingly to safeguard the battery performance and reliability. Moreover, SOC estimation depends on the battery model accuracy as well. The battery parameters are affected by the charging and discharging rates, temperature and SOC. The parameters need to be updated regularly to improve the battery model and the SOC estimation accuracy. The opportunistic SOC estimation in chapter 3 requires a pre-stored lookup table and the accuracy might suffer for the aged cells. The UKFST from chapter 4 addresses all the short falls of the opportunistic SOC estimation but it still lacks the temperature dependency factor in the estimation. This chapter proposes a SOC estimation method and online parameter updating using a dual square root unscented Kalman filter based on unit spherical unscented transform (DUKFST) to include the temperature effect which is lacking in the UKFST.

For DUKFST, the results are compared with EKF and UKFST. Experimental results have shown that it has better performance in terms of lower root mean square error (RMSE) and absolute maximum error across different temperatures at 0°C, 25°C

and 50°C. The improvement is more significant at 0°C and 50°C. The three temperatures are selected based on the satellite operating temperature range in the orbit and the thermal analysis performed by the satellite thermal management team.

5.2 Temperature Dependent Lithium-ion Battery Model

Based on the double polarization battery model in Fig. 3.1, battery parameters are now assumed to be functions of SOC and temperature in DUKFST. Fig. 5.1 shows the temperature dependent equivalent circuit model.

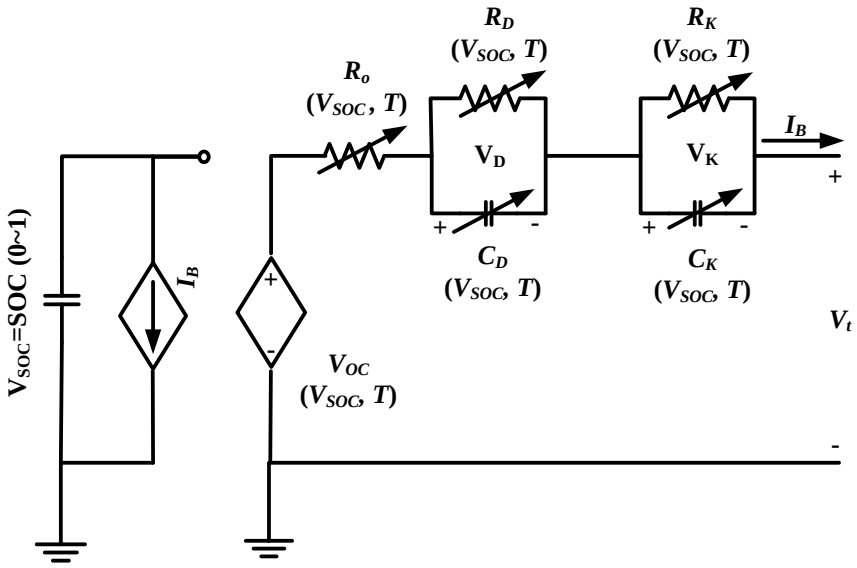

Fig. 5.1 Temperature dependent double polarization model

In Fig. 5.1, V_{OC} is now a function of battery SOC and the temperature T. The battery parameters are affected by ambient temperatures, SOC, current and ageing factors. Among them, the ambient temperature affects the most [177]. In this study, the same lithium-ion battery (NCR18650) as in chapter 3 is used.

Fig. 5.2 shows the experimental battery response at different temperatures when a 1.45A discharge pulse with 10 seconds duration is applied on the battery. Fig. 5.3 illustrates the performance of the battery having different released capacity at different temperatures when the battery is discharged from the fully charged state to the fully

discharged state at a constant 1.45A discharge current. From Figs. 5.2 and 5.3, it is observed that the internal dynamic response of the battery varies at different temperatures. As such, online identification and updating of battery parameters are necessary to improve the battery model accuracy if it is expected to operate at different temperatures.

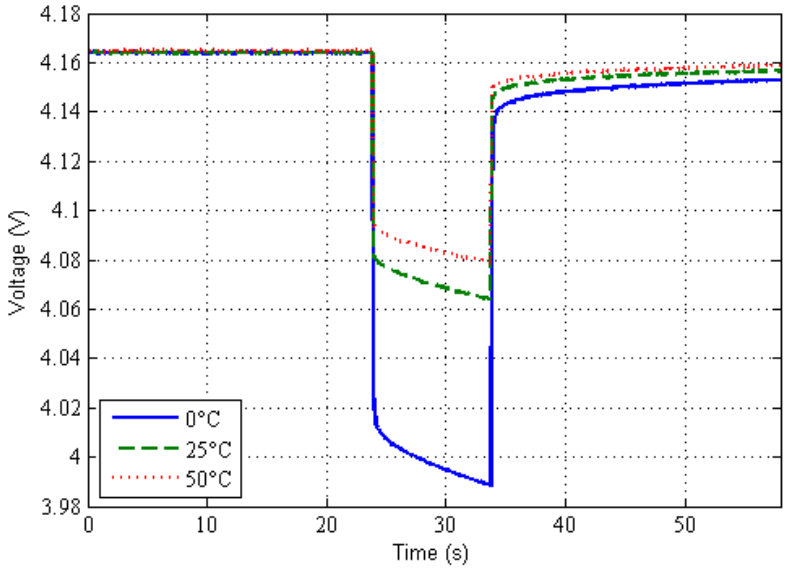

Fig. 5.2 1.45A (0.5C) discharge pulse response at different temperatures (0°C, 25°C and 50°C)

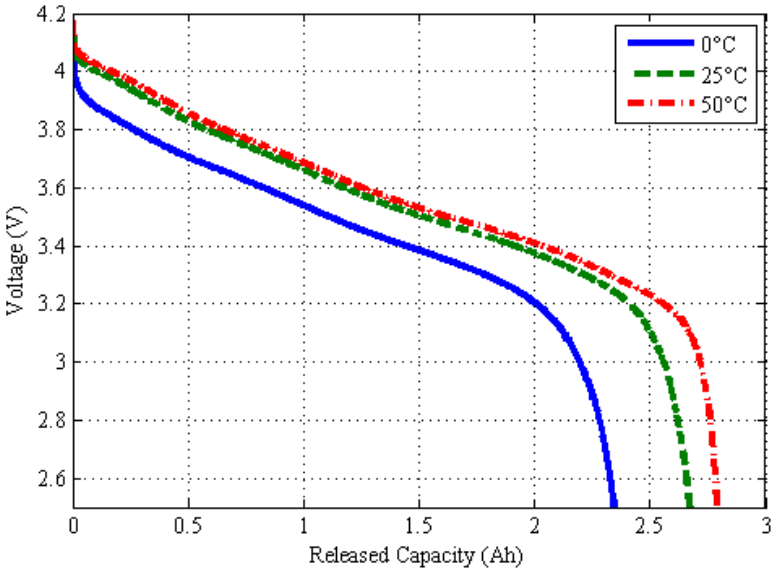

Fig. 5.3 1.45A constant current discharge curve at different temperatures (0°C, 25°C and 50°C)

5.2.1 Open-circuit voltage V_{OC} versus SOC at 0°C, 25°C and 50°C

It is well-known that the V_{OC} and SOC have a nonlinear relationship. The V_{OC} is also affected by ambient temperature as shown in Figs. 5.4 and 5.5. To illustrate the temperature effect on V_{OC}, the battery ambient temperature is varied from 25°C to 0°C (cold temperature) and 25°C to 50°C (hot temperature). Figs. 5.4 and 5.5 show how the V_{OC} changes at different (cold and hot) temperatures. In Fig. 5.4, it is observed that V_{OC} of the battery with a 50% SOC dropped to a lower value when the temperature is decreased from 25°C to 0°C. Moreover, the V_{OC} returns to the original value when the temperature rises to 25°C. Fig. 5.5 shows the case that the temperature is increased from 25°C to 50°C.

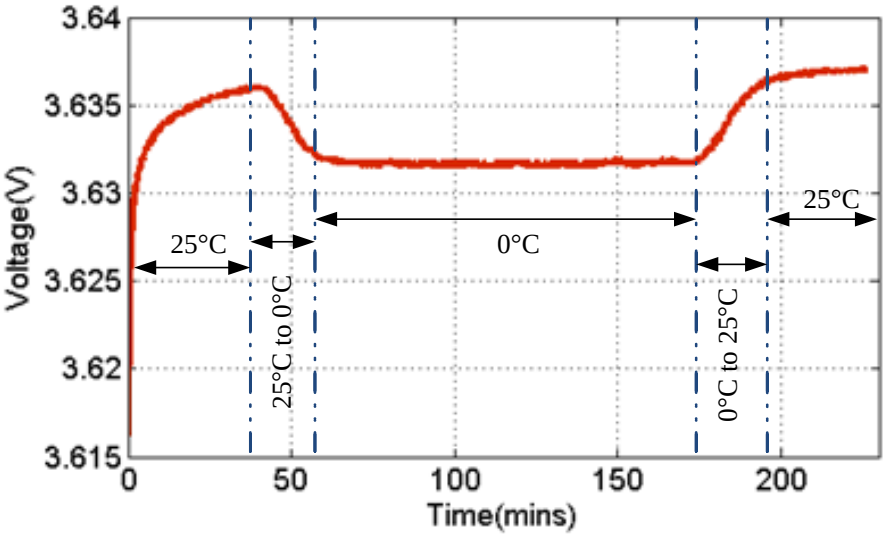

Fig. 5.4 V_{OC} at 50% SOC at 0°C

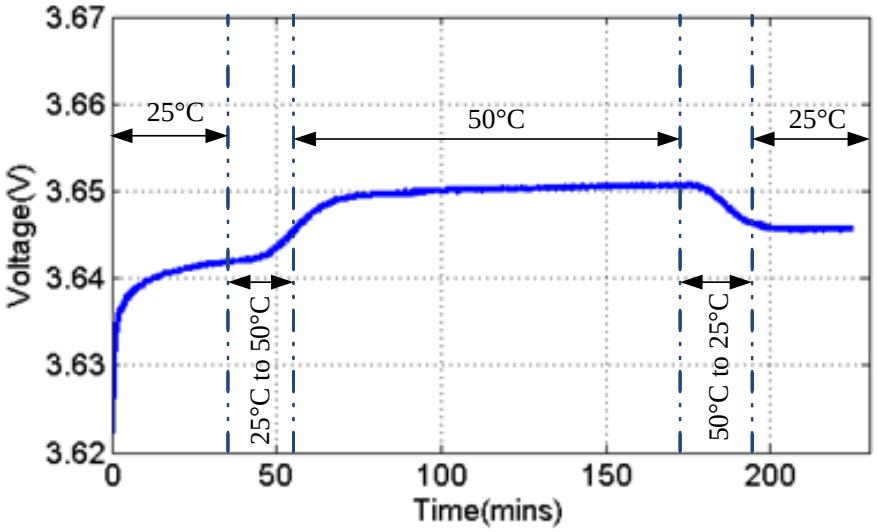

Fig. 5.5 V_{OC} at 50% SOC at 50°C

To study the relationship between V_{OC} and SOC, the open-circuit test is performed [178]. The hysteresis effect of battery is neglected in this test [167-169]. For this experiment, the battery is first fully charged using the constant current and constant voltage (CC-CV) method. It is then rested for an hour to allow V_t to reach the equilibrium voltage and V_t is recorded as V_{OC}. The battery is subsequently discharged at 10% SOC level interval by a constant discharge current of 0.58A followed by 1 hour rest period before V_{OC} is measured. The experiment is repeated until the battery is fully discharged. V_{OC} at different temperatures (0°C and 50°C) are subsequently measured in the same manner using a thermal chamber. Fig. 5.6 shows the V_{OC} and SOC relationship at 0°C, 25°C and 50°C. In Fig. 5.6, the V_{OC} at the fully discharged stage is around 3.2V and is different from the maximum discharge voltage of 2.5V. The maximum discharge voltage is the minimal allowable voltage for a battery at any time. The fully discharged V_{OC} is obtained after resting the battery for an hour once it is discharged till the maximum discharge voltage. Similar characteristics in terms of voltage difference between the discharge curve and the OCV-SOC relationship can also be found in [178].

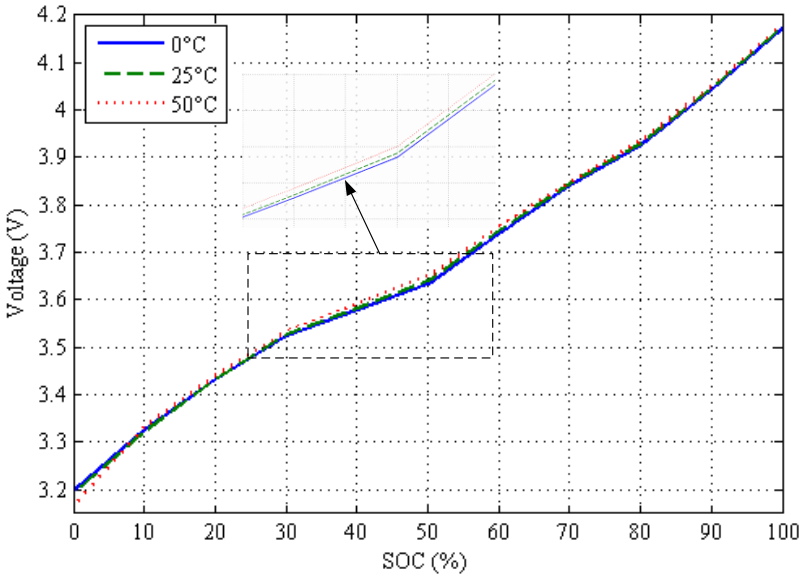

Fig. 5.6 V_{OC} versus SOC at 0°C, 25°C and 50°C

Using Fig. 5.6, the relationship of V_{OC} and SOC (ζ) can be described by a 7th order polynomial using a polynomial curve-fitting method as follows:

$$V_{OC}(\zeta,\ T) = m_1\zeta^7 + m_2\zeta^6 + ... + m_6\zeta^2 + m_7\zeta + m_8 \tag{5.1}$$

where the coefficients are the same as (4.6) for the case of T = 25°C.

5.2.2 Battery state space model

Let ζ be the battery SOC, V_D and V_K be the voltages across the two RC networks in Fig. 5.1. The dynamics of the system are given by

$$\dot{\zeta}(\dot{V}_{SOC}) = -\frac{I_B}{Q_b} \tag{5.2}$$

$$\dot{V}_D(\zeta,\ T) = -\frac{V_D}{R_D(\zeta,T)C_D(\zeta,T)} + \frac{I_B}{C_D(\zeta,T)} \tag{5.3}$$

$$\dot{V}_K(\zeta,\ T) = -\frac{V_K}{R_K(\zeta,T)C_K(\zeta,T)} + \frac{I_B}{C_K(\zeta,T)} \tag{5.4}$$

where Q_b represents the battery nominal capacity from the battery datasheet after ignoring the temperature and cycle dependencies and T is the battery temperature. Let

the battery internal state variables, x, be defined as $x = \begin{bmatrix} \hat{\zeta} & \hat{V}_D & \hat{V}_K \end{bmatrix}^T$ and the battery parameters be defined as $z = \begin{bmatrix} \hat{R}_o & \hat{R}_D & \frac{1}{\hat{C}_D} & \hat{R}_K & \frac{1}{\hat{C}_K} \end{bmatrix}^T$. Using Fig. 5.1 and (5.2)-(5.4), the battery state process function, F, and measurement function, H, can then be derived as

$$\begin{aligned} F(\zeta,\ V_D,\ V_K,\ T) &= \begin{bmatrix} \zeta_{k+1} \\ V_{D_{k+1}} \\ V_{K_{k+1}} \end{bmatrix} \\ &= \begin{bmatrix} 1 & 0 & 0 \\ 0 & e^{\frac{-\Delta t}{R_D C_D}} & 0 \\ 0 & 0 & e^{\frac{-\Delta t}{R_K C_K}} \end{bmatrix} \begin{bmatrix} \zeta_k \\ V_{D_k} \\ V_{K_k} \end{bmatrix} + \begin{bmatrix} -\frac{\Delta t}{Q_b} \\ R_D(1-e^{\frac{-\Delta t}{R_D C_D}}) \\ R_K(1-e^{\frac{-\Delta t}{R_K C_K}}) \end{bmatrix} \begin{bmatrix} I_B \end{bmatrix} \end{aligned} \tag{5.5}$$

$$\begin{aligned} \hat{V}_t &= H(x, z, I_B, T) \\ &= \hat{V}_{OC}(f(V_{SOC}, T)) - \hat{V}_D(V_{SOC}, T) - \hat{V}_K(V_{SOC}, T) - I_B \hat{R}_o(V_{SOC}, T) \end{aligned} \tag{5.6}$$

where Δt represents the sampling time, I_B is the battery current and V_t is the measured terminal voltage. Battery parameters need to be known to estimate the battery state variables. The identified parameters in Table 4-2 are taken as the initial battery parameters. However, these battery parameters vary at different temperature and SOC. They are updated through a spherical square root unscented Kalman filter, which will be explained in the next section.

5.3 Dual Spherical Square Root Unscented Kalman Filter

For the proposed approach, the DUKFST uses two separate Kalman filters for state estimation and parameter estimation/update. The matrix operations are simpler than than those of joint estimations which combine the state and parameters into a single system

[179]. It uses two Sqrt-UKFST presented in chapter 4 to incorporate the temperature effect. One is used as state estimator for the SOC and the other is to update the parameters of the battery. For dual estimation, the battery cell dynamics to explicitly include the parameters can be written as

$$\hat{x}_{k+1} = f\left(\hat{x}_k,\ u_k,\ \hat{z}_k\right) + Q_k^x \tag{5.7}$$

$$\hat{y}_k = h\left(\hat{x}_k,\ u_k,\ \hat{z}_k\right) + R_k^x \tag{5.8}$$

$$\hat{z}_{k+1} = \hat{z}_k + Q_k^z \tag{5.9}$$

$$\hat{d}_k = h\left(\hat{x}_k,\ u_k,\ \hat{z}_k\right) + R_k^z \tag{5.10}$$

where u_k is the system input variables, x_k is the system state variables, z_k is the time varying parameters and y_k and d_k are the state output variables. The state-space and the measurement models of $f(x, u, z)$ and $h(x, u, z)$ are (5.5) and (5.6) respectively. Let $Q_k \sim N(0, cov_Q)$ and $R_k \sim N(0, cov_R)$ represent the uncorrelated zero-mean white Gaussian process and measurement noise. The parameter dynamic equation in (5.9) implies that the parameters remain constant but they change slowly over time through the R_k^z process noise [97, 179]. With these two systems defined, the same procedure of Sqrt-UKFST in chapter 4 can be used for state estimator and parameter update.

The error covariance of Q and R can affect the filter performance as well. To further improve the filter performance, different adaptive filtering methods of maximum likelihood, Bayesian estimation and covariance matching have been used to adaptively update Q and R [180]. However, the simultaneous adaptation of both Q_k and R_k is not considered robust as discussed in [181]. It is the state process noise Q_k, which is unknown and it can be updated with the adaptive factor α [182, 183] using covariance

matching. Covariance matching makes the elements of the innovation or residual-based covariance matrix consistent with the theoretical values. This is possible by the established principle that the estimated covariance matrix of the innovations or residuals should match with its theoretical form [180, 181]. Based on this principle, the updating of Q takes place. The innovation sequence v_k and its theoretical covariance ($E\left\{v_k v_k^T\right\}$) can be expressed as [181]

$$v_k = y_k - h_k \hat{x}_k^- \tag{5.11}$$

$$E\left\{v_k v_k^T\right\} = h_k \hat{P}_k^- h_k^T + R_k \tag{5.12}$$

where y_k is the output measurement, h_k is the measurement function, $\hat{x}_k^-$ is the state estimate before Kalman gain is applied and $\hat{P}_k^-$ ($\hat{P}_k^- = S_k^-\left(S_k^-\right)^T$) is the predicted state covariance matrix. The innovation covariance C_v can be estimated over a window length of N using the covariance sequence as

$$C_v^{k,N} = \frac{1}{N}\sum_{j=k-N+1}^{k} v_j v_j^T \tag{5.13}$$

Using the covariance matching principle, the estimated covariance in (5.13) should match its theoretical covariance (5.12) as

$$\frac{1}{N}\sum_{j=k-N+1}^{k} v_j v_j^T = h_k \hat{P}_k^- h_k^T + R_k \tag{5.14}$$

With R_k and $\hat{P}_k^-$, Q_k can be updated through the use of the adaptive factor α. The factor α can calculated as the ratio between the estimated innovation covariance and the predicted state covariance [182, 183].

$$\alpha = \frac{trace\left\{\hat{C}_v - R_k\right\}}{trace\left\{h_k \hat{P}_k^- h_k^T\right\}} = \frac{trace\left\{\hat{C}_v - R_k\right\}}{trace\left\{h_k S_k^- \left(S_k^-\right)^T h_k^T\right\}} \tag{5.15}$$

where f_k is the state transition function. With α, Q at epoch k can then be stimated as

$$\hat{Q}_k = \alpha \hat{Q}_{k-1} \tag{5.16}$$

With the adaptive process noise, dual estimation with two separate Kalman filters can be used for state and parameters estimation [96, 179]. The DUKFST is performed as follows:

1) *Initialization*:

The initial state $x = \begin{bmatrix} \hat{\zeta} & \hat{V}_D & \hat{V}_K \end{bmatrix}^T$. Its initial state covariance $\left(S_{x_0}\right)$, the initial parameter $z = \begin{bmatrix} \hat{R}_o & \hat{R}_D & \frac{1}{\hat{C}_D} & \hat{R}_K & \frac{1}{\hat{C}_K} \end{bmatrix}^T$ and its covariance $\left(S_{z_0}\right)$ are initialized using (5.17) and (5.18).

$$\hat{x}_0 = E\left[x_0\right],\ S_{x_0} = chol\left\{E[(x_0 - \hat{x}_0)(x_0 - \hat{x}_0)^T]\right\} \tag{5.17}$$

$$\hat{z}_0 = E\left[z_0\right],\ S_{z_0} = chol\left\{E[(z_0 - \hat{z}_0)(z_0 - \hat{z}_0)^T]\right\} \tag{5.18}$$

where *chol* represents the Cholesky factor calculation.

2) *Parameter time update*:

A *priori* state and error covariance for z are calculated using (5.19)-(5.21). A *priori* parameter time update $z_{i,k-1}$ are computed in (5.20) using the sigma points $Z_i^{n_z}$ and the error covariance $S_{z_{k-1}}$. The sigma points are generated using Table 4-3.

$$\hat{z}_k^- = \hat{z}_{k-1} \tag{5.19}$$

$$z_{i,k-1} = \hat{z}_{k-1} + S_{z_{k-1}} Z_i^{n_z} \tag{5.20}$$

where $i = 0,1,....,n_z + 1$.

A *priori* parameter error covariance $S_{z_k}^-$ is calculated using (5.21).

$$S_{z_k}^- = \lambda_{RLS}^{-1/2} S_{z_{k-1}} \tag{5.21}$$

where $\lambda_{RLS}^{-1/2} \in (0,1]$.

3) *State time update*:

A *priori* state and error covariance for *x* are calculated using (5.22)-(5.26). The sigma points $\chi_i^{n_x}$ and their weightage W_x are generated using Table 4-3. The generated sigma points are propagated through the state function in (5.5). A *priori* state $\hat{x}_k^-$ is calculated using the propagated sigma points $\chi_{k|k-1}$ in (5.24).

$$\chi_{i,k-1} = \hat{x}_{k-1} + S_{x,k-1}\chi_i^{n_x} \tag{5.22}$$

$$\chi_{k|k-1} = F(\chi_{k-1}, I_{B,k-1}) \tag{5.23}$$

$$\hat{x}_k^- = \begin{bmatrix} \hat{\zeta}_k^- & \hat{V}_D^- & \hat{V}_K^- \end{bmatrix}^T = \sum_{i=0}^{n+1} W_{x,i}\chi_{k|k-1} \tag{5.24}$$

where $i = 0,1,....,n_x + 1$.

A *priori* state error covariance $S_{x,k}^-$ can be calculated using (5.25) and (5.26) as follows:

$$S_{x,k}^- = qr\left\{\begin{bmatrix} \sqrt{W_{x,i}}(\chi_{1:n+1,k|k-1} - \hat{x}_k^-) & \sqrt{Q_x} \end{bmatrix}\right\} \tag{5.25}$$

$$S_{x,k}^- = cholupdate\{S_{x,k}^-, \chi_{0,k|k-1} - \hat{x}_k^-, W_{x,0}\} \tag{5.26}$$

where *qr* and *cholupdate* represent the QR factorization and Cholesky factor update.

4) *State filter Output estimate*:

The propagated sigma points are then used to calculate the output sigma points Υ_k using (5.6) in (5.27). The system output $\hat{y}_k^-$ is estimated using these Υ_k in (5.28).

$$\Upsilon_{k|k-1} = H[\chi_{k|k-1},\ I_{B,k-1}] \tag{5.27}$$

$$\hat{y}_k^- = \hat{V}_t^- = \sum_{i=0}^{n+1} W_{x,i}\Upsilon_{i,k|k-1} \tag{5.28}$$

Update the output covariance $S_{\tilde{y}_k}$ using (5.29) and (5.30).

$$S_{\tilde{y}_k} = qr\{[\sqrt{W_{x,i}}(\Upsilon_{1:n+1,k|k-1} - \hat{y}_k^-) \quad \sqrt{R}]\} \tag{5.29}$$

$$S_{\tilde{y}_k} = cholupdate\{S_{\tilde{y}_k}, \Upsilon_{0,k|k-1} - \hat{y}_k^-, W_{x,0}\} \tag{5.30}$$

5) *State filter Kalman gain*:

Calculate the cross covariance matrix $P_{x_k y_k}$ and the state filter Kalman gain K_x using (5.31) and (5.32) as

$$P_{x_k y_k} = \sum_{i=0}^{n+1} W_{x,i}(\chi_{i,k|k-1} - \hat{x}_k^-)(\Upsilon_{i,k|k-1} - \hat{V}_{t,k}^-)^T \tag{5.31}$$

$$K_{x,k} = P_{x_k y_k} S_{\tilde{y}_k}^{T^{-1}} S_{\tilde{y}_k}^{-1} \tag{5.32}$$

6) *State filter measurement update*:

The state estimate $\hat{x}_k^+$ is updated through measurement V_t, K_x and $\hat{x}_k^-$ in (5.33).

$$\hat{x}_k^+ = \hat{x}_k^- + K_{x,k}(V_{t,k} - \hat{V}_{t,k}^-) \tag{5.33}$$

The *posterior* state covariance matrix $S_{x,k}$ is calculated as

$$S_{x,k} = cholupdate\{S_{x,k}^-,\ K_{x,k}S_{\tilde{y}_k},\ -1\} \tag{5.34}$$

The Q_x is updated as

$$C_v^{k,N} = \frac{1}{N}\sum_{j=k-N+1}^{k}(v_j = \hat{x}_k^+ - \hat{x}_k^-)v_j^T \tag{5.35}$$

$$\alpha = \frac{trace\left\{\hat{C}_v - R\right\}}{trace\left\{H_k S_{x,k}^- \left(S_{x,k}^-\right)^T H_k^T\right\}} \tag{5.36}$$

$$\hat{Q}_{x,k} = \alpha \hat{Q}_{x,k-1} \tag{5.37}$$

7) *Parameter filter output estimate*:

The parameter filter output $\hat{d}_k$ is calculated using the sigma-points $D_{k|k-1}$ as follows

$$D_{k|k-1} = H(x_k, Z_i^{n_z}, I_{B,k-1}) \tag{5.38}$$

$$\hat{d}_k = \sum_{i=0}^{n+1} W_{z,i} D_{i,k|k-1} \tag{5.39}$$

Update the parameter filter output covariance as

$$S_{d_k} = qr\left\{\left[\sqrt{W_{z,i}}(Z_{1:n+1,k|k-1} - \hat{z}_k^-) \quad \sqrt{Q_z}\right]\right\} \tag{5.40}$$

$$S_{d_k} = cholupdate\{S_{d_k},\ D_{0,k|k-1} - \hat{d}_k,\ W_{z,0}\} \tag{5.41}$$

8) *Parameter filter Kalman gain $K_{z,k}$*:

Calculate the parameter filter cross covariance matrix $P_{z_k y_k}$ and the Kalman gain K_z as

$$P_{z_k d_k} = \sum_{i=0}^{n+1} W_{z,i}(Z_{i,k|k-1}^+ - \hat{z}_k^-)(D_{i,k|k-1} - \hat{d}_k)^T \tag{5.42}$$

$$K_z = P_{z_k d_k} S_{d_k}^{T^{-1}} S_{d_k}^{-1} \tag{5.43}$$

9) *Parameter filter measurement update*:

The parameter update $\hat{z}_k^+$ is computed below as

$$\hat{z}_k^+ = \hat{z}_k^- + K_z(V_{t,k} - \hat{d}_k^-) \tag{5.44}$$

Lastly, update the parameter *posterior* error covariance and process noise as

$$S_{z_k} = cholupdate\{S_{z_k}^-,\ K_z S_{d_k},\ -1\} \tag{5.45}$$

$$\hat{Q}_{z,k} = \alpha \hat{Q}_{z,k-1} \tag{5.46}$$

The proposed DUKFST overall flowchart is shown in Fig. 5.7.

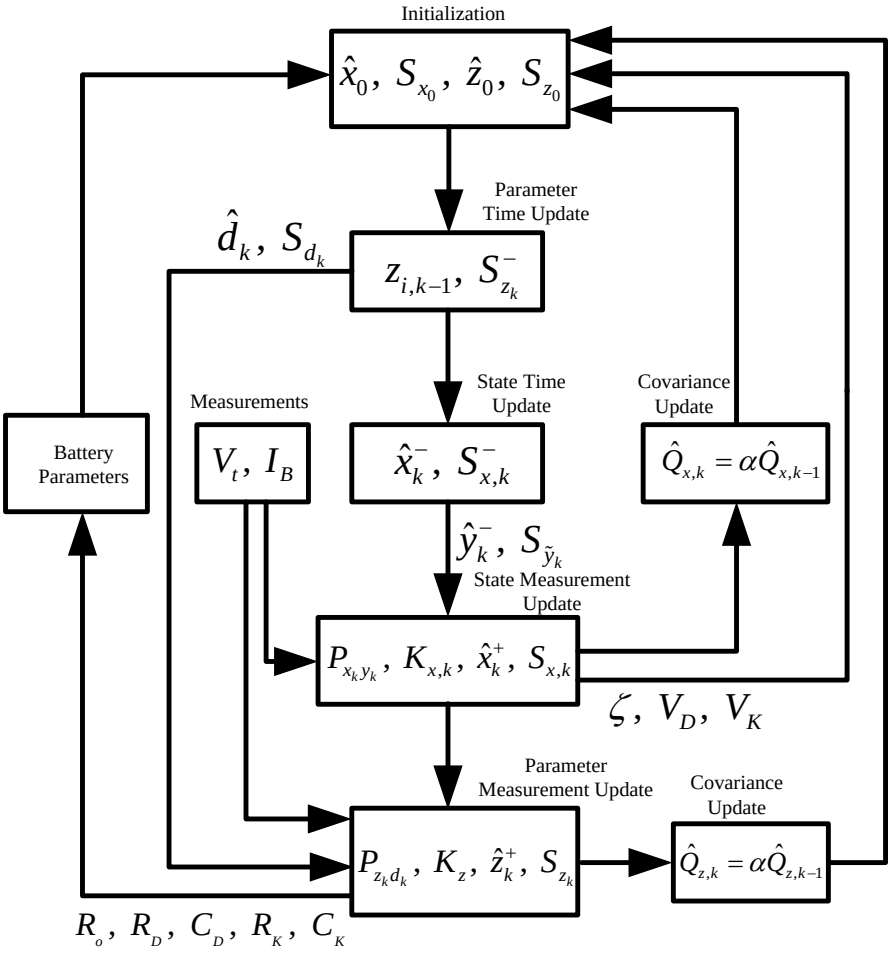

Fig. 5.7 Flowchart of DUKFST

5.4 Simulation and Experimental Evaluation of DUKFST

5.4.1 Simulation study of DUKFST

Using the temperature dependent lithium-ion battery model in Fig. 5.8, the simulation study is performed to verify the proposed DUKFST algorithm. Fig. 5.8 shows the constructed Simulink simulation testbed. Fig. 5.9 presents the discharge and charge load profile used in the simulation. The temperatures used for the simulation are 0°C (cold) and 25°C (hot). Fig. 5.10 shows that the battery operating temperature maintains around 25°C throughout the experiment. The SOC estimation comparison between the reference and DUKFST at 25°C is plotted in Fig. 5.11. The corresponding absolute SOC estimation error at 25°C and 0°C are presented in Figs. 5.12 and 5.13 respectively. Figs. 5.12 and 5.13 show that DUKFST performed better at 25°C than at 0°C. The maximum estimation error is below 2.5% and the DUKFST is able to estimate SOCs correctly at different temperature.

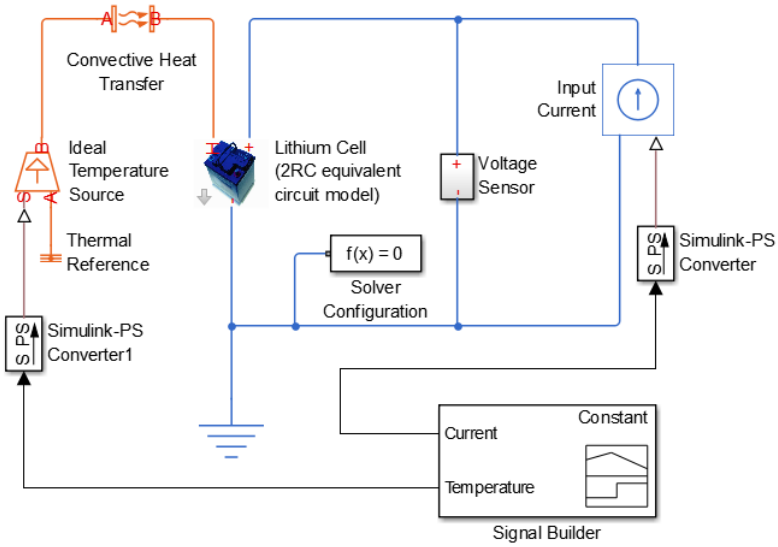

Fig. 5.8 Thermal dependent lithium-ion battery model in Simulink [184]

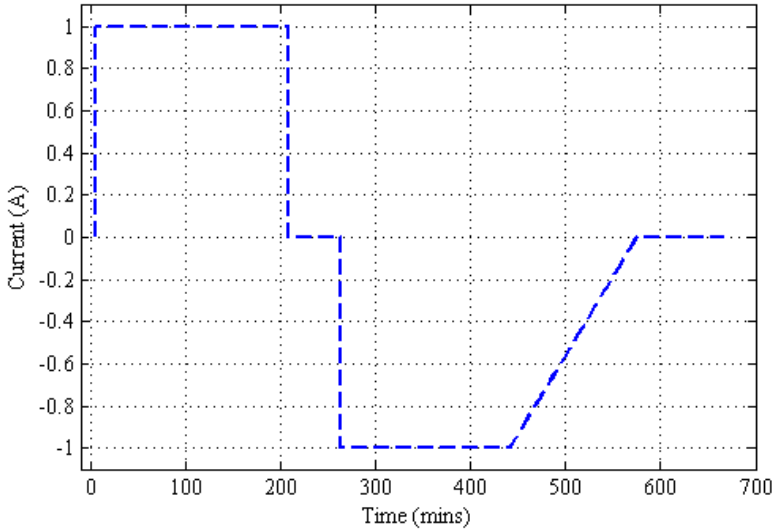

Fig. 5.9 Simulation load profile of DUKFST

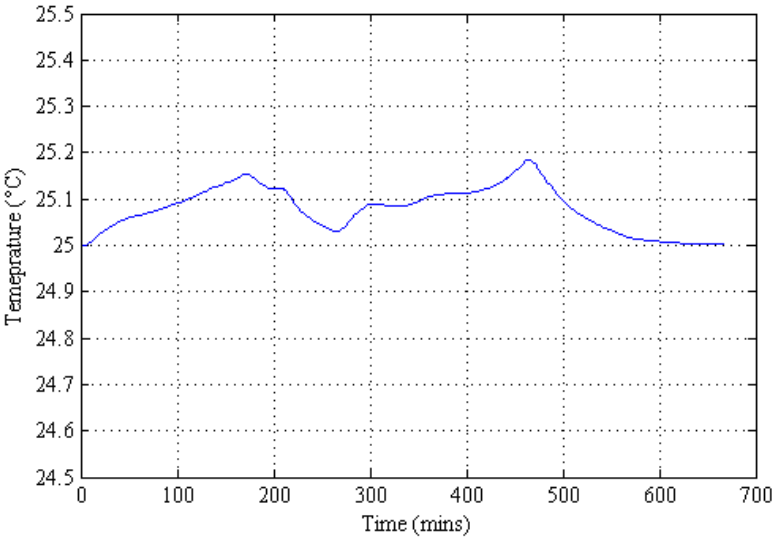

Fig. 5.10 Battery operation temperature at 25°C

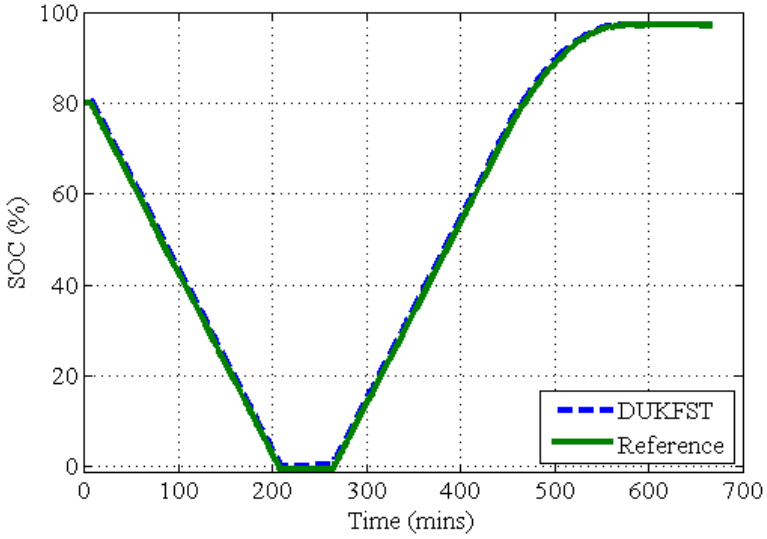

Fig. 5.11 SOC estimation comparison at 25°C

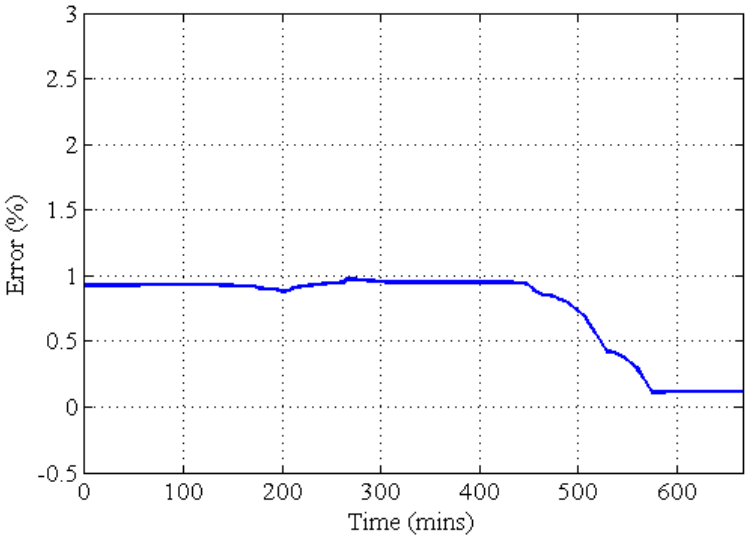

Fig. 5.12 Absolute SOC error comparison at 25°C

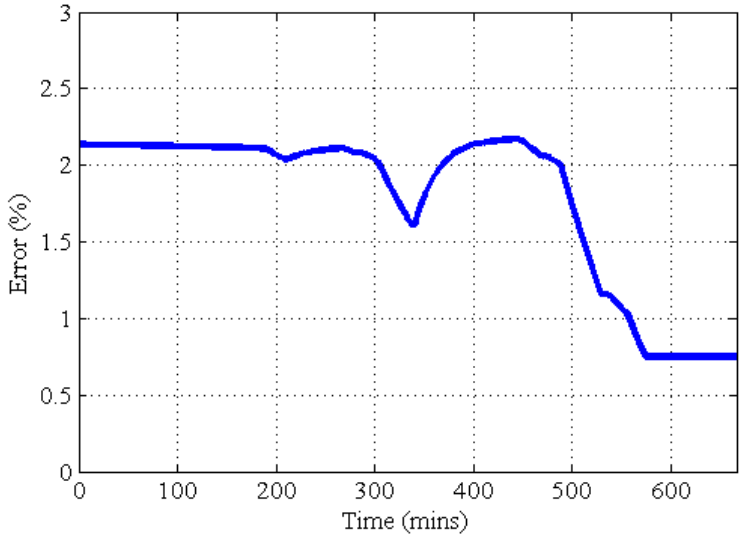

Fig. 5.13 Absolute SOC error comparison at 0°C

Table 5-1 presents the calculated absolute mean, RMSE and maximum error for 0°C and 25°C simulation studies.

Table 5-1 SOC estimation error performance

	25℃	***0℃***
Mean	0.86%	1.97%
RMSE	0.88%	2.00%
Maximum	0.97%	2.20%

5.4.2 Experimental studies of DUKFST

To validate the proposed method experimentally, the same battery test bench as shown in Fig. 3.14 is used in the experiment. The thermal chamber is used to set the different operating range of the battery at different orbits. The temperatures used for the experiment are at 0°C, 25°C and 50°C following the satellite expected temperature range. The setup is then used to perform VELOX-I nanosatellite payload mission experiment as shown in Fig. 5.14 to validate the proposed method. VELOX-I is the first Singapore nanosatellite built by Nanyang Technological University. VELOX-I consists of scientific payloads which include a vision system with extended optics, a dual-field

of view sun sensor and a piggyback pico-satellite VELOX-PIII for satellite communication experiment [185]. There are two different loading profiles for the nanosatellite: normal operation and payload operation. For the normal operation as shown in Fig. 3.15, the load profile does not have many dynamic load changes. The proposed method is compared against the UKFST in the previous chapter and EKF for the performance evaluation.

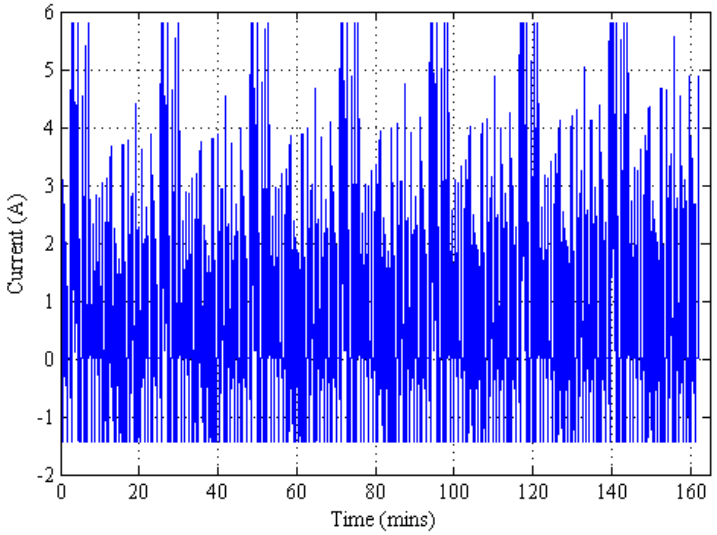

Fig. 5.14 VELOX-I nanosatellite payload current profile

1) Robustness and convergence study in terms of initial SOC error

The proposed method is first verified for its robustness in terms of initial SOC error. Assuming that there is an error in the initial SOC, the SOC estimation is performed with the load profile as shown in Fig. 5.14. The battery is first fully charged using the CC-CV method. Due to the high initial charging current (1.45A) of the load profile, the battery charging voltage exceeds the absolute charge voltage limit of 4.2V and this could damage the battery. In order to safeguard the charged safety limit voltage when using the load profile, the battery is discharged to 80% SOC by a discharge current of 0.29A (0.1C). Different initial SOC errors in terms of 10% SOC intervals from 0% to 100%

are considered for the proposed method at three different temperatures: 0°C, 25°C and 50°C. Fig. 5.15 shows the convergence of initial error analysis at 25°C when the reference SOC is 80%. It can be observed that the proposed method converges to the actual SOC within 20s. To further validate the convergence performance of the proposed method, different reference SOCs, i.e. 40%, 60% and 80%, are performed at 0°C, 25°C and 50°C. Fig. 5.16 shows that the DUKFST is able to converge to the reference SOC across the entire operation range with the maximum estimation error of 2.4% at 25°C.

Table 5-2 and 5-3 summarize the performance at 0°C and 50°C. The results show that the initial estimation error does not impact the convergence of the SOC estimation using the proposed DUKFST.

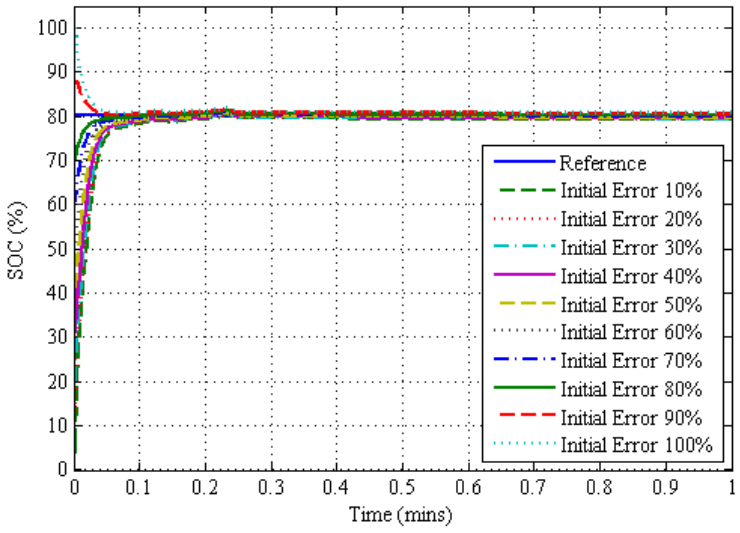

Fig. 5.15 Initial SOC error convergence study at 25°C with different initial errors

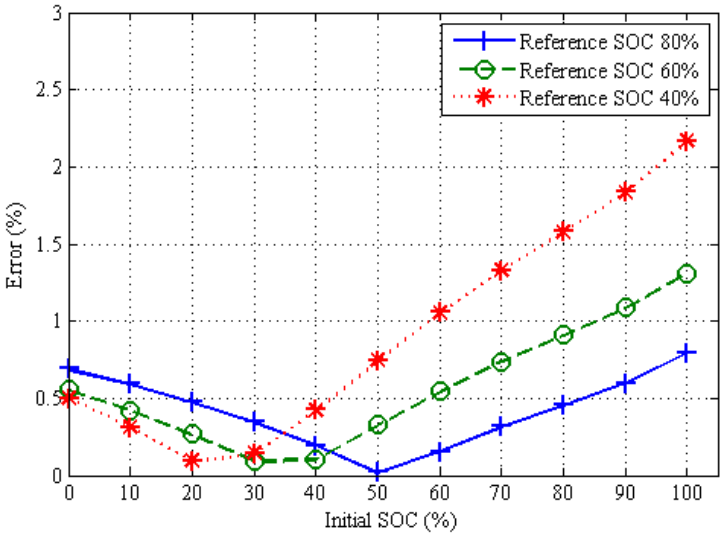

Fig. 5.16 SOC estimation error under unknown initial SOC at 25°C

Table 5-2 Initial SOC error analysis at 0°C

		Estimation error at 80% Reference SOC (%)	***Estimation error at 60% Reference SOC (%)***	***Estimation error at 40% Reference SOC (%)***
Initial SOC Error (%)	***100***	0.57	4.12	0.31
	90	0.38	3.92	0.05
	80	0.24	3.76	0.31
	70	0.11	3.61	0.58
	60	0.06	3.44	0.88
	50	0.22	3.25	1.21
	40	0.4	3.05	1.56
	30	0.55	2.87	1.87
	20	0.67	2.72	2.13
	10	0.79	2.58	2.36
	0	0.88	2.46	2.57

Table 5-3 Initial SOC error analysis at 50°C

		Estimation error at 80% Reference SOC (%)	***Estimation error at 60% Reference SOC (%)***	***Estimation error at 40% Reference SOC (%)***
Initial SOC Error (%)	***100***	0.37	4.47	0.64
	90	0.08	4.14	1.1
	80	0.13	3.89	1.48
	70	0.35	3.67	1.79
	60	0.58	3.43	2.1
	50	0.78	2.22	2.39
	40	0.92	3.04	2.64
	30	1.05	2.89	2.86
	20	1.2	2.71	3.09
	10	1.38	2.51	3.37
	0	1.56	2.28	3.67

2) SOC Estimation at 0°C, 25°C and 50°C

For a given initial SOC and the battery parameters in Table 4-2, SOC estimation based on DUKFST is performed using the load profile in Fig. 5.14 at three different temperatures: 0°C, 25°C and 50°C. The performance of the proposed method is then compared with UKFST and EKF. For performance evaluation, the RMSE and absolute maximum errors in (4.27) and (4.28) are used. Figs. 5.17 and 5.18 present the SOC estimation using different approaches and the absolute error between the estimated and reference SOC at 50°C for each method. From Fig. 5.17, it can be observed that DUKFST and UKFST follow more closely to the reference SOC than the EKF. Fig. 5.18 shows that DUKFST produces the least error.

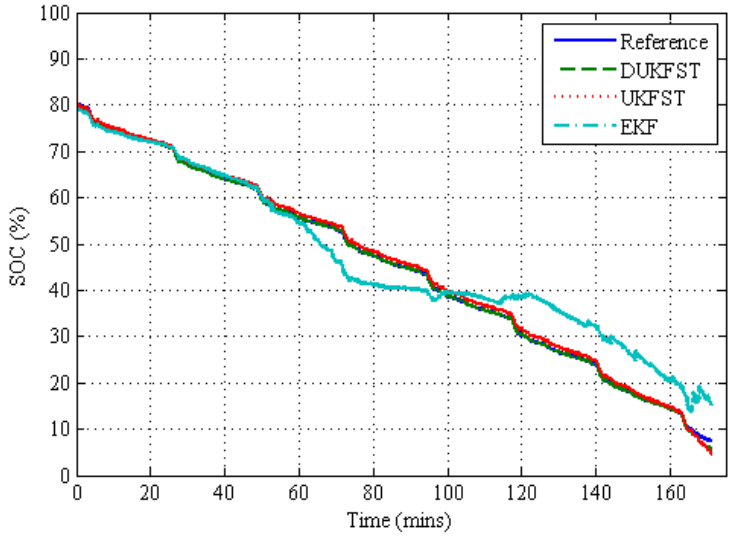

Fig. 5.17 SOC comparison at 50°C

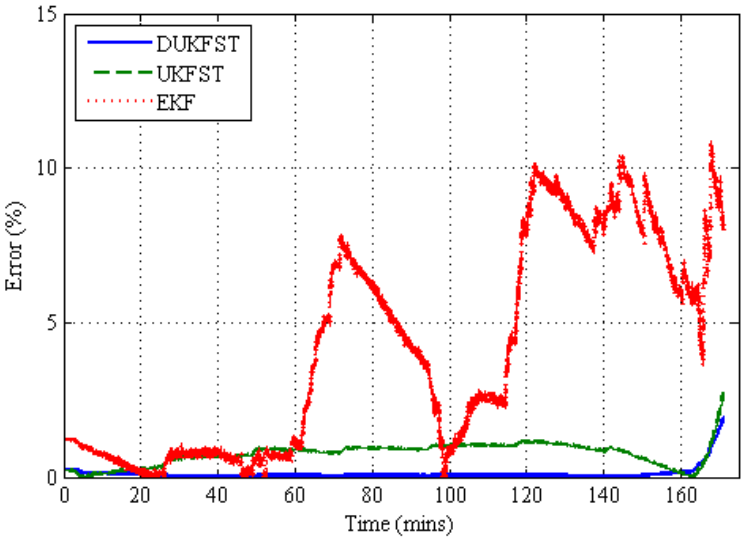

Fig. 5.18 SOC error comparison at 50°C

Using the same load profile, the experiment is also conducted at 0°C and 25°C. Figs. 5.19 and 5.20 show the corresponding absolute SOC error. From Figs. 5.18 to 5.20, it is noted that the proposed method outperforms the UKFST and EKF especially at 0°C and 50°C.

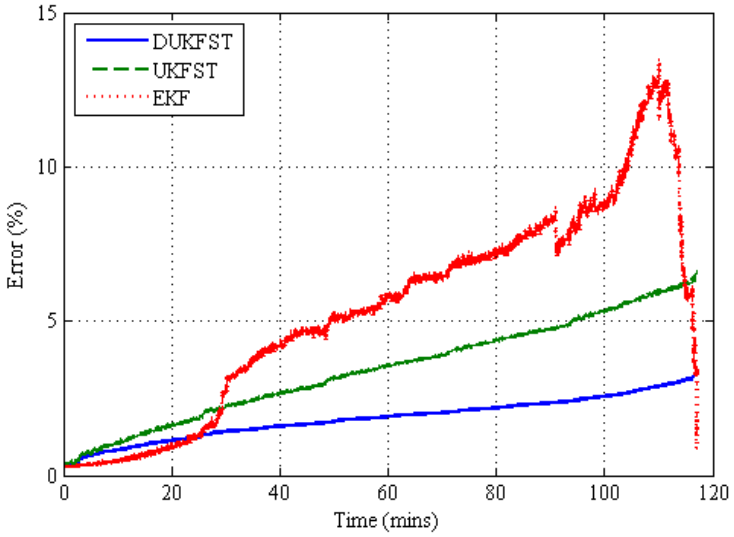

Fig. 5.19 SOC error comparison at 0°C

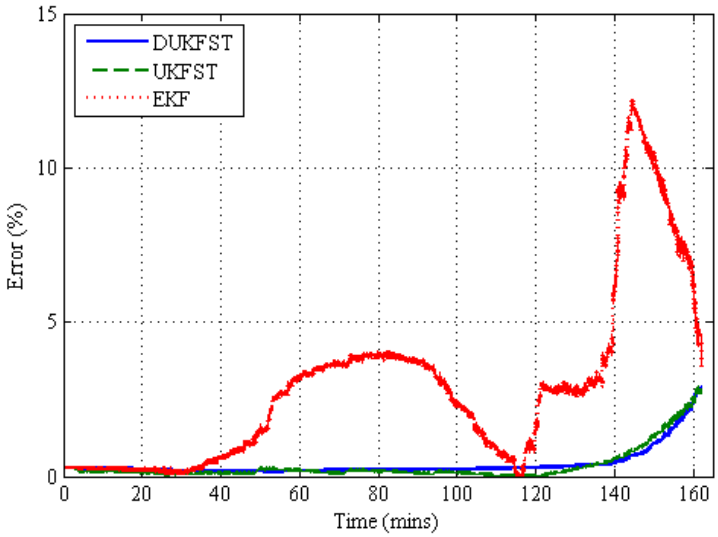

Fig. 5.20 SOC error comparison at 25°C

The improvement in performance is due to the updating of battery parameters by the proposed method. Figs. 5.21-5.23 show the values of R_o, τ_D ($\tau_D = R_D C_D$) and τ_K ($\tau_K = R_K C_K$) at 0°C, 25°C and 50°C. These estimated values during the experiment are plotted against SOC to have a clearer understanding how the battery parameters change across different SOC levels and temperatures. It can be observed that the parameters of the battery vary across different temperature and SOC. Table 5-4 shows the performance comparison between the proposed DUKFST, UKFST and EKF. From Table 5-4, it can

be seen that DUKFST has a lower RMSE and maximum error than those of UKFST and EKF across different temperatures.

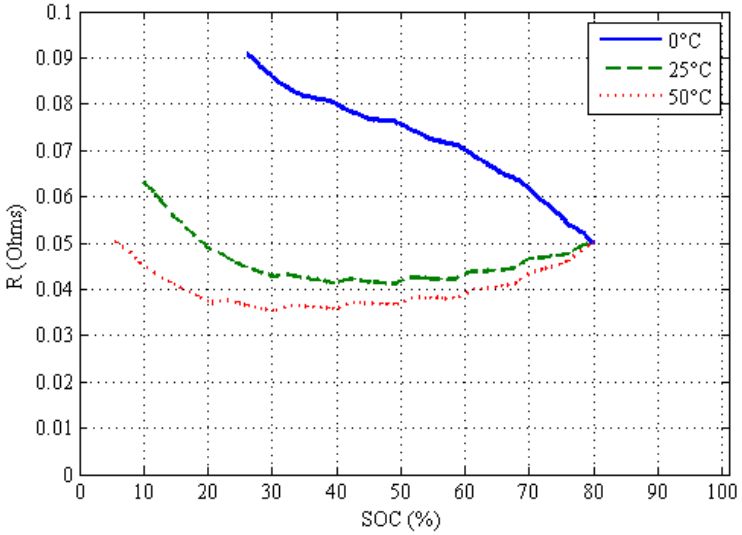

Fig. 5.21 R_o at 0°C, 25°C and 50°C

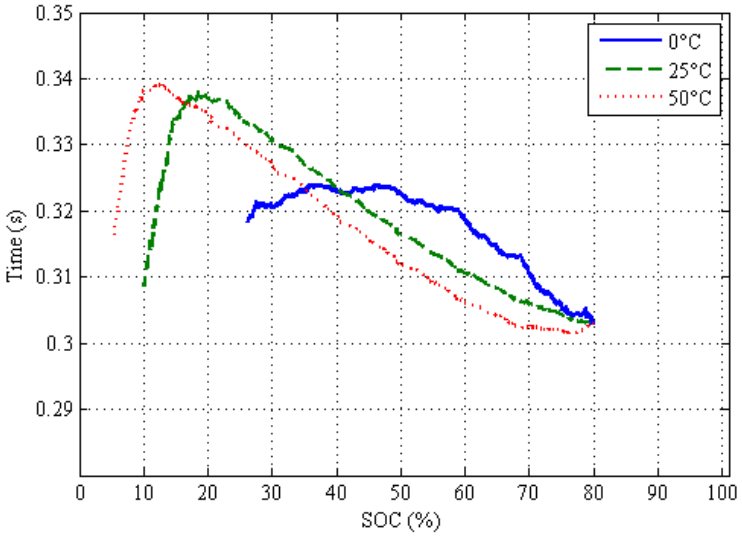

Fig. 5.22 τ_D at 0°C, 25°C and 50°C

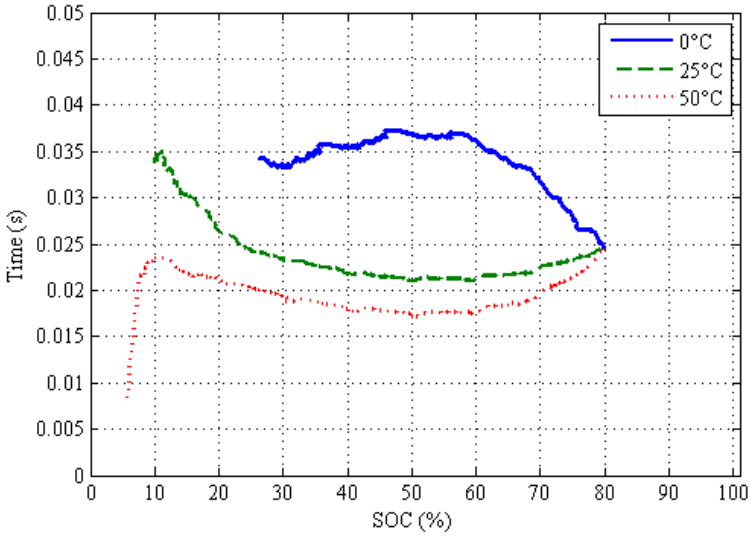

Fig. 5.23 τ_K at 0°C, 25°C and 50°C

Table 5-4 Performance comparison at 0°C, 25°C and 50°C

		DUKFST	***UKFST***	***EKF***
0°C	***RMSE***	1.96%	3.78%	6.3%
	Maximum	3.36%	6.66%	13.5%
25°C	***RMSE***	0.58%	0.62%	4.1%
	Maximum	2.86%	2.9%	12.2%
50°C	***RMSE***	0.36%	0.83%	5.3%
	Maximum	1.93%	2.73%	10.8%

3) Computational requirement

Table 5-5 compares the number of multiplications required in each operation for the DUKST, UKFST and EKF. In Table 5-5, "*n*", *"z"* and "*L*" denote the number of states, the number of parameters and the number of measurements respectively. From the table, it is observed that DUKFST has the most number of multiplications. Comparing DUKFST and UFKST, the total number of multiplication increased from 81 to 334. However this also resulted in the improved performance of 93% and 98% for RMSE and absolute maximum error respectively at 0°C. For comparison with EKF at 0°C, it represents 221% and 302% improvement for the RMSE and absolute maximum error respectively.

Table 5-5 Multiplication comparison analysis between DUKST, UKFST and EKF

	Multiplication Required		
Operation	*DUKFST*	*UKFST*	*EKF*
P_{xx}	$(n + 2)n^2$	$(n + 2)n^2$	-
P_{xy}	$(n + 2)(nL)$	$(n + 2)(nL)$	-
P_{yy}	$(n + 2)L^2$	$(n + 2)L^2$	-
$PH^T(HPH^T + R)$	-	-	$L^3 + 2nL^2 + 2n^2L$
$K(y - \hat{y})$	$L^3 + nL^2 + nL$	$L^3 + nL^2 + nL$	$nL + Ln^2$
$P - KP_{yy}K$	Ln^2	Ln^2	$n^2L + n^3$
Total Multiplication Required	$253(z = 5, L = 1)$ $+ 81(n = 3, L = 1) = 334$	$81(n = 3, L = 1)$	$73(n = 3, L = 1)$

5.5 Summary

Operating temperature of the satellite varies significantly from 0 to 30°C for internal temperature and from -40 to 75°C for external temperature in one orbit which lasts around 100 minutes. The different operating temperature affects its battery parameters and SOC. The SOC estimation accuracy is therefore degraded if the temperature fluctuates. In this chapter, a new SOC estimation method and an online parameter updating algorithm using a dual square root unscented Kalman filter (DUKFST) with unit spherical unscented transform is presented to overcome the lack of temperature factor in the UKFST in chapter 4. The experimental results demonstrate that the proposed DUKFST outperforms the UKFST and EKF with the lowest RMSE and the lowest maximum errors. The improvement is particularly significant at 0°C and 50°C. This improvement in performance is at the expense of an increased computational requirement. All KFs based approaches are affected by the measurement and process noise. It is beneficial if it can be eliminated to minimize the performance degradation from the incorrect noise covariance. This has led to the development of particle swarm optimization (PSO) with inverse barrier constraint SOC estimation in the next chapter.

CHAPTER 6

6. PARTICLE SWARM OPTIMIZATION STATE-OF-CHARGE ESTIMATION

6.1 Introduction

Square root spherical unscented Kalman filter (UKFST) and dual unscented Kalman filter (DUKFST) based methods have been proposed to improve the shortcomings of extended Kalman filter (EKF) in chapters 4 and 5 respectively. All Kalman filter based methods require the knowledge of process and measurement noise. Consequently, poor convergence rates will occur if they are not determined correctly. Chemical reactions of the battery internal operations are complicated. Thus it is difficult to obtain the process and measurement noise information accurately. Kalman filters also require the noise to be Gaussian for the results to be optimal. To overcome these shortcomings, a state-of-charge (SOC) estimation approach based on particle swarm optimization (PSO) with inverse barrier constraint is proposed in this chapter. This method overcomes the need to linearize the model and does not require the information on measurement and process noise. The proposed method has been verified experimentally and compared against DUKST, UKFST and EKF. From the experimental results, the root mean square error (RMSE) of PSO is 1.36% and absolute maximum error of PSO is 4.01%, which has a lower RMSE and maximum error than EKF. The PSO performance is comparable with DUKST and have lower RMSE than UKFST.

6.2 Particle Swarm Optimization based SOC Estimation

Using the equivalent circuit model in Fig. 3.1 and (4.2)-(4.5), the voltages of two RC networks, V_D and V_K, and the battery terminal voltage V_t are written as

$$V_{D_{k+1}} = V_{D_k} e^{\frac{-t}{\tau_D}} + I_B R_{D_k} (1 - e^{\frac{-t}{\tau_D}}) \tag{6.1}$$

$$V_{K_{k+1}} = V_{K_k} e^{\frac{-t}{\tau_K}} + I_B R_{K_k} (1 - e^{\frac{-t}{\tau_K}}) \tag{6.2}$$

$$V_t = V_{OC}(f(SOC = \varphi)) - I_B R_o - V_D - V_K \tag{6.3}$$

Using (6.1)-(6.3), the measured values of R_o and V_{OC} can be extracted from the measured battery voltage V_t and current I_B. Once the battery V_{OC} is known, the SOC can be estimated through the SOC-V_{OC} equation in (4.6). From (4.8), the transfer function $G(s)$ is written as

$$\begin{aligned} G(s) &= \frac{V_t(s) - \hat{V}_{OC}(s)}{I_B(s)} = -\frac{a_2 s^2 + a_1 s + a_0}{s^2 + b_1 s + b_0} \\ &= -\left\{ \frac{R_o s^2 + (\frac{R_o}{R_D C_D} + \frac{R_o}{R_K C_K} + \frac{1}{C_D} + \frac{1}{C_K}) s + \frac{R_o + R_D + R_K}{R_D C_D R_K C_K}}{s^2 + (\frac{1}{R_D C_D} + \frac{1}{R_K C_K}) s + \frac{1}{R_D C_D R_K C_K}} \right\} \end{aligned} \tag{6.4}$$

Using bilinear transformation, the transfer function can be discretized as follows:

$$m_1(V_{t,k} - V_{OC}) + m_2(V_{t,k-1} - V_{OC}) + m_3(V_{t,k-2} - V_{OC}) = m_4 I_{B,k} + m_5 I_{B,k-1} + m_6 I_{B,k-2} \tag{6.5}$$

where

$$m_1 = \frac{4}{t^2} + \frac{2}{t}\left(\frac{1}{R_D C_D} + \frac{1}{R_K C_K} \right) + \frac{1}{R_D C_D R_K C_K}$$

$$m_2 = \frac{2}{R_D C_D R_K C_K} - \frac{8}{t^2}$$

$$m_3 = \frac{4}{t^2} - \frac{2}{t}\left(\frac{1}{R_D C_D} + \frac{1}{R_K C_K}\right) + \frac{1}{R_D C_D R_K C_K}$$

$$m_4 = -\left[\frac{4R_o}{t^2} + \frac{2}{t}\left(\frac{R_o}{R_D C_D} + \frac{R_o}{R_K C_K} + \frac{1}{C_D} + \frac{1}{C_K}\right) + \frac{R_o + R_D + R_K}{R_D C_D R_K C_K}\right]$$

$$m_5 = \frac{8}{R_o t^2} - 2\frac{R_o + R_D + R_K}{R_D C_D R_K C_K}$$

$$m_6 = -\frac{4R_o}{t^2} + \frac{2}{t}\left(\frac{R_o}{R_D C_D} + \frac{R_o}{R_K C_K} + \frac{1}{C_D} + \frac{1}{C_K}\right) - \frac{R_o + R_D + R_K}{R_D C_D R_K C_K}$$

Both (6.3) and (6.5) will be used in formulating the objective function of the PSO. The main objective is to determine the unknown parameters to obtain the V_{OC}. Then the SOC can be derived using the V_{OC} vs SOC relationship in Fig. 4.1.

6.2.1 Formulation of objective function

For the proposed method, the main objective is to estimate the battery parameters, V_{OC}, R_o, R_D, τ_D, V_D, R_K, τ_K and V_K , using the measured battery terminal voltage $\tilde{V}_t$ and battery current I_B. Mathematically, the objective function can be formulated as

$$f_{obj} = \left| f_{V_t} \right| + \left| f_{V_{dynamics}} \right| \tag{6.6}$$

where

$$f_{V_t} = 1 - \frac{V_t}{\tilde{V}_t} \tag{6.7}$$

$$f_{V_{dynamics}} = \frac{\begin{bmatrix} m_1(V_{t,k} - V_{OC}) + m_2(V_{t,k-1} - V_{OC}) + \\ m_3(V_{t,k-2} - V_{OC}) \end{bmatrix}}{m_4 I_{B,k} + m_5 I_{B,k-1} + m_6 I_{B,k-2}} + 1 \tag{6.8}$$

The terms in (6.7) and (6.8) are obtained using (6.3) and (6.5) respectively. Both (6.7) and (6.8) are normalized to ensure that their weightages are the same. The objective

function (6.6) is formulated such that the identified battery parameters give accurate battery terminal voltage and dynamics. The first term in (6.6) is used to ensure that the identified parameters give an accurate terminal voltage while the second term describes the dynamic response error.

6.2.2 Inverse barrier constraint

To ensure that the estimated parameters are positive values, an inverse barrier f_b is added to the objective function (6.6) such that $f_{obj} = \left| f_{V_t} \right| + \left| f_{V_{dynamics}} \right| + \left| f_b \right|$. The inverse barrier constraint is formulated as follows:

$$f_b = \mu \sum_{i=1}^{8} \alpha_{x_i} \left[f_{barrier,x_i} \right] \tag{6.9}$$

where

$$f_{barrier,x} = \frac{1}{x_{i,\max} - x_i} + \frac{1}{x_i - x_{i,\min}}$$

$$\alpha_{x_i} = \frac{x_{\mathrm{i,max}} - x_{\mathrm{i,min}}}{4}$$

$$x_i \in \left[V_{OC} \quad R_o \quad R_D \quad \tau_D \quad V_D \quad R_K \quad \tau_K \quad V_K \right].$$

The inverse barrier ensures that the objective function will tend to infinity when it is close to the boundary. As the range of the unknown parameters x_i is different, the α_x is included to ensure that the inverse barrier functions are within the same weightage range for different parameters. The α_{x_i} of each parameter is obtained by finding the minimum point of the barrier function ($f_{barrier,x}$) in (6.9). From (6.9), the $f_{barrier,x}$ of the current particle x_p is

$$f_{barrier,x} = \frac{1}{\left(x_{\max} - x_p \right)} + \frac{1}{\left(x_p - x_{\min} \right)} \tag{6.10}$$

By taking the derivative of (6.10) and equating to zero, the minimum value of the current particle is obtained.

$$\frac{d}{dx} f_{barrier,x} = \frac{1}{\left(x_{\max} - x_p\right)^2} - \frac{1}{\left(x_p - x_{\min}\right)^2} = 0$$
$$x_p = \frac{x_{\max} + x_{\min}}{2} \tag{6.11}$$

From (6.11), the minimum value occurs when x_p is equal to the average value of maximum and minimum constraints. By substituting (6.11) into (6.10), the minimum value of barrier function can be obtained.

$$f_{barrier,x} = \frac{1}{\left(x_{\max} - \frac{x_{\max} + x_{\min}}{2}\right)^2} + \frac{1}{\left(\frac{x_{\max} + x_{\min}}{2} - x_{\min}\right)^2}$$
$$= \frac{4}{x_{\max} - x_{\min}} \tag{6.12}$$

From (6.12), the $f_{barrier,x}$ is set to unity by letting $\alpha_x = \frac{x_{\max} - x_{\min}}{4}$.

The constraint used in the inverse barrier f_b is given by

$$\text{Constraint} = \begin{cases} V_{OC_{\min}} < V_{OC} < V_{OC_{\max}} \\ 0.001\Omega < R_o < 0.1\Omega \\ 0.001\Omega < R_D < 0.05\Omega \\ 1s < \tau_D < 10s \\ 0.001V < V_D < 0.1V \\ 0.001\Omega < R_K < 0.05\Omega \\ 10\,\text{s} < \tau_K < 50\,\text{s} \\ 0.001V < V_K < 0.1V \end{cases}$$

For the constraint of battery parameters (R_o, R_D, τ_D, V_D, R_K, τ_K and V_K), the historical parameter range of lithium-ion chemistries [176] is used. In general, the total internal resistance of the battery ranges from 50 to 100 mΩ and the 60% increase of battery

maximum resistance compared to its initial value is reported to be an indication of the battery's end of life [12, 176]. Thus, the battery maximum parameters values can be assumed to be 160% of its initial value. For the search space of V_{OC}, it is updated using the measured battery terminal voltage during the charging and discharging process. The search range is defined as

If $I_B > 0$ (discharging)

$$V_{\mathrm{OC}_{\min}} = V_t + I_B \times (R_{o_{\min}} + R_{D_{\min}} + R_{K_{\min}})$$

$$V_{\mathrm{OC}_{\max}} = V_t + I_B \times (R_{o_{\max}} + R_{D_{\max}} + R_{K_{\max}})$$

If $I_B < 0$ (charging)

$$V_{\mathrm{OC}_{\min}} = V_t + I_B \times (R_{o_{\max}} + R_{D_{\max}} + R_{K_{\max}})$$

$$V_{\mathrm{OC}_{\max}} = V_t + I_B \times (R_{o_{\min}} + R_{D_{\min}} + R_{K_{\min}})$$

The constraint parameter μ is used in (6.9) as the overall weightage of the inverse barrier. By adding the constraint, the problem now becomes an unconstraint optimization problem which can be solved using PSO discussed in the next section.

6.2.3 The PSO algorithm

The PSO algorithm is a stochastic method that begins with the initialization of a population with random solutions. These random solutions will be substituted into the cost function to search for the best fitness solution known as *pbest*. In addition, the global best fitness solution known as *gbest* is also stored in the optimizer. The velocity for the particles is given as [186]

$$v_{ij}[k+1] = \omega v_{ij}[k] + c_1\lambda_1(x_{pbest,ij} - x_{ij}[\mathrm{k}]) + c_2\lambda_2(x_{gbest,i} - x_{ij}[\mathrm{k}]) \qquad (6.13)$$

where λ_1 and λ_2 represent uniform distributed random numbers, c_1 and c_2 are acceleration constants. The inertia weight ω is given by $\omega = \omega_{\max} - \frac{\omega_{\max} - \omega_{\min}}{k_{\max}} \times k$ with k as the

generation index and k_{max} as the maximum number of generations. In each iteration, the optimizer changes the velocity of the population so that it will converge towards *pbest* and *gbest*. The iteration will terminate when the desired *gbest* value is met or the maximum number of generation is reached. The proposed algorithm is summarized in Table 6-1.

Table 6-1. Pseudo code of PSO with inverse barrier constraint method

Step 1: Initialization
Load V_t and I_B from the experiment.
i=0; index of parameters evaluated.
k=0; generation index.
Randomly generate:
A population of N particles, $x_{ij}[k] = \left[V_{OC} \quad R_o \quad R_D \quad \tau_D \quad V_D \quad R_K \quad \tau_K \quad V_K\right]^T$
An initial set of velocities, $\mathbf{v}_{ij}[k]$;
Let $pbest_{ij} = gbest$ during initialization. (j = 1,2,…..,N)

Step 2: Update *pbest* and *gbest*.
for j=*0;p<N;j++*
Calculate f_{obj} (6.6) using, (6.7), (6.8) and (6.9);
if($f_{obj}(j) < f_{obj}(pbest_{ij})$) $pbest_{ij} = f_{obj}(j)$
end
$gbest_i$ = min($pbest_{ij}$);

Step 3: Update velocities using (6.13).
$v_{ij}[k+1] = \omega v_{ij}[k] + c_1\lambda_1(x_{pbest,ij} - x_{ij}[k]) + c_2\lambda_2(x_{gbest,i} - x_{ij}[k])$
where λ_1 and λ_2 are random numbers uniformly distributed; The constant c_1 and c_2 are also known as the acceleration constants.
The inertia weight $\omega = \omega_{max} - \frac{\omega_{max} - \omega_{min}}{k_{max}} \times k$
where k_{max} is the maximum number of iteration.

Step 4: Check for stopping criterion.
The stopping criterion is defined as:
$gbest_i < 0.001$
Update generation index k and go to Step 2 if stopping criterion is not met. After this step, a set of optimized parameter $x_{gbest,i}$ is obtained.

6.3 Experimental Evaluation

To validate the performance of the proposed method, various experiments have been conducted using the same experimental setup as in Fig. 3.14 to perform the vision

system payload operation of VELOX-I nanosatellite. The same lithium-ion cell in chapter 3 with a total capacity of 2.9Ah is used in the experiment. In order to prolong the battery lifespan, the battery's depth of discharge is recommended to be less than 25% [40]. Fig. 6.1 shows the battery current profile of the experiment. The positive current spike represents the operation of the vision payload system in VELOX-I.

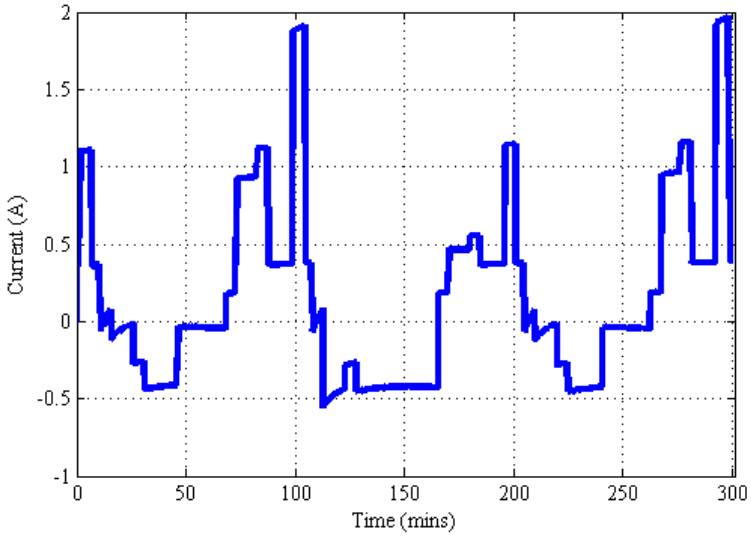

Fig. 6.1 VELOX-I vision mission load profile

The parameters that affect the performance of PSO are the population size (*ps*), the acceleration constants c_1 and c_2 and the barrier parameter μ. The acceleration constants are set at 2 to ensure that the particles would go beyond the target in half time [186]. For the selection of population size *ps*, 5 different population sizes (20, 40, 60, 80 and 100) are used to perform the PSO algorithm for the first 30 data points of Fig. 6.1. For each data point, a maximum generation of 1000 is performed and it is repeated 50 times to average the optimized results. Fig. 6.2 shows the averaged optimized result of the different population sizes. For all the population size, the solution converges at each data point. However, the best fit value is varying at each data point as the objective function is calculated based on varying V_t and I_B measurements. For the experimental

evaluation, a population size of 50 is used after considering the computation load of the PSO when performing the optimization.

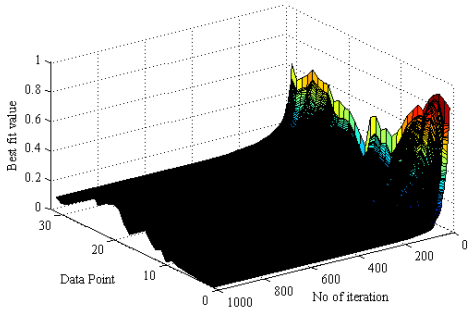

(i) *ps* = 20

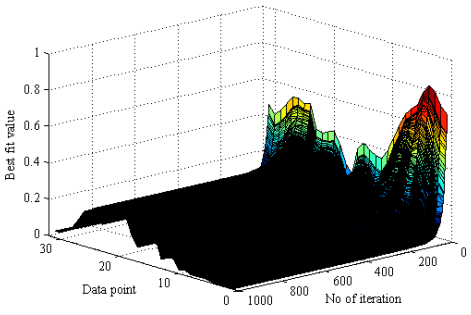

(ii) *ps* =40

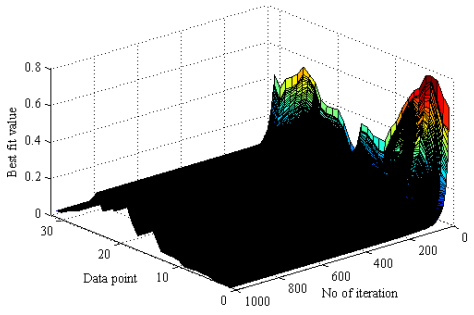

(iii) *ps* = 60

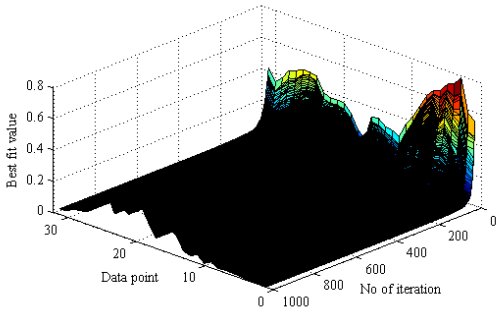

(iv) *ps* =80

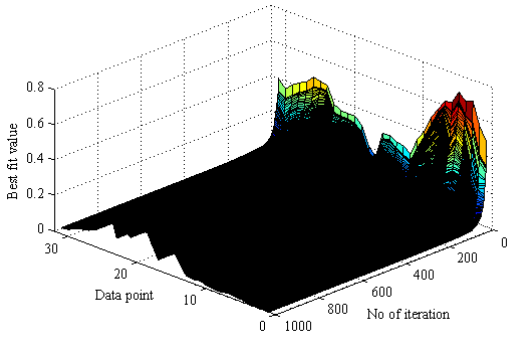

(v) *ps* =100

Fig. 6.2 Population size studies using the best fit value

Fig. 6.3 shows the effects of different barrier parameter values towards the best fit value for the same 30 data points with the population size of 50. The best fit value remains constant once it falls below the value 1e-3. As a result, 1e-4 is used as the barrier parameter in the experiment.

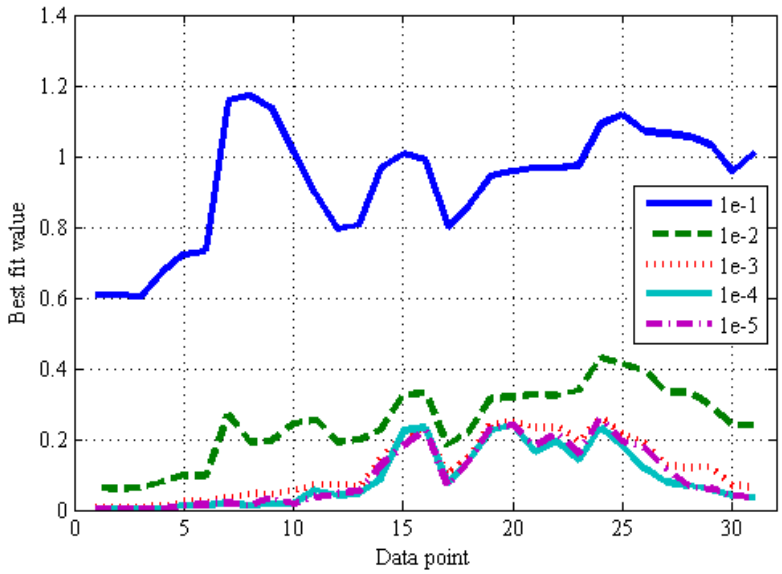

Fig. 6.3 Selection of barrier parameter studies

Based on the results in Figs. 6.2 and 6.3, the following PSO parameters are used in the proposed method for the experiment:

(1) Population size: N = 50

(2) Maximum iteration: k_{max} = 300

(3) Members of particle: V_{OC}, R_o, R_D, τ_D, V_D, R_K, τ_K and V_K

(4) Inertia weight factors: ω_{max} =0.9 and ω_{min}=0.4

(5) Acceleration constants: c_1=c_2=2

(6) Barrier parameter: μ= 0.0001

(7) Stopping criterion: *gbest* = 0.001

Fig. 6.4 shows the SOC estimation for the proposed method, DUKFST, UKFST and EKF. It is observed that PSO and DUKFST performed better than UKFST and EKF.

Fig. 6.5 presents the absolute estimation error of each method. The result is summarized in Table 6-2. From the result, the PSO performed better than EKF with lower error for both RMSE and absolute maximum error. It has a lower RMSE than UKFST but its absolute maximum error is higher. Its performance is similar to DUKFST with a higher absolute maximum error.

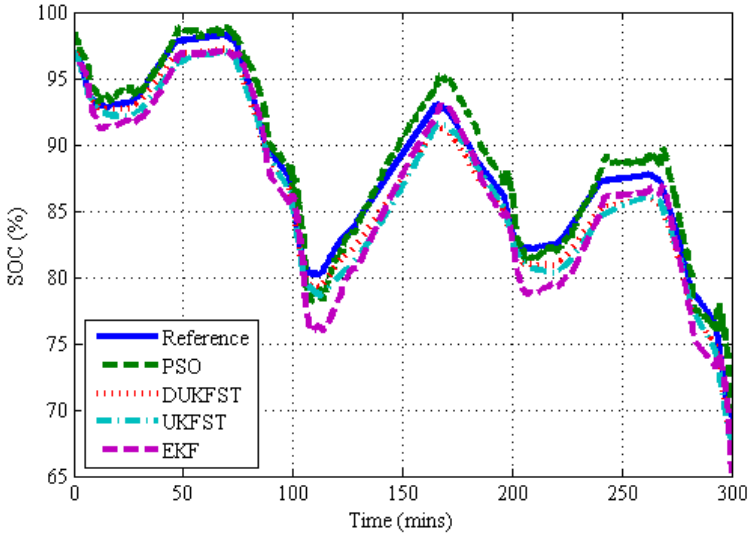

Fig. 6.4 SOC estimation comparison

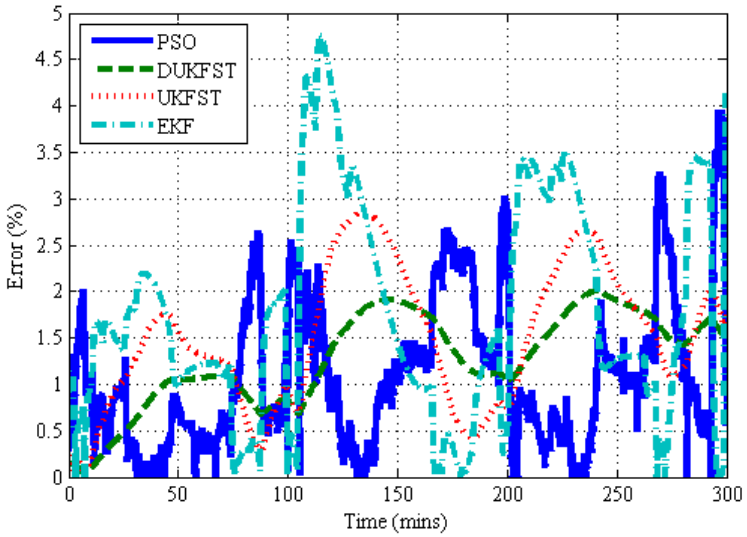

Fig. 6.5 SOC estimation error comparison

Table 6-2 Performance comparison between proposed method, DUKFST, UKFST and EKF

	PSO	*DUKFST*	*UKFST*	*EKF*
Mean	1.10%	1.27%	1.49%	1.81%
RMSE	1.36%	1.37%	1.67%	2.16%
Maximum Error	4.01%	2.01%	2.85%	5.09%

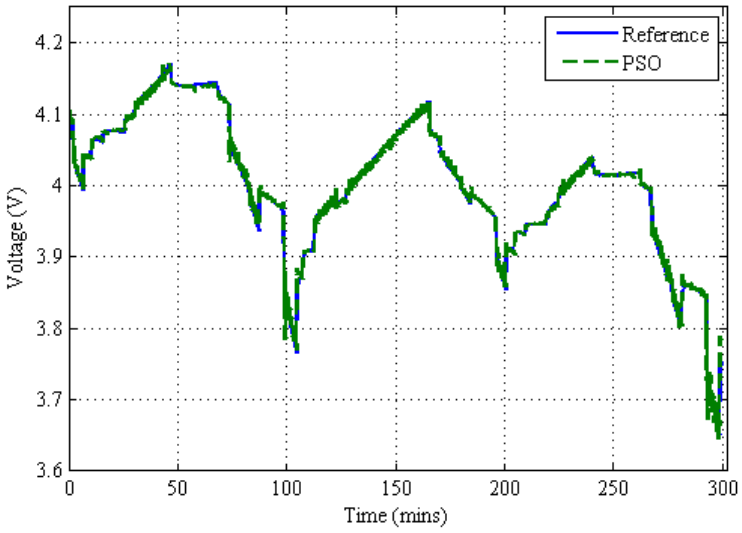

Fig. 6.6 V_t estimation comparison

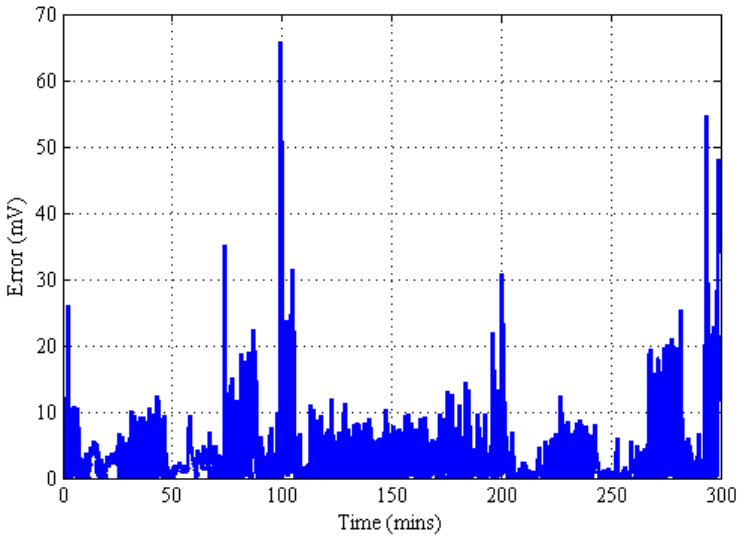

Fig. 6.7 V_t estimation error comparison

The battery terminal voltage V_t estimation error is used to validate the identified battery parameters. Figs. 6.6 and 6.7 compare the estimated battery voltage using the proposed method and its estimation error respectively. It shows that the proposed

method is able to estimate the voltage accurately. The average estimation error is below 20 mV. The spike of 60mV occurs whenever the battery discharge current is changed.

6.4 Summary

In this chapter, a particle swarm optimization (PSO) with inverse barrier constraint for SOC estimation is proposed. It overcomes the shortcomings of the need to linearize the battery model of EKF method. It also does not require any information on measurement and process noise which affect the performance of all of Kalman filter based method. From the experimental results, the RMSE and absolute maximum error based on the proposed method are 1.37% and 4.01% respectively, which is 59% and 27% in improvement than the EKF. It has a lower RMSE error than the UFKST and is comparable with DUKFST.

CHAPTER 7

7. CONCLUSION AND FUTURE WORKS

7.1 Conclusion

In this thesis, four different SOC estimation methods that suit the satellite application needs have been progressively proposed and developed. Firstly, the SOC estimation using ampere-hour counting with impulse response reset has been developed. The method takes advantage of the turning on/off of satellite subsystems instead of artificially injecting current pulses to extract the battery's impulse response. It does not require any additional circuit to perform the pulse. The performance has been compared against a precise ampere-hour meter. From the comparison, the proposed approach has a maximum error of 5.14% and a mean error of 1.83%. However, it still requires the impulse response from the load change to reset it. Moreover, the impulse responses need to be stored in the look-up table and they are also affected by the ageing and battery operation temperature.

The second state-of-charge (SOC) estimation method is based on a square root spherical unscented Kalman filter (Sqrt-UKFST). It improves the shortfalls of the first method and extended Kalman filter (EKF). It takes advantage of Jacobian-free linearization approach with unscented Kalman filter (UKF). Its spherical transform with a hyper unit sphere requires fewer sigma points than the standard UKF and this leads to a reduced computational requirement. The numerical properties in state covariance is also improved by the square root characteristic. From the experimental results, the root-mean-square errors (RMSE) of EKF, ampere-hour counting and fuel gauge are approximately 37%, 900% and 171% higher than the proposed Sqrt-UKFST

respectively. The parameter variation study also shows that the proposed Sqrt-UKFST is more robust than EKF and the regular UKF requires 32% more multiplication than Sqrt-UKFST. Although it improves the shortfall of the opportunistic SOC estimation method, the temperature factor is not considered.

The third method uses a dual square root unscented Kalman filter (DUKFST) with unit spherical unscented transform. It is developed to overcome the lack of temperature consideration in the Sqrt-UKFST. The experimental results demonstrate that the proposed DUKFST outperforms the Sqrt-UKFST and EKF with the lowest RMSE and the lowest maximum errors across different temperatures. The improvement is particularly significant at 0°C and 50°C. This improvement in performance is at the expense of increased computational requirement.

Lastly, a particle swarm optimization with inverse barrier constraint for SOC estimation is developed to overcome the shortcomings of the need to linearize the battery model which is the major drawback for EKF method. Moreover, it does not require any information on measurement and process noise which can affect all the Kalman filter based method's performance. From the experimental results, the RMSE and absolute maximum error of the PSO method are 1.37% and 4.01% respectively, which is 59% and 27% in improvement when compared against EKF. It has lower RMSE error than the Sqrt-UFKST and is comparable with DUKFST. Table 7-1 summarizes the strength and the weakness of each proposed method.

Table 7-1. Summary of proposed methods

Proposed Method	Strength	Weakness
Opportunistic	Performed better than Coulomb counting. It is able to reset across all SOC levels. Takes advantage of the satellite load profile. Computation is the simplest among the proposed methods.	Temperature factor is not considered. Needs to store the impulse response. The responses are affected by ageing and temperature. It still requires load change to reset it.
Sqrt-UKFST	Dynamic and closed-loop estimation. Online and can provide dynamic estimation error range. It is more robust to the parameter variation than extended Kalman filter. It is more computational efficient than the traditional unscented transform.	Higher computational cost than opportunistic. Temperature factor is not considered. Kalman filter is still affected by the noise covariance.
DUKFST	Temperature factor is included. Battery parameter and noise covariance update are performed.	More computationally expensive than Sqrt-DUKFST. The DUKFST is still dependent on noise covariance factor.
PSO with an inverse barrier constraint	It does not require noise covariance value and parameter identification is not required. Performance is comparable to DUKFST.	Most computationally expensive method.

7.2 Future Works

The following suggestions should be explored further for the future works.

In this thesis, only state-of-charge estimation is performed for satellite power management system. It is also beneficial to include the state-of-health estimation for the satellite. This can provide more details of battery information such as power fade due to

the increase in battery parameters and battery run time. Moreover, majority of estimated SOC are expressed in terms of battery nominal or maximum rated capacity. Since battery rated capacity is affected by temperature and it deteriorates over the long run, its maximum available capacity estimation should be incorporated into state-of-charge estimation.

Various lithium-ion chemistries such as lithium-ion phosphate and lithium-manganese oxide exhibit different cell behaviours. A generalized model to represent all different cell chemistries should be investigated. The generalized model should include hysteresis effect as there is a lack of hysteresis modelling in lithium-ion batteries. The hysteresis effect is quite significant in lithium phosphate chemistries where the battery open-circuit voltage has a very flat curve against its state-of-charge. This model should combine the electrochemical and equivalent circuit. Most of the battery management systems employ heater to maintain the battery operation temperature. The ways to use both the load profile and the electrochemical model to maintain the operation temperature instead of a heater should be explored.

Batteries are usually connected in multiple packs together with power electronics converter. The optimum charging of the battery and the cell equalization/balancing using the state-of-charge and the state-of-health should be investigated. The cell balancing is another important issue in battery packs where one damaged cell can be extremely dangerous to the whole battery packs. Lastly, an integrated battery management system with cell equalization, state-of-charge, state-of-health and optimal charging should be developed for a satellite in order to optimize battery usage.

LIST OF PUBLICATIONS

- **H. Aung** and K. S. Low, "Opportunistic state of charge (SOC) estimation for a Nanosatellite," in *Proc. Int. Symp. on Space Technology and Sci., JSASS*, Jun. 2013.
- **H. Aung** and K. S. Low, "Modeling and State of Charge Estimation of a Lithium Ion Battery Using Unscented Kalman Filter in a Nanosatellite," in *Proc.The 9th IEEE Conf. on Ind. Electron. and Applicat.*, Jun. 2014, pp. 1422-1426.
- **H. Aung**, K. S. Low, and S. T. Goh, "State-of-Charge Estimation of Lithium-ion Battery Using Square Root Spherical Unscented Kalman Filter (Sqrt-UKFST) in Nanosatellite," *Power Electronics, IEEE Transactions on*, vol. PP, pp. 1-1, 2014.
- **H. Aung**, and K. S. Low, "Temperature Dependent State-of-charge Estimation of Lithium Ion Battery Using Dual Spherical Unscented Kalman Filter," *IET Power Electron., vol. 8, pp. 2026-2033, 2015.*
- **H. Aung**, K. S. Low, and J. J. Soon, "State-of-Charge Estimation Using Particle Swarm Optimization with Inverse Barrier Constraint for Satellite's Battery," in *Proc.The 10th IEEE Conf. on Ind. Electron. and Applicat.*, Jun. 2015.
- **H. Aung**, J. J. Soon and K. S. Low, "Real Time State-of-charge Estimation of Lithium Ion Batteries Using Particle Swarm Optimization (PSO)," To be submitted to *IEEE Power Electronics.*

BIBLIOGRAPHY

[1] K. Woellert, P. Ehrenfreund, A. J. Ricco, and H. Hertzfeld, "Cubesats: Cost-effective science and technology platforms for emerging and developing nations," *Advances in Space Research,* vol. 47, pp. 663-684, Feb. 2011.

[2] J. Bouwmeester and J. Guo, "Survey of worldwide pico- and nanosatellite missions, distributions and subsystem technology," *Acta Astronautica,* vol. 67, pp. 854-862, Oct. 2010.

[3] S. Nakasuka, N. Sako, H. Sahara, Y. Nakamura, T. Eishima, and M. Komatsu, "Evolution from education to practical use in University of Tokyo's nano-satellite activities," *Acta Astronautica,* vol. 66, pp. 1099-1105, Apr. 2010.

[4] H. Heidt, J. Puig-Suari, A. Moore, S. Nakasuka, and R. Twiggs, "CubeSat: A new generation of picosatellite for education and industry low-cost space experimentation," 2000.

[5] D. Selva and D. Krejci, "A survey and assessment of the capabilities of Cubesats for Earth observation," *Acta Astronautica,* vol. 74, pp. 50-68, May. 2012.

[6] F. Santoni, F. Piergentili, S. Donati, M. Perelli, A. Negri, and M. Marino, "An innovative deployable solar panel system for Cubesats," *Acta Astronautica,* vol. 95, pp. 210-217, Feb. 2014.

[7] A. Ali, M. R. Mughal, H. Ali, and L. Reyneri, "Innovative power management, attitude determination and control tile for CubeSat standard NanoSatellites," *Acta Astronautica,* vol. 96, pp. 116-127, Mar. 2014.

[8] B. Scrosati and J. Garche, "Lithium batteries: Status, prospects and future," *J. Power Sources,* vol. 195, pp. 2419-2430, May. 2010.

[9] A. Väyrynen and J. Salminen, "Lithium ion battery production," *The Journal of Chemical Thermodynamics,* vol. 46, pp. 80-85, Mar. 2012.

[10] J. Li, J. Klee Barillas, C. Guenther, and M. A. Danzer, "A comparative study of state of charge estimation algorithms for LiFePO4 batteries used in electric vehicles," *J. Power Sources,* vol. 230, pp. 244-250, May. 2013.

[11] M. U. Cuma and T. Koroglu, "A comprehensive review on estimation strategies used in hybrid and battery electric vehicles," *Renewable and Sustainable Energy Reviews,* vol. 42, pp. 517-531, Feb. 2015.

[12] W. Waag, C. Fleischer, and D. U. Sauer, "Critical review of the methods for monitoring of lithium-ion batteries in electric and hybrid vehicles," *J. Power Sources,* vol. 258, pp. 321-339, Mar. 2014.

[13] S. Piller, M. Perrin, and A. Jossen, "Methods for state-of-charge determination and their applications," *J. Power Sources,* vol. 96, pp. 113-120, Jun. 2001.

[14] F. Huet, "A review of impedance measurements for determination of the state-of-charge or state-of-health of secondary batteries," *J. Power Sources,* vol. 70, pp. 59-69, Jan. 1998.

[15] D. Andre, C. Appel, T. Soczka-Guth, and D. U. Sauer, "Advanced mathematical methods of SOC and SOH estimation for lithium-ion batteries," *J. Power Sources,* vol. 224, pp. 20-27, Feb. 2013.

[16] L. Lu, X. Han, J. Li, J. Hua, and M. Ouyang, "A review on the key issues for lithium-ion battery management in electric vehicles," *J. Power Sources,* vol. 226, pp. 272-288, 3/15/ Mar. 2013.

[17] H. Rahimi-Eichi, U. Ojha, F. Baronti, and M. Chow, "Battery Management System: An Overview of Its Application in the Smart Grid and Electric Vehicles," *IEEE Ind. Electron. Mag.,* vol. 7, pp. 4-16, Jun. 2013.

[18] B. Pattipati, C. Sankavaram, and K. R. Pattipati, "System identification and estimation framework for pivotal automotive battery management system characteristics," *IEEE Trans. Syst. Man, Cybern. B, Cybern.,* vol. 41, pp. 869-884, Nov. 2011.

[19] V. Pop, H. J. Bergveld, D. Danilov, P. P. L. Regtien, and P. H. L. Notten, *Battery Management Systems: Accurate State-of-Charge Indication for Battery-Powered Applications*. London: Springer Verlag, 2008.

[20] K. W. E. Cheng, B. P. Divakar, H. Wu, K. Ding, and H. F. Ho, "Battery-management system (BMS) and SOC development for electrical vehicles," *IEEE Trans. Veh. Technol.,* vol. 60, pp. 76-88, Jan. 2011.

[21] A. A. H. Hussein and I. Batarseh, "A review of charging algorithms for nickel and lithium battery chargers," *IEEE Trans. Veh. Technol.,* vol. 60, pp. 830-838, Mar. 2011.

[22] I. H. Li, W. Y. Wang, S. F. Su, and Y. S. Lee, "A merged fuzzy neural network and its applications in battery state-of-charge estimation," *IEEE Trans. Energy Convers.,* vol. 22, pp. 697-708, Sept. 2007.

[23] T. R. Crompton, *Battery reference book*: Oxford : Newnes, 3rd ed., 2000.

[24] R. A. Huggins, *Advanced Batteries: Materials Science Aspects*: Boston, MA : Springer US., 2009.

[25] C. Vincent and B. Scrosati, *Modern Batteries 2nd Edition*: Elsevier, 1997.

[26] G. Pistoia, *Batteries for portable devices*: Amsterdam ; New York : Elsevier, 1st ed., 2005.

[27] D. Linden and T. B. Reddy, *Handbook of batteries*: New York: McGraw-Hill, 2002.

[28] R. M. Dell and D. A. J. Rand, *Understanding batteries*: Cambridge : Royal Society of Chemistry., 2001.

[29] A. R. Jha, *Next-generation batteries and fuel cells for commercial, military, and space applications*: Boca Raton, Fla. : CRC Press., 2012.

[30] B. Scrosati, K. M. Abraham, W. A. v. Schalkwijk, and J. Hassoun, *Lithium batteries : advanced technologies and applications*: Hoboken, New Jersey : John Wiley & Sons, Inc., 2013.

[31] A. Thaler and D. Watzenig, *Automotive Battery Technology*: Cham : Springer International Publishing : Imprint: Springer, 2014.

[32] R. J. Brodd, *Batteries for Sustainability: Selected Entries from the Encyclopedia of Sustainability Science and Technology*: New York, NY : Springer New York : Imprint: Springer, 2013.

[33] S. Dhameja, *Electric vehicle battery systems*: Boston : Newnes., 2002.

[34] H. A. Kiehne, *Battery technology handbook*: New York : Marcel Dekker, 2nd ed., 2003.

[35] K. E. Aifantis, S. A. Hackney, and R. V. Kumar, *High energy density lithium batteries : materials, engineering, applications*: Weinheim : Wiley-VCH., 2010.

[36] B. Diouf and R. Pode, "Potential of lithium-ion batteries in renewable energy," *Renewable Energy,* vol. 76, pp. 375-380, Apr. 2015.

[37] A. I. Stan, M. Swierczynski, D. I. Stroe, R. Teodorescu, and S. J. Andreasen, "Lithium ion battery chemistries from renewable energy storage to automotive and back-up power applications - An overview," in *Proc. Int. Conf. Optimization of Elect. and Electron. Equipment (OPTIM)*, May. 2014, pp. 713-720.

[38] X. Yuan, H. Liu, and J. Zhang, *Lithium-ion batteries : advanced materials and technologies*: Boca Raton, FL : CRC Press, c2012., 2012.

[39] J.-K. Park, *Principles and applications of lithium secondary batteries*: Weinheim : Wiley-VCH., 2012.

[40] C. D. Rahn and C.-Y. Wang, *Battery systems engineering* Hoboken : John Wiley & Sons Inc., 2013.

[41] C. Daniel and J. O. Besenhard, *Handbook of battery materials*: Weinheim : Wiley-VCH Verlag, 2011.

[42] T. B. Reddy and D. Linden, *Linden's handbook of batteries*: New York : McGraw-Hill. 4th ed., 2011.

[43] M. Coleman, C. K. Lee, C. Zhu, and W. G. Hurley, "State-of-charge determination from EMF voltage estimation: using impedance, terminal voltage, and current for lead-acid and lithium-ion batteries," *IEEE Trans. Ind. Electron.*, vol. 54, pp. 2550-2557, Oct. 2007.

[44] E. Prada, D. Di Domenico, Y. Creff, J. Bernard, and V. Sauvant-Moynot, "A coupled OD electrochemical ageing & electro-thermal Li-ion modeling approach for HEV/PHEV," in *Proc. IEEE Veh. Power and Propulsion Conf. (VPPC)*, Sept. 2011, pp. 1-8.

[45] M. W. Verbrugge and R. S. Conell, "Electrochemical and Thermal Characterization of Battery Modules Commensurate with Electric Vehicle Integration," *J. Electrochemical Soc.*, vol. 149, pp. A45-A53, Jan. 2002.

[46] A. Seaman, T.-S. Dao, and J. McPhee, "A survey of mathematics-based equivalent-circuit and electrochemical battery models for hybrid and electric vehicle simulation," *J. Power Sources*, vol. 256, pp. 410-423, Feb. 2014.

[47] R. G. Compton and C. E. Banks, *Understanding voltammetry*: London : Imperial College Press. 2nd ed., 2011.

[48] H. Bode, *Lead-acid batteries*: Wiley and Sons., 1977.

[49] B. Wu, M. Mohammed, D. Brigham, R. Elder, and R. E. White, "A non-isothermal model of a nickel–metal hydride cell," *J. Power Sources*, vol. 101, pp. 149-157, Oct. 2001.

[50] T.-S. Dao and J. McPhee, "Dynamic modeling of electrochemical systems using linear graph theory," *J. Power Sources*, vol. 196, pp. 10442-10454, Dec. 2011.

[51] J. Newman and W. Tiedemann, "Porous-electrode theory with battery applications," *AIChE J.*, vol. 21, pp. 25-41, Jan. 1975.

[52] M. Doyle, T. F. Fuller, and J. Newman, "Modeling of Galvanostatic Charge and Discharge of the Lithium/Polymer/Insertion Cell," *J. The Electrochemical Society*, vol. 140, pp. 1526-1533, Jun. 1993.

[53] M. Doyle, J. Newman, A. S. Gozdz, C. N. Schmutz, and J. M. Tarascon, "Comparison of Modeling Predictions with Experimental Data from Plastic Lithium Ion Cells," *J. The Electrochemical Society*, vol. 143, pp. 1890-1903, Jun. 1996.

[54] C. M. Doyle, "Design and simulation of lithium rechargeable batteries," *Lawrence Berkeley National Laboratory*, 2010.

[55] J. Newman and K. E. Thomas-Alyea, *Electrochemical systems*: John Wiley & Sons, 2012.

[56] V. Ramadesigan, V. Boovaragavan, J. C. Pirkle, and V. R. Subramanian, "Efficient Reformulation of Solid-Phase Diffusion in Physics-Based Lithium-Ion Battery Models," *J. The Electrochemical Society*, vol. 157, pp. A854-A860, May. 2010.

[57] V. Ramadesigan, K. Chen, N. A. Burns, V. Boovaragavan, R. D. Braatz, and V. R. Subramanian, "Parameter Estimation and Capacity Fade Analysis of Lithium-Ion Batteries Using Reformulated Models," *J. The Electrochemical Society*, vol. 158, pp. A1048-A1054, Jul. 2011.

[58] H. L. Chan, "A new battery model for use with battery energy storage systems and electric vehicles power systems," in *Proc. IEEE Power Engineering Soc. Winter Meeting.*, Jan. 2000, pp. 470-475 vol.1.

[59] H. Yao-Ching, L. Tin-Da, C. Ruei-Ji, and L. Hong-Yu, "Electric circuit modelling for lithium-ion batteries by intermittent discharging," *IET Power Electron.*, vol. 7, pp. 2672-2677, Oct. 2014.

[60] M. Einhorn, F. V. Conte, C. Kral, and J. Fleig, "A method for online capacity estimation of lithium ion battery cells using the state of charge and the transferred charge," *IEEE Trans. Ind. Appl.*, vol. 48, pp. 736-741, Mar. 2012.

[61] N. Lohmann, P. Weßkamp, P. Haußmann, J. Melbert, and T. Musch, "Electrochemical impedance spectroscopy for lithium-ion cells: Test equipment and procedures for aging and fast characterization in time and frequency domain," *J. Power Sources*, vol. 273, pp. 613-623, Jan. 2015.

[62] E. Samadani, S. Farhad, W. Scott, M. Mastali, L. E. Gimenez, M. Fowler, *et al.*, "Empirical Modeling of Lithium-ion Batteries Based on Electrochemical Impedance Spectroscopy Tests," *Electrochimica Acta,* vol. 160, pp. 169-177, Apr. 2015.

[63] R. Rao, S. Vrudhula, and D. N. Rakhmatov, "Battery modeling for energy aware system design," *Computer,* vol. 36, pp. 77-87, Dec. 2003.

[64] W. Wang, H. Shu-Hung Chung, and J. Zhang, "Near-Real-Time Parameter Estimation of an Electrical Battery Model With Multiple Time Constants and SOC-Dependent Capacitance," *IEEE Trans. Power Electron.,* vol. 29, pp. 5905-5920, Nov. 2014.

[65] M. Einhorn, F. V. Conte, C. Kral, and J. Fleig, "Comparison, Selection, and Parameterization of Electrical Battery Models for Automotive Applications," *IEEE Trans. Power Electron.,* vol. 28, pp. 1429-1437, Mar. 2013.

[66] M. Chen and G. A. Rincon-Mora, "Accurate electrical battery model capable of predicting runtime and I-V performance," *IEEE Trans. Energy Convers.,* vol. 21, pp. 504-511, Jun. 2006.

[67] M. Gholizadeh and F. R. Salmasi, "Estimation of State of Charge, Unknown Nonlinearities, and State of Health of a Lithium-Ion Battery Based on a Comprehensive Unobservable Model," *IEEE Trans. Ind. Electron.,* vol. 61, pp. 1335-1344, Mar. 2014.

[68] R. L. Fares and M. E. Webber, "Combining a dynamic battery model with high-resolution smart grid data to assess microgrid islanding lifetime," *Appl. Energy,* vol. 137, pp. 482-489, Jan. 2015.

[69] S. M. Rezvanizaniani, Z. Liu, Y. Chen, and J. Lee, "Review and recent advances in battery health monitoring and prognostics technologies for electric vehicle (EV) safety and mobility," *J. Power Sources,* vol. 256, pp. 110-124, Jun. 2014.

[70] K. S. Ng, C.-S. Moo, Y.-P. Chen, and Y.-C. Hsieh, "Enhanced coulomb counting method for estimating state-of-charge and state-of-health of lithium-ion batteries," *Appl. Energy,* vol. 86, pp. 1506-1511, Sep. 2009.

[71] K. S. Ng, Y. F. Huang, C. S. Moo, and Y. C. Hsieh, "An enhanced coulomb counting method for estimating state-of-charge and state-of-health of lead-acid batteries," in *Proc. 31st Int. Telecommunications Energy Conf (INTELEC).* Oct. 2009, pp. 1-5.

[72] F. Codeca, S. M. Savaresi, and G. Rizzoni, "On battery state of charge estimation: a new mixed algorithm," in *Proc. IEEE Int Conf on Control Applications.*, Sept. 2008, pp. 102-107.

[73] S. Hoenig, H. Singh, and T. G. Palanisamy, "Method for determining state of charge of a battery by measuring its open circuit voltage," ed: Google Patents, Apr. 2002.

[74] H. J. Bergveld, V. Pop, and P. H. L. Notten, "Apparatus and method for determination of the state-of-charge of a battery when the battery is not in equilibrium," ed: Google Patents, Feb. 2010.

[75] V. Pop, H. J. Bergveld, P. H. L. Notten, J. H. G. Op het Veld, and P. P. L. Regtien, "Accuracy analysis of the State-of-Charge and remaining run-time determination for lithium-ion batteries," *Measurement,* vol. 42, pp. 1131-1138, Oct. 2009.

[76] W. Waag and D. U. Sauer, "Adaptive estimation of the electromotive force of the lithium-ion battery after current interruption for an accurate state-of-charge and capacity determination," *Appl. Energy,* vol. 111, pp. 416-427, Nov. 2013.

[77] C. Chang Yoon, S. Gab-Su, Y. Sung Hyun, and C. Bo-Hyung, "State-of-charge estimation for lithium-ion battery pack using reconstructed open-circuit-voltage curve," in *Proc. Int. Power Electron. Conf. (IPEC)*, May. 2014, pp. 2272-2276.

[78] P. Lei, L. Rengui, and Z. Chunbo, "Relaxation model of the open-circuit voltage for state-of-charge estimation in lithium-ion batteries," *IET Electrical Systems in Transportation.,* vol. 3, pp. 112-117, Nov. 2013.

[79] H. He, X. Zhang, R. Xiong, Y. Xu, and H. Guo, "Online model-based estimation of state-of-charge and open-circuit voltage of lithium-ion batteries in electric vehicles," *Energy,* vol. 39, pp. 310-318, Mar. 2012.

[80] E. D. Tate, M. W. Verbrugge, and S. D. Sarbacker, "State of charge prediction method and apparatus for a battery," ed: Google Patents, Aug. 2002.

[81] M. R. Khan, G. Mulder, and J. Van Mierlo, "An online framework for state of charge determination of battery systems using combined system identification approach," *J. Power Sources,* vol. 246, pp. 629-641, Jan. 2014.

[82] B. S. Bhangu, P. Bentley, D. A. Stone, and C. M. Bingham, "Nonlinear observers for predicting state-of-charge and state-of-health of lead-acid batteries for hybrid-electric vehicles," *IEEE Trans. Veh. Technol.,* vol. 54, pp. 783-794, May. 2005.

[83] H. Dai, X. Wei, Z. Sun, J. Wang, and W. Gu, "Online cell SOC estimation of Li-ion battery packs using a dual time-scale Kalman filtering for EV applications," *Appl. Energy,* vol. 95, pp. 227-237, Jul. 2012.

[84] X. Hu, S. Li, H. Peng, and F. Sun, "Robustness analysis of State-of-Charge estimation methods for two types of Li-ion batteries," *J. Power Sources,* vol. 217, pp. 209-219, Nov. 2012.

[85] C. Hu, B. D. Youn, and J. Chung, "A multiscale framework with extended Kalman filter for lithium-ion battery SOC and capacity estimation," *Appl. Energy,* vol. 92, pp. 694-704, Apr. 2012.

[86] J. Kim and B. H. Cho, "State-of-charge estimation and state-of-health prediction of a li-ion degraded battery based on an EKF combined with a per-unit system," *IEEE Trans. Veh. Technol.,* vol. 60, pp. 4249-4260, Nov. 2011.

[87] M. Mastali, J. Vazquez-Arenas, R. Fraser, M. Fowler, S. Afshar, and M. Stevens, "Battery state of the charge estimation using Kalman filtering," *J. Power Sources,* vol. 239, pp. 294-307, Oct. 2013.

[88] Z. Chen, Y. Fu, and C. C. Mi, "State of charge estimation of lithium-ion batteries in electric drive vehicles using extended Kalman filtering," *IEEE Trans. Veh. Technol.,* vol. 62, pp. 1020-1030, Mar. 2013.

[89] S. Sepasi, R. Ghorbani, and B. Y. Liaw, "A novel on-board state-of-charge estimation method for aged Li-ion batteries based on model adaptive extended Kalman filter," *J. Power Sources,* vol. 245, pp. 337-344, Jan. 2014.

[90] R. Xiong, F. Sun, Z. Chen, and H. He, "A data-driven multi-scale extended Kalman filtering based parameter and state estimation approach of lithium-ion olymer battery in electric vehicles," *Appl. Energy,* vol. 113, pp. 463-476, 1// Jan. 2014.

[91] S. Yuan, H. Wu, and C. Yin, "State of Charge Estimation Using the Extended Kalman Filter for Battery Management Systems Based on the ARX Battery Model," *Energies,* vol. 6, pp. 444-470, Jan. 2013.

[92] F. Sun, X. Hu, Y. Zou, and S. Li, "Adaptive unscented Kalman filtering for state of charge estimation of a lithium-ion battery for electric vehicles," *Energy,* vol. 36, pp. 3531-3540, May. 2011.

[93] Z. He, M. Gao, C. Wang, L. Wang, and Y. Liu, "Adaptive State of Charge Estimation for Li-Ion Batteries Based on an Unscented Kalman Filter with an Enhanced Battery Model," *Energies,* vol. 6, pp. 4134-4151, Aug 2013.

[94] H. Gholizade-Narm and M. Charkhgard, "Lithium-ion battery state of charge estimation based on square-root unscented Kalman filter," *IET Power Electron.,* vol. 6, pp. 1833-1841, Nov 2013.

[95] G. L. Plett, "Sigma-point Kalman filtering for battery management systems of LiPB-based HEV battery packs: Part 1: Introduction and state estimation," *J. Power Sources,* vol. 161, pp. 1356-1368, Oct. 2006.

[96] G. L. Plett, "Sigma-point Kalman filtering for battery management systems of LiPB-based HEV battery packs: Part 2: Simultaneous state and parameter estimation," *J. Power Sources,* vol. 161, pp. 1369-1384, Oct. 2006.

[97] J. Kim, S. Lee, and B. H. Cho, "Complementary cooperation algorithm based on DEKF combined with pattern recognition for SOC/capacity estimation and SOH prediction," *IEEE Trans. Power Electron.,* vol. 27, pp. 436-451, Jan. 2012.

[98] R. Xiong, H. He, F. Sun, and K. Zhao, "Evaluation on state of charge estimation of batteries with adaptive extended Kalman filter by experiment approach," *IEEE Trans. Veh. Technol.,* vol. 62, pp. 108-117, Jan. 2013.

[99] F. Zhang, G. Liu, L. Fang, and H. Wang, "Estimation of battery state of charge with H∞ observer: applied to a robot for inspecting power transmission lines," *IEEE Trans. Ind. Electron.,* vol. 59, pp. 1086-1095, Feb. 2012.

[100] A. Alfi, M. Charkhgard, and M. Haddad Zarif, "Hybrid state of charge estimation for lithium-ion batteries: design and implementation," *IET Power Electron.,* vol. 7, pp. 2758-2764, Nov. 2014.

[101] W.-J. Yang, D.-H. Yu, and Y.-B. Kim, "Parameter estimation of lithium-ion batteries and noise reduction using an H∞ filter," *Journal of Mechanical Science and Technology,* vol. 27, pp. 247-256, Jan. 2013.

[102] G. A. C. L. Castillo and C. M. F. Odulio, "H∞ filter-based online battery state-of-charge estimator for pure electric vehicles," in *Proc. IEEE TENCON Region 10 Conf.,* Nov. 2012, pp. 1-6.

[103] Y. He, X. Liu, C. Zhang, and Z. Chen, "A new model for State-of-Charge (SOC) estimation for high-power Li-ion batteries," *Appl. Energy,* vol. 101, pp. 808-814, Jan. 2013.

[104] J. Yan, G. Xu, H. Qian, and Y. Xu, "Robust State of Charge Estimation for Hybrid Electric Vehicles: Framework and Algorithms," *Energies,* vol. 3, pp. 1654-1672, Sept. 2010.

[105] C. Xiaopeng, S. Weixiang, C. Zhenwei, and A. Kapoor, "A comparative study of observer design techniques for state of charge estimation in electric vehicles," in *Proc. 7th IEEE Conf. Ind. Electron. and Applicat. (ICIEA),* Jul. 2012, pp. 102-107.

[106] X. Hu, F. Sun, and Y. Zou, "Estimation of State of Charge of a Lithium-Ion Battery Pack for Electric Vehicles Using an Adaptive Luenberger Observer," *Energies,* vol. 3, pp. 1586-1603, Sept. 2010.

[107] L. Liu, L. Y. Wang, Z. Chen, C. Wang, F. Lin, and H. Wang, "Integrated system identification and state-of-charge estimation of battery systems," *IEEE Trans. Energy Convers.,* vol. 28, pp. 12-23, Mar. 2013.

[108] Y.-H. Chiang, W.-Y. Sean, and J.-C. Ke, "Online estimation of internal resistance and open-circuit voltage of lithium-ion batteries in electric vehicles," *J. Power Sources,* vol. 196, pp. 3921-3932, Apr. 2011.

[109] M. A. Roscher, O. S. Bohlen, and D. U. Sauer, "Reliable state estimation of multicell lithium-ion battery systems," *IEEE Trans. Energy Convers.,* vol. 26, pp. 737-743, Sept. 2011.

[110] X. Jun, C. C. Mi, C. Binggang, D. Junjun, C. Zheng, and L. Siqi, "The State of Charge Estimation of Lithium-Ion Batteries Based on a Proportional-Integral Observer," *IEEE Trans. Veh. Technol.,* vol. 63, pp. 1614-1621, May. 2014.

[111] H. Chaoui, N. Golbon, I. Hmouz, R. Souissi, and S. Tahar, "Lyapunov-Based Adaptive State of Charge and State of Health Estimation for Lithium-Ion Batteries," *IEEE Trans. Ind. Electron.,* vol. 62, pp. 1610-1618, Mar. 2015.

[112] D. Kim, K. Koo, J. Jeong, T. Goh, and S. Kim, "Second-Order Discrete-Time Sliding Mode Observer for State of Charge Determination Based on a Dynamic Resistance Li-Ion Battery Model," *Energies,* vol. 6, pp. 5538-5551, Oct. 2013.

[113] I.-S. Kim, "The novel state of charge estimation method for lithium battery using sliding mode observer," *J. Power Sources,* vol. 163, pp. 584-590, Dec. 2006.

[114] Z. Fei, L. Guangjun, and F. Lijin, "A battery state of charge estimation method using sliding mode observer," in *Proc. 7th World Congr. on Intelligent Control and Automation (WCICA 2008),* Jun. 2008, pp. 989-994.

[115] X. Chen, W. Shen, Z. Cao, and A. Kapoor, "A novel approach for state of charge estimation based on adaptive switching gain sliding mode observer in electric vehicles," *J. Power Sources*, vol. 246, pp. 667-678, Jan. 2014.

[116] C. Xiaopeng, S. Weixiang, C. Zhenwei, A. Kapoor, and I. Hijazin, "Adaptive gain sliding mode observer for state of charge estimation based on combined battery equivalent circuit model in electric vehicles," in *Proc. 8th IEEE Conf. Ind. Electron. and Applicat. (ICIEA)*, Jun. 2013, pp. 601-606.

[117] I. S. Kim, "Nonlinear State of Charge Estimator for Hybrid Electric Vehicle Battery," *IEEE Trans. Power Electron.*, vol. 23, pp. 2027-2034, Jul. 2008.

[118] W.-Y. Chang, "Estimation of the state of charge for a LFP battery using a hybrid method that combines a RBF neural network, an OLS algorithm and AGA," *Int. J. of Elect. Power & Energy Syst.*, vol. 53, pp. 603-611, Dec. 2013.

[119] L. Yuang-Shung, W. Wei-Yen, and K. Tsung-Yuan, "Soft Computing for Battery State-of-Charge (BSOC) Estimation in Battery String Systems," *IEEE Trans. Ind. Electron.*, vol. 55, pp. 229-239, Jan. 2008.

[120] J. Wei, J. Xuehuan, Z. Jinliang, X. Zhengtao, and J. Yubing, "Comparison of SOC Estimation Performance with Different Training Functions Using Neural Network," in *Proc. UKSim 14th Int. Conf. on Comput. Modelling and Simulation (UKSim)*, Mar. 2012, pp. 459-463.

[121] Y. Shen, "Adaptive online state-of-charge determination based on neuro-controller and neural network," *Energy Conversion and Management*, vol. 51, pp. 1093-1098, May. 2010.

[122] M. Charkhgard and M. Farrokhi, "State-of-charge estimation for lithium-ion batteries using neural networks and EKF," *IEEE Trans. Ind. Electron.*, vol. 57, pp. 4178-4187, Dec. 2010.

[123] M. Shahriari and M. Farrokhi, "Online state-of-health estimation of VRLA batteries using state of charge," *IEEE Trans. Ind. Electron.*, vol. 60, pp. 191-202, Jan. 2013.

[124] L. Xu, J. Wang, and Q. Chen, "Kalman filtering state of charge estimation for battery management system based on a stochastic fuzzy neural network battery model," *Energy Conversion and Manage.*, vol. 53, pp. 33-39, Jan. 2012.

[125] L. Zhitao, W. Youyi, D. Jiani, and C. Can, "RBF network-aided adaptive unscented kalman filter for lithium-ion battery SOC estimation in electric

vehicles," in *Proc. 7th IEEE Conf. on Ind. Electron. and Applicat. (ICIEA).* Jul. 2012, pp. 1673-1677.

[126] H. T. Lin, T. J. Liang, and C. S. M, "Estimation of Battery State of Health Using Probabilistic Neural Network," *IEEE Trans. Ind. Informat.,* vol. 9, pp. 679-685, May. 2013.

[127] L. Kang, X. Zhao, and J. Ma, "A new neural network model for the state-of-charge estimation in the battery degradation process," *Appl. Energy,* vol. 121, pp. 20-27, May. 2014.

[128] K. T. Chau, K. C. Wu, and C. C. Chan, "A new battery capacity indicator for lithium-ion battery powered electric vehicles using adaptive neuro-fuzzy inference system," *Energy Conversion and Management,* vol. 45, pp. 1681-1692, Jul. 2004.

[129] T. Wu, M. Wang, Q. Xiao, and X. Wang, "The SOC estimation of power Li-ion battery based on ANFIS model," *Smart Grid and Renewable Energy,* vol. 3, p. 51, Feb. 2012.

[130] S. G. Li, S. M. Sharkh, F. C. Walsh, and C. N. Zhang, "Energy and Battery Management of a Plug-In Series Hybrid Electric Vehicle Using Fuzzy Logic," *IEEE Trans. Veh. Technol.,* vol. 60, pp. 3571-3585, Oct. 2011.

[131] C. Bo, B. Zhifeng, and C. Binggang, "State of charge estimation based on evolutionary neural network," *Energy Conversion and Manage.,* vol. 49, pp. 2788-2794, Oct. 2008.

[132] J. C. A. Anton, P. J. G. Nieto, C. B. Viejo, and J. A. V. Vilan, "Support vector machines used to estimate the battery state of charge," *IEEE Trans. Power Electron.,* vol. 28, pp. 5919-5926, Dec. 2013.

[133] J. C. Álvarez Antón, P. J. García Nieto, F. J. de Cos Juez, F. Sánchez Lasheras, M. González Vega, and M. N. Roqueñí Gutiérrez, "Battery state-of-charge estimator using the SVM technique," *Appl. Mathematical Modelling,* vol. 37, pp. 6244-6253, May. 2013.

[134] Q. S. Shi, C. H. Zhang, and N. X. Cui, "Estimation of battery state-of-charge using ν-support vector regression algorithm," *Int. J. of Automotive Technology,* vol. 9, pp. 759-764, Dec. 2008.

[135] Z. Niaona and L. Kewei, "The prediction of SOC based on multiple dimensioned Support Vector Machine," in *Proc. Second Int. Conf. on Mechanic Automation and Control Eng. (MACE)*, Jul. 2011, pp. 1786-1788.

[136] T. Hansen and C.-J. Wang, "Support vector based battery state of charge estimator," *J. Power Sources*, vol. 141, pp. 351-358, Mar. 2005.

[137] C. Hung Cheng, C. Shuo Rong, C. Hong Chou, W. Shing Lih, and C. Liang Rui, "Fast Estimation of State of Charge for Lithium-Ion Battery," in *Proc. Int. Symp. Computer, Consumer and Control (IS3C)*, Jun. 2014, pp. 284-287.

[138] A. H. Ranjbar, A. Banaei, A. Khoobroo, and B. Fahimi, "Online estimation of state of charge in li-ion batteries using impulse response concept," *IEEE Trans. Smart Grid*, vol. 3, pp. 360-367, Mar. 2012.

[139] A. Zenati, P. Desprez, and H. Razik, "Estimation of the SOC and the SOH of li-ion batteries, by combining impedance measurements with the fuzzy logic inference," in *Proc. 36th Annu. Conf. on IEEE Ind. Electron. Soc. (IECON)*, Nov. 2010, pp. 1773-1778.

[140] A. Zenati, P. Desprez, H. Razik, and S. Rael, "Impedance measurements combined with the fuzzy logic methodology to assess the SOC and SOH of lithium-ion cells," in *Proc. IEEE Veh. Power and Propulsion Conf. (VPPC)*, Sept. 2010, pp. 1-6.

[141] L. Yi-Feng, C. S. A. Gong, C. Long-Xi, and L. Yi-Hua, "AC impedance technique for dynamic and static state of charge analysis for Li-ion battery," in *Proc. IEEE 17th Int. Symposium on Consumer Electronics (ISCE)*, Jun. 2013, pp. 9-10.

[142] R. Li, J. Wu, H. Wang, and G. Li, "Prediction of state of charge of Lithium-ion rechargeable battery with electrochemical impedance spectroscopy theory," in *Proc. IEEE 5th Ind. Electron. and Applicat. Conf. (ICIEA)*, Jun. 2010, pp. 684-688.

[143] M. F. Samadi, G. A. Nazri, and M. Saif, "Application of Dynamic Cell Resistance for determination of state of charge," in *Proc. IEEE Transportation Electrification Conf. and Expo (ITEC)*, Jun. 2014, pp. 1-5.

[144] X. Ying, L. Chenjie, and B. Fahimi, "Online State of Charge estimation in electrochemical batteries: Application of pattern recognition techniques," in *Proc. 28th Annu. IEEE Appl. Power Electron. Conf. and Exposition (APEC)*. Mar. 2013, pp. 2474-2478.

[145] J. Lin, X. Tang, B. J. Koch, D. R. Frisch, and M. J. Gielniak, "Dynamically adaptive method for determining the state of charge of a battery," ed: Google Patents, Aug. 2010.

[146] T. Gallien, B. Schweighofer, M. Recheis, and H. Wegleiter, "State of charge determination of LiFePO4 batteries using an external applied magnetic field," in *Proc. 39th Annu. Conf. of IEEE Ind. Electron. Soc. (IECON)*, Nov. 2013, pp. 4000-4004.

[147] A. Wenzler, "Method and Device for Determining a Charge State of a Battery with the Aid of a Fluxgate Sensor," ed: Google Patents, Jul. 2012.

[148] H. Aung, K. S. Low, and S. T. Goh, "State-of-Charge Estimation of Lithium-ion Battery Using Square Root Spherical Unscented Kalman Filter (Sqrt-UKFST) in Nanosatellite," *IEEE Trans. Power Electron.,* vol. 30, pp. 4774-4783, Sept. 2015.

[149] H. Rahimi-Eichi, F. Baronti, and C. Mo-Yuen, "Online adaptive parameter identification and state-of-charge coestimation for lithium-polymer battery cells," *IEEE Trans. Ind. Electron.,* vol. 61, pp. 2053-2061, Apr 2014.

[150] H. Rahimi-Eichi, F. Baronti, and M. Y. Chow, "Modeling and online parameter identification of Li-Polymer battery cells for SOC estimation," in *Proc. IEEE Int Symposium on Industrial Electronics (ISIE)*, May. 2012, pp. 1336-1341.

[151] C. Unterrieder, C. Zhang, M. Lunglmayr, R. Priewasser, S. Marsili, and M. Huemer, "Battery state-of-charge estimation using approximate least squares," *J. Power Sources,* vol. 278, pp. 274-286, Mar. 2015.

[152] K. A. Smith, C. D. Rahn, and C. Y. Wang, "Model-based electrochemical estimation and constraint management for pulse operation of lithium ion batteries," *IEEE Trans. Control Syst. Technol.,* vol. 18, pp. 654-663, May. 2010.

[153] D. Di Domenico, G. Fiengo, and A. Stefanopoulou, "Lithium-ion battery state of charge estimation with a Kalman Filter based on a electrochemical model," in *Proc. IEEE Int. Conf. on Control Applicat. (CCA)*, Sept. 2008, pp. 702-707.

[154] D. Di Domenico, A. Stefanopoulou, and G. Fiengo, "Lithium-Ion Battery State of Charge and Critical Surface Charge Estimation Using an Electrochemical Model-Based Extended Kalman Filter," *J. of Dynamic Syst. Measurement and Control,* vol. 132, pp. 061302-061302, Oct. 2010.

[155] S. K. Rahimian, S. Rayman, and R. E. White, "State of Charge and Loss of Active Material Estimation of a Lithium Ion Cell under Low Earth Orbit Condition Using

Kalman Filtering Approaches," *J. of The Electrochemical Soc.*, vol. 159, pp. A860-A872, Apr. 2012.

[156] S. Santhanagopalan and R. E. White, "Online estimation of the state of charge of a lithium ion cell," *J. Power Sources*, vol. 161, pp. 1346-1355, Oct. 2006.

[157] R. Klein, N. A. Chaturvedi, J. Christensen, J. Ahmed, R. Findeisen, and A. Kojic, "Electrochemical Model Based Observer Design for a Lithium-Ion Battery," *IEEE Trans. Control Syst. Technol.*, vol. 21, pp. 289-301, Mar. 2013.

[158] S. J. Moura, N. A. Chaturvedi, and M. Krstić, "Adaptive Partial Differential Equation Observer for Battery State-of-Charge/State-of-Health Estimation Via an Electrochemical Model," *J. of Dynamic Syst. Measurement, and Control*, vol. 136, pp. 011015-011015, Oct. 2013.

[159] M. F. Samadi, S. M. M. Alavi, and M. Saif, "Online state and parameter estimation of the Li-ion battery in a Bayesian framework," in *Proc. American Control Conf. (ACC)*, Jun. 2013, pp. 4693-4698.

[160] M. Corno, N. Bhatt, S. M. Savaresi, and M. Verhaegen, "Electrochemical Model-Based State of Charge Estimation for Li-Ion Cells," *IEEE Trans. Control Syst. Technol.*, vol. 23, pp. 117-127, Jan. 2015.

[161] C. Zheng and K. S. Low, "A virtual instrument for the testing and performance evaluation of a microsatellite power supply system," *IEEE Trans. Instrum. Meas.*, vol. 57, pp. 1808-1815, Aug. 2008.

[162] L. Gao, S. Liu, and R. A. Dougal, "Dynamic lithium-ion battery model for system simulation," *IEEE Trans. Compon. Packag. Technol.*, vol. 25, pp. 495-505, Sept. 2002.

[163] C.-T. Chen, *Linear system theory and design*: New York : Oxford University Press, Fourth edition., 2013.

[164] S. S. Haykin, *Kalman filtering and neural networks*. New York: Wiley, 2001.

[165] W. He, N. Williard, C. Chen, and M. Pecht, "State of charge estimation for electric vehicle batteries using unscented kalman filtering," *Microelectronics Reliability*, vol. 53, pp. 840-847, Jan. 2013.

[166] M. Partovibakhsh and G. Liu, "Online estimation of model parameters and state-of-charge of Lithium-Ion battery using unscented Kalman filter," in *Proc. American Control Conf (ACC)*, Jun. 2012, pp. 3962-3967.

[167] F. Baronti, W. Zamboni, N. Femia, R. Roncella, and R. Saletti, "Experimental analysis of open-circuit voltage hysteresis in lithium-iron-phosphate batteries," in *Proc. IEEE 39th Annu. Conf. Industrial Electron. Soc. (IECON)*, Mar. 2013, pp. 6728-6733.

[168] K. Jonghoon, S. Gab-Su, C. Changyoon, C. Bo-Hyung, and L. Seongjun, "OCV hysteresis effect-based SOC estimation in extended Kalman filter algorithm for a LiFePO/C cell," in *Proc. IEEE Int. Electric Vehicle Conf. (IEVC).* Mar. 2012, pp. 1-5.

[169] F. Baronti, N. Femia, R. Saletti, C. Visone, and W. Zamboni, "Hysteresis Modeling in Li-Ion Batteries," *IEEE Trans. Magn.*, vol. 50, pp. 1-4, Nov. 2014.

[170] H. He, R. Xiong, X. Zhang, F. Sun, and J. Fan, "State-of-charge estimation of the lithium-ion battery using an adaptive extended kalman filter based on an improved Thevenin model," *IEEE Trans. Veh. Technol.*, vol. 60, pp. 1461-1469, May. 2011.

[171] J. L. Crassidis and J. L. Junkins, *Optimal estimation of dynamic systems*, 2nd ed. Boca Raton, FL: CRC Press, 2012.

[172] D. Simon, *Optimal state estimation : Kalman, H∞ and nonlinear approaches*. Hoboken, N.J.: Wiley-Interscience, 2006.

[173] S. J. Julier, "The spherical simplex unscented transformation," in *Proc. American Control Conf.*, Jun. 2003, pp. 2430-2434 vol.3.

[174] O. Tremblay and L.-A. Dessaint, "Experimental validation of a battery dynamic model for EV applications," *World Electric Vehicle J.*, vol. 3, pp. 1-10, May. 2009.

[175] L. Long and P. Bauer, "Practical Capacity Fading Model for Li-Ion Battery Cells in Electric Vehicles," *IEEE Trans. Power Electron.*, vol. 28, pp. 5910-5918, Dec. 2013.

[176] D. Haifeng, W. Xuezhe, and S. Zechang, "A new SOH prediction concept for the power lithium-ion battery used on HEVs," in *Proc. IEEE Vehicle Power and Propulsion Conf. VPPC.*, Sept. 2009, pp. 1649-1653.

[177] L. Lam, P. Bauer, and E. Kelder, "A practical circuit-based model for Li-ion battery cells in electric vehicle applications," in *Proc. IEEE 33rd Int Telecommunications Energy Conference (INTELEC)*, Oct. 2011, pp. 1-9.

[178] C. Y. Chun, J. Baek, G.-S. Seo, B. H. Cho, J. Kim, I. K. Chang, *et al.*, "Current sensor-less state-of-charge estimation algorithm for lithium-ion batteries utilizing filtered terminal voltage," *J. Power Sources*, vol. 273, pp. 255-263, Jan. 2015.

[179] G. L. Plett, "Extended Kalman filtering for battery management systems of LiPB-based HEV battery packs: Part 3. State and parameter estimation," *J. Power Sources,* vol. 134, pp. 277-292, Aug. 2004.

[180] R. K. Mehra, "Approaches to adaptive filtering," *IEEE Trans. Autom. Control,* vol. 17, pp. 693-698, Oct. 1972.

[181] R. Vepa, "Adaptive state estimation of a PEM fuel cell," *IEEE Trans. Energy Convers.*, vol. 27, pp. 457-467, Jun. 2012.

[182] A. H. Mohamed and K. P. Schwarz, "Adaptive Kalman Filtering for INS/GPS," *J. Geodesy,* vol. 73, pp. 193-203, May 1999.

[183] W. Ding, J. Wang, C. Rizos, and D. Kinlyside, "Improving Adaptive Kalman Estimation in GPS/INS Integration," *J. Navigation,* vol. 60, pp. 517-529, Sept 2007.

[184] T. Huria, M. Ceraolo, J. Gazzarri, and R. Jackey, "High fidelity electrical model with thermal dependence for characterization and simulation of high power lithium battery cells," in *Proc. IEEE Int. Electric Vehicle Conf. (IEVC)*, Greenville, SC, Mar. 2012, pp. 1-8.

[185] S. Xie, G. X. Lee, K.-S. Low, and E. Gunawan, "Wireless Sensor Network for Satellite Applications: A Survey and Case Study," *Unmanned Systems,* vol. 02, pp. 261-277, Jul. 2014.

[186] J. J. Soon and K. S. Low, "Photovoltaic model identification using particle swarm optimization with inverse barrier constraint," *IEEE Trans. Power Electron.*, vol. 27, pp. 3975-3983, Sept. 2012.